Durability of stiffened CFRP panels with initial delaminations

Daan Jonas Hottentot Cederløf

Technische Universiteit Delft

TU Delft Delft University of Technology

Challenge the future

DURABILITY OF STIFFENED CFRP PANELS WITH INITIAL DELAMINATIONS

by

Daan Jonas Hottentot Cederløf

in partial fulfillment of the requirements for the degree of

Master of Science
in Aerospace Engineering

at the Delft University of Technology,
to be defended publicly on Monday July 2nd, 2018 at 14:00.

Supervisor:	Prof. dr. ir. C. Kassapoglou	
Thesis committee:	Prof. dr. ir. R. Benedictus,	TU Delft
	Dr. ir. C. Rans,	TU Delft
	Prof. dr. ir. M. V. Donadon,	ITA

This thesis is confidential and cannot be made public until July 1, 2018.

TU Delft Delft University of Technology

ABSTRACT

As composites materials and bonded structures are increasingly being implemented in aerospace structures it is imperative to increase their weight specific performance. A shift is required in design philosophy, moving from a conservative safe life approach towards a damage tolerant philosophy. By allowing damage to exist in a structure, lighter designs may be realized, reaping significant benefits in a weight centered industry. However, the damage growth must be well understood and predicted, to ensure that a critical damage size is never reached between inspections. In this thesis a step is taken in that direction: a numerical damage model, accounting for static and fatigue delamination growth, is validated on the sub-component level by means of a series of experimental tests.

The sub-component to be tested is a CFRP skin reinforced with a T-stiffener. An initial delamination (size 20% of the panel length) is introduced in the skin-stiffener interface halfway down the panel length. Due to the repeated buckling of the skin during compressive fatigue loading, the delamination grows under mixed-mode conditions.

Prior to fatigue testing and modelling, a quasi-static test was performed to validate: the buckling load, the global stiffness and the ultimate load predicted by the model. A Hashin based damage model was used in the composite sections with an energy based damage propagation criterion. Good agreement was found between the experimental test and the numerical model in terms of buckling load, panel stiffness and ultimate load. Furthermore, the buckling mode (a diagonal half wave on the skin) was captured by the model.

The fatigue load cycle is determined using a low fidelity FEM analysis and experimental calibration. A Pmax of -47kN was selected, at an R-ratio of 10 (compression-compression). This is roughly 40% of the ultimate load of the panel and well within the post-buckling regime. Each panel was subject to up to 350'000 fatigue cycles in order to obtain a measurable delamination growth. By means of periodic ultrasonic inspection, the delamination shape and magnitude was tracked.

The numerical model is based on a cohesive zone formulation where static damage is determined with a bi-linear softening law and the fatigue damage is controlled by a fracture mechanics based Paris relation. It was implemented as a user defined sub-routine (VUMAT) by Lucas A. Oliveira in the commercial FE software Abaqus. In order to model high-cycle fatigue, a cycle jump method is employed in the explicit FEM model. Comparison of intermittent ultra-sonic scans showed a good agreement with the numerical model in terms of the delamination shape evolution. However, due to Paris (fatigue crack growth rate) data being sourced from open literature, the magnitude of delamination area was not accurately captured. The numerical model can not be validated until correct Paris data is obtained for the material used.

Following fatigue testing, the residual strength of the panels was tested. A slight decrease in ultimate strength was observed in the panels subject to fatigue testing. Additionally, a minor decrease in stiffness was found. Quasi-static testing throughout the fatigue life of one panel reveals a 2.7% decrease in panel stiffness after 350'000 fatigue cycles. Due to computational limitations, this intra-laminar fatigue degradation was not modelled, however it is argued to be small enough to be omitted.

ACKNOWLEDGEMENTS

This thesis summarizes my student career at the Delft University of Technology and year long exchange to Brazil. Throughout my studies I have had the pleasure of meeting a great variety of people from all over the world. These people have positively influenced me and my future, for which I am truly grateful.

Benedicte, you brought me a sense of peace and calmed my nerves. Without your support and love, especially during my year abroad, I would not have been able to keep my bearings.

Christos, I am grateful for the opportunity you gave me. After 5 years in Delft, I needed a change of environment and a year in Brazil provided just that. Your unwavering support and critical feedback is exactly what an aspiring student needs.

I was welcomed with open arms in the Elefante Branco lab at the Instituto Tecnológico de Aeronáutica. Thank you for integrating me so quickly into the group and for the lively discussions over coffee so strong it required a knife and fork to consume. To my daily supervisors at ITA: Donadon and Mariano, your dedication to your students is what distinguishes the learning environment you have created. I am impressed and grateful. To the three co-pilots in my office room: I could never have achieved my results without your relentless support. A special thank you to Lucas and Ricardo, specialists in their respective fields, for showing me the ropes.

A final warm thanks goes out to my friends and fellow students at the TU Delft. Mark and Ruben, your daily critique of my thesis work greatly improved its quality. To all the rest of you, thanks for occasionally distracting me (although in all honesty that is not too difficult) and giving me the opportunity to take a step back from my work.

Daan Jonas Hottentot Cederløf
Delft, June 2018

CONTENTS

List of Symbols

Acronyms

CFRP	Carbon Fibre Reinforced Polymer
CZM	Cohesive Zone Model
DCB	Double Cantilever Beam
DIC	Digital Image Correlation
FAA	Federal Aviation Administration
FEM	Finite Element Method
FE	Finite Element
LEFM	Linear Elastic Fracture Mechanics
VCCT	Virtual Crack Closure Technique
SERR	Strain Energy Release Rate
XFEM	Extended Finite Element Method
SIF	Stress Intensity Factor
NDT	Non Destructive Testing
UT	Ultrasonic Testing
4ENF	4-point bend End Notched Flexure
MMB	Mixed Mode Bending
LVDT	Linear Variable Differential Transformer
OEM	Original Equipment Manufacturer

Latin Symbols

A	Area	m^2
a	Crack length	m
a_0	Initial crack length	m
C	Paris relation constant	-
D	Damage parameter	-
d_s	Static damage	-
d_f	Fatigue damage	-
E	Young's modulus	N/m^2
G	Shear modulus	N/m^2
G	Strain Energy Release Rate	J/m^2
G_c	Critical Strain Energy Release Rate	J/m^2
h	Element height	m
I,II,III	Subscript for mode I, II and II	-
K	Stress Intensity Factor	$N/m^2\sqrt{m}$
l	Panel length	m
l_e	Element length	m
m	Paris relation exponent	-
N	Fatigue cycles	-
P	Load	N
R	Load ratio	-
S	Strength	N/m^2
U	Strain energy	J
w	Disbond width	m

Greek Symbols

δ	Displacement	m
η	BK interpolation constant	-
ν	Poisson ratio	-
σ	Stress	N/m^2
ϕ	Mixed mode ratio	-

List of Figures

List of Tables

1

INTRODUCTION

Since the introduction of commercial aircraft in the early 1900s numerous different types of aircraft have been designed and manufactured. An incredible progression has taken place since the de Havilland airco DH4 first flew in 1916, in terms of performance, comfort and safety. Early designs used cloth and wood as main airframe materials, a paradigm shift occurred in the 1920s when the first aluminium aircraft took to the skies. Another revolution is currently taking place with the development of full composite aircraft such the Boeing 787, Airbus A350 and the Honda HA-420 business jet. This shift towards composite primary aero-structures is primarily motivated by the possible weight savings which in turn results in lower weight and fuel usage, which reduces operating costs and emissions. With new materials come new methods for both manufacturing and design, this three-way relation is also known as the trinity principle. Composites are not suited for traditional fastening methods such as bolting and riveting as the necessary holes for such fastening methods introduces delaminations and fibre discontinuities. Furthermore, the lack of plasticity in composites means that the manufacturing tolerances become increasingly restrictive. Adhesive bonding is therefore a joining method with a great application potential, when compared to traditional joining methods. Advantages include:

- it allows the joining of dissimilar materials
- there is no need for multiple manufacturing steps such as drilling, reaming, deburring and riveting
- without protruding rivet or bolt heads it allows for more aerodynamically efficient surfaces
- it can allow for a weight saving wrt. mechanical fasteners
- as a chemical barrier it can prevent corrosion
- as a mechanical barrier it can act as a sealant

There are however a number of drawbacks which have limited the use of adhesive bonding in primary aircraft structures. Current limitations/restrictions include:

- certification of the (repeatability of the) manufacturing process, to avoid so called 'kissing bonds'
- limited/slow NDT methods for inspecting bonded areas, visual inspections of the bond interface are physically impossible
- technology readiness/maturity is not high enough for sophisticated knowledge of disbond growth and failure
- difficulty in implementing a 'Damage Tolerant' design philosophy. [11]
- required chemical and/or mechanical surface treatment to ensure, among others, a contaminant-free surface with adequate wettability and surface energy [12]
- sensitivity to environmental conditions such as moisture and temperature [13]

1.1. RESEARCH AIM, QUESTIONS AND OBJECTIVES

The aim of the project is to **analyse the durability of bonded stiffened composite panels with initial flaws under cyclic compressive loading**.

In order to achieve the thesis aim, the following research questions are posed. Note, the main research question is in bold.

1. What is the state-of-the-art knowledge regarding the modelling of bonds in composite structures under static and fatigue loading?
2. How does the disbond size and position influence the stability of a stiffened composite panel?
3. **What is the correlation between disbond growth rate under fatigue loading and the disbond size?**

The research questions are broken into objectives, which serve to answer the posed research questions. The primary objective is: **To experimentally validate a fatigue crack growth model, using a cohesive zone formulation, on the sub-assembly level by analyzing fatigue crack growth in artificially disbonded stiffened panels**

The following sub-objectives are established in order to answer the research aim and questions in a logical order. These sub-objectives are in turn implemented in a Gantt chart in Appendix A.

1. Compile an analysis of state-of-the-art on stability and durability of bonded composite structures
   (a) Investigate possible bonding techniques and what influences the bond properties in terms of geometry and environmental conditions
   (b) Determine the relation between disbond size and the buckling load/mode
   (c) Study modelling techniques for static and fatigue driven crack growth with a bias towards cohesive zone modelling
   (d) Investigate current/past experimental efforts on fatigue crack growth at coupon and sub-assembly level
2. Create and verify FE models to analyze:
   (a) Static/implicit: Linear buckling
   (b) Static/implicit: Non-Linear buckling
   (c) Dynamic/explicit: Fatigue crack growth
   (d) Dynamic/explicit: Ultimate load including the Hashin damage criterion
3. Validate FE models by performing quasi-static and fatigue compression experiments

1.2. PROBLEM INTRODUCTION

The proposed thesis is part of a larger project, named: INOVA. The aim is to investigate the durability of bonded and co-cured joints in primary composite aerospace structures. Furthermore, the influence of elevated temperature and humidity on the joint properties is studied. The goal is ultimately to achieve a better understanding of the behaviour of bonded joints over a typical aircraft lifetime. This may then be further implemented in the damage tolerant design of a bonded composite structure for application within a primary aerospace structure.

The scope of this MSc thesis is limited to co-cured composite (Carbon/Epoxy) panels at room temperature ambient (RTA) conditions. However, due to the broad nature of the INOVA project, a brief study is performed on adhesive bonding in chapter 2.1. Bonding techniques and environmental affects are investigated to understand the broader scope of the whole project and how the research of this proposed MSc thesis will contribute to the larger aim of the INOVA project. The study of bonded joints is relevant to co-cured

structures since the mechanisms of crack growth in a bonded joint are comparable to delamination growth in a co-cured interface.

The primary contributing members of the INOVA project are Instituto Tecnologica de Aeronautica (ITA) and Embraer. The stiffened panels to be investigated are produced (by Embraer) and introduced here to give a better understanding of the physical problem at hand. In fig. 1.1 an example panel is shown. It consists of a co-cured carbon/epoxy skin and stiffener, the lay-up and cross-section is shown in fig. 1.2. An artificial disbond is introduced halfway down the stiffener element by means of a Teflon^{TM} (PTFE) tape.

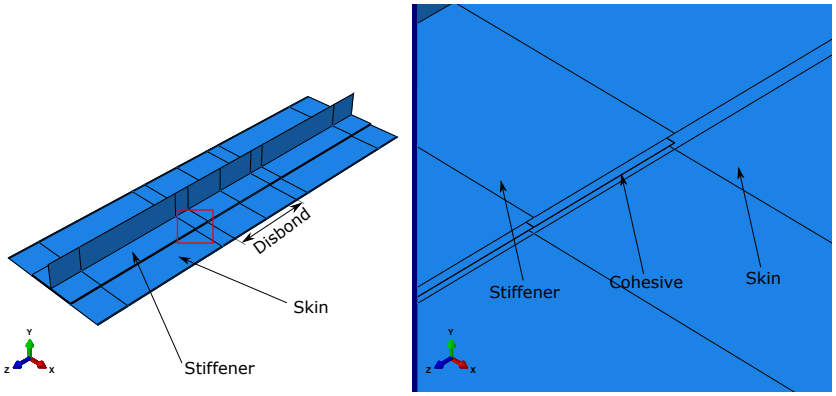

Figure 1.1: Left: global overview of panel, showing disbonded region in center. Right: zoomed in view of where cohesive section, joining the skin and stiffener, ends (disbond starts)

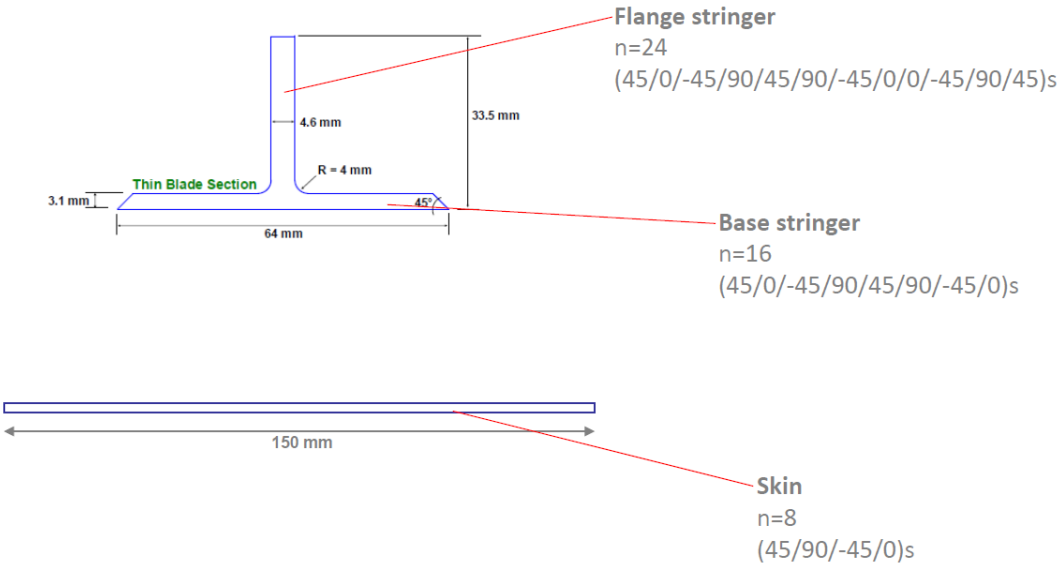

Figure 1.2: Panel cross-sectional view, with lay-ups of skin and stiffener shown.

2

LITERATURE SURVEY

The literature research is broken down in the following progression. It will cover the first and the second objectives mentioned in chapter 1. Adhesive bonding is discussed in chapter 2.1: what are the various available bonding techniques and how are they influenced by environmental/geometric conditions? In chapter 2.2 stability of bonded structures with initial imperfections is discussed including a reflection on the panels that are to be used in the experimental phase of the thesis.

The topic of fatigue disbond growth is investigated in chapter 2.3, with a primary focus on Cohesive Zone Models (CZM). Finally, in appendix B various Non Destructive Testing (NDT) techniques are investigated. Each chapter is concluded with a summary and reference to the research questions and objectives posed in section 1.1.

2.1. ADHESIVE BONDING

In order to answer research question 1 and research objectives 1a and 1d, posed in section 1.1, an understanding of the principles of adhesive bonding is requisite. The FAA [14] defines the following: "Bonded structures include multiple interfaces (e.g., composite-to-composite, composite-to-metal, or metal-to-metal), where at least one of the interfaces requires additional surface preparation prior to bonding.". Bonding is an interesting process since it combines the creation of the joining material (i.e the adhesive is cured) and simultaneously joins multiple parts to form the geometry of a structure. In this section some fundamental concepts related to bonded structures are introduced. Particularly, bonded aerospace **thermoset** composite structures are of interest.

Three different methods of bonding are described in section 2.1.1. Knowledge of how different bonding techniques influence the strength and fracture toughness of a bonded composite joint is discussed in sections 2.1.2 and 2.1.5. Additionally, bonds are influenced by surface preparation, joint configuration, material parameters(adhesive and adherend), geometrical parameters(adhesive thickness, overlap length, stacking sequence, ply angle) and failure mode [15]. These topics are investigated in sections 2.1.2 and 2.1.3. Finally, the effect of fibre bridging and fracture toughness are discussed in sections 2.1.4 and 2.1.5.

2.1.1. BONDING TECHNIQUES

The term given to the different composite bonding techniques is dependent on the state of the adherends, which can be either cured or un-cured. Co-curing is the process where two un-cured laminates are cured and bonded in the same curing cycle. In the case of co-curing there is an additional variable: whether or not an adhesive layer is used to bond the two adherends. It is interesting to note the FAA definition mentioned in the beginning of this section. Since the adherends in a co-cured process are not subject to surface treatment prior to bonding, the process may not technically fall under to category of adhesive bonding.

The secondary bonding process involves two cured laminates which are bonded with a layer of adhesive, which is then cured. This process also works for dissimilar materials allowing for example metals to be bonded to composite structures. Surface treatment of both adherend surfaces is critical to ensure a proper chemical bond as opposed to a 'kissing bond'. When only one of the two adherends is cured the process is called co-bonding. Again, dissimilar materials may be bonded by means of co-bonding. The various bonding techniques are illustrated in figure 2.1.

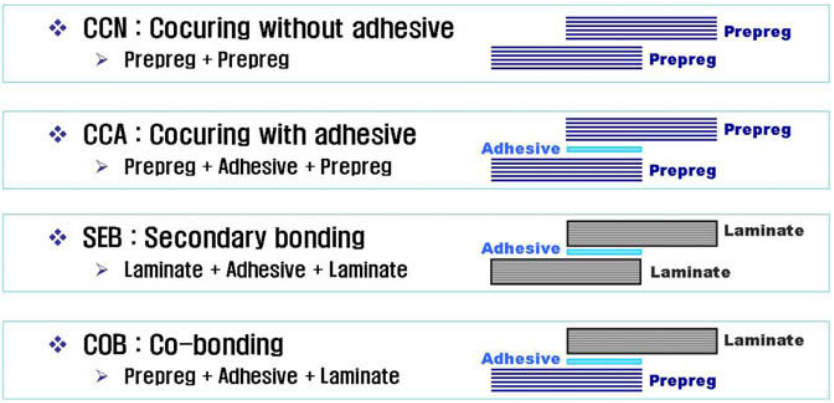

Figure 2.1: Overview of four different bonding methods, obtained from Song et al. [1]

Generally, co-cured parts require fewer manufacturing and preparing steps, reducing both production time and cost. Compared to secondary bonding and co-bonding, the surfaces of the co-cured adherends for example do not require cleaning and pre-treatment prior to bonding. Furthermore, the material, geometry and bond are created in one shot, whereas a co-bonded or secondary bonded structure requires at least one extra curing cycle. However, co-cured bonds are more difficult to manufacture due to higher complexity moulds required to ensure the final part geometry. Therefore, co-cured joints are often limited to manufacturing of smaller, less complex parts.

When analyzing failure in bonded joints the failure mode can be divided into three categories. A cohesive failure mode occurs when a crack forms within the adhesive. If the crack occurs along the interface between the adherend and the adhesive it is classified as a adhesive failure. Finally, failure may occur in the adherend material, without damage to the adhesive material, simply called adherend failure. In the case of bonded composite joints, inter-laminar or intra-laminar failure of the adherends falls under the adherend failure mode. Generally, a cohesive failure or adherend failure is desired, an adhesive failure mode is indicative of improper manufacturing, as will be discussed in section 2.1.3.

2.1.2. STRENGTHS OF DIFFERENT BONDING TECHNIQUES

Song et al. [1] tested 391 single lap specimens with different adherend thicknesses, overlap lengths and lay-ups. This extensive research included secondary-bonds, co-bonds, and co-cured joints with and without an adhesive layer between the un-cured pre-pregs. The global results are shown in fig. 2.2. The co-bonded joints showed consistently lower failure strengths and failed adhesively. The co-cured (both with and without extra adhesive) and the secondarily bonded joints failed cohesively. The co-cured bonds without additional adhesive showed the highest failure strength. The results regarding bond strengths are consistent with the findings reported by Mohan et al. in [16, 17]. It is important to note that this is a coupon level experiment with a single failure mode (mode II shear). Using bonding in joints is generally only advisable where the expected load is predominantly of a shearing nature. Adhesive bonds performs quite poorly in mode I crack opening where the adherends are peeled or pried apart as demonstrated in [16, 17].

2.1.3. SURFACE PREPARATION INFLUENCE ON BOND STRENGTH

Prior to bonding, the adherend surfaces must be adequately prepared. This includes removal of foreign debris and contaminants in order to improve surface energy, wetting and surface material activation. In the case

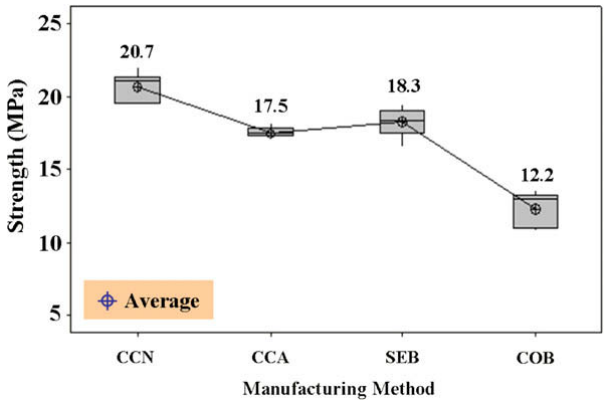

Figure 2.2: Comparison of strengths for different bonding techniques, see fig. 2.1 for abbreviation definitions

of co-bonding or secondary bonding surface cleaning is used to remove any traces of release agents which may be left by peel-plies or mould surface. In the case of 'dry' peel plies it is necessary to remove any traces of fibres left behind on the adherend surface. Surface treatment may be performed physically by grinding, abrading, grit blasting, plasma, flame treatment, laser, UV/ozone or corona treatment. All have their respective benefits and drawbacks. Kanerva et al. [18] demonstrated the use of peel plies or tear peel plies resulted in lower bond shear strengths than when mechanical abrasion was used to treat the adherend surface. Both the tear peel ply and the normal peel ply failed adhesively whilst the mechanically abraded joint failed either cohesively or in the adherend material.

2.1.4. FIBRE BRIDGING

During co-curing or secondary bonding, fibres from the un-cured adherends may form connections (bridges) between the adherends and/or adhesive. Fibres from the scrim cloths used in some adhesives may also form cross-links between the adherends [16, 17]. This cross-linking mechanism has a toughening effect with respect to delamination growth and may be particularly useful in mode I crack openings. Yao et al. have performed numerous studies regarding fibre bridging and its influence on the quasi-static and fatigue characteristics of adhesives [19–21].

Coupon level experiments were performed for mode I crack opening using co-cured DCB specimens. No additional adhesive was included. Yao et al. [21] demonstrated that fibre bridging significantly influenced the fatigue crack growth behaviour of the samples. It was found that interfaces with adjacent 45° plies showed significantly more fibre bridging than interfaces between two 0° plies. Static test results showed an increase in fracture toughness G_{IC}, which is due to the fibres behind the crack tip reducing the stress intensity factor. A final observation was that the fibre bridging caused by quasi-static loading was different from that caused by fatigue loading. This means that it is not correct to normalize data obtained from fatigue experiments with parameters from quasi-static experiments since the damage state is different. Furthermore, Pascoe et al. [22] argue that this proves that fatigue resistance is not solely related to fracture toughness. This is has implication for the models discussed in section 2.3.

In [20], the effect of fibre bridging on the classic Paris relation is investigated (Mode I, DCB test), it is found that an increase in fibre bridging affects only the C value in equation 2.1 (as does stress ratio R), whilst the variable m is dependent on the stress ratio and not the fibre bridging. Further investigation on the impact of laminate thickness in [19] found that thinner laminates showed a larger amount of fibre bridging than thicker laminates, especially in the early formation of the crack. The Paris relation is an phenomenological model, relying on curve fitting experimental data based on macroscopic observations. Since it is a macroscopic observation it can be argued that it is not an inherent material property, rather, it is a convenient engineering aid. Based on the premise that it is not per se a constant material property it is valid to incorporate the influence of fibre bridging on the macroscopic crack growth.

$$\frac{da}{dN} = C \cdot (\Delta G)^m \tag{2.1}$$

2.1.5. FRACTURE TOUGHNESS

A common parameter used to characterize adhesive material (along with strength and stiffness) is the fracture toughness. It is defined as the amount of elastic strain energy per unit area of crack growth (eq. (2.2)). Due to the difficulties of calculating the Stress Intensity Factor (K) near the crack tip of a composite material, the Strain Energy Release Rate (G) is normally used to define fracture toughness. This material property is used to model crack growth behaviour, as will be discussed in section 2.3.

$$G := -\frac{\delta U}{\delta A} \tag{2.2}$$

Mohan, Ivankovic and Murphy [16, 17] analysed both mode I and mixed mode fracture toughness for co-cured and secondary bonded composite joints. The experiments were performed at coupon level. Their investigation showed how the different bonding techniques affect the final contained moisture (both free and bound) in the bond, which in turn influences bond fracture toughness. During secondary bonding the adherends did not contain any water since they have been cured, whilst co-cured adherends still contained moisture. Therefore, during the curing cycle of the co-cured joint, the moisture of both the adhesive and adherend plasticised the adhesive polymer which resulted in voids forming at the interface. Further observation included the influence of the Teflon^{TM} insert used to initiate the crack in the co-cured samples: ripples were found in the fracture surface near the crack. The ripples were not present in the co-bonded samples. These ripples are theorized to have affected the initiation values for the fracture toughness in the joints. The data for the co-cured samples showed significantly larger scatter, this is thought to be caused by the teflon tape, however it remains to be proven. Teflon tape is used in this M.Sc. research to introduce artificial defects in the bondline and is therefore of high importance to this thesis project.

Their results showed that for mode I [16], the secondary bonded joints failed cohesively, whilst the co-cured joint showed adhesive failure. This means that the fracture toughness values obtained for the co-cured samples cannot be seen as the correct values for the adhesive. The co-cured samples showed the lowest fracture toughness, for both initiation and propagation of the crack. The secondary bonded samples cured at $120^{\circ}C$ showed lower initiation fracture toughness but higher propagation values compared to samples bonded at $180^{\circ}C$. It was observed that the secondary bonded joint that was cured at a higher temperature showed a significant amount of fibre bridging of the scrim cloth used in the adhesive with the adherends, which may have improved the bond fracture initiation toughness. In the secondary bonded samples, this scrim cloth was observed to often be the interface along which the crack propagated.

The mode II and mixed mode fracture toughness experiments [17] showed that the secondary bonded joints showing mostly cohesive failure with occasional interlaminar failure. The co-cured joints failed adhesively. Again they concluded that the moisture released from the pre-preg during bond curing was responsible for this difference. The mode II fracture toughness was found to be 5-6 times greater than the mode I fracture toughness in each of the bonding techniques. As the mode-mix ratio was increased up to a pure mode II test, the fracture area was found to increase due to more jagged fracture surfaces. The increase in fracture area however was at most a factor 1.6-1.8. Furthermore, a larger plasticity zone behind the crack tip was observed in microscopic analyses, which may account for the large increase in fracture toughness.

2.1.6. RELEVANCE OF BOND INFLUENCING FACTORS TO RESEARCH PROJECT

Without a doubt, the field of adhesive bonding is central in the proposed thesis and the larger INOVA research project. In order to answer the first research question a thorough knowledge of bonding is vital, especially how it is influenced by factors such as surface treatment and geometry.

Various experimental studies were performed at a coupon level to characterize and analyze the strength and toughness of bonded composites. A comparison of the various bonding techniques shows a clear benefit of using either co-cured bonds without adhesive or secondary bonds. The choice of which to use may de-

pend not only on the bond strengths however, since part size and complexity comes into account. Co-curing of a complex part with numerous stiffeners or other smaller elements may be limited by autoclave size. This thesis research will focus on co-cured panels and as such the information gathered here will influence the loading parameters for the proposed experimental tests.

Finally, the study on fibre bridging gave an initial insight into the fatigue behaviour of bonded structures. Of particular interest is how fibre bridging reduces the crack growth behaviour in co-cured composite specimens under fatigue. This is directly related to objective 1d, where experimental fatigue work is to be investigated.

2.2. BUCKLING OF BONDED COMPOSITE STRUCTURES WITH INITIAL IMPERFECTIONS

In the context of stiffened panels, buckling is a phenomenon which most often occurs under axial compression or shear loading. Real life structures under compression are sensitive to imperfections, meaning that structural instability will occur before the ultimate stress of the material is reached. This is illustrated in fig. 2.3, where the load-displacement curve of a generic system reaches a bifurcation point. In the absence of imperfections the solution will continue on the linear slope until yield stress is achieved in the material. However, in the presence of imperfections, as is the case for real life structures, buckling occurs. Various forms of buckling may take place such as global buckling of the stiffener, often associated with failure of the structure (unstable curve in fig. 2.3). On a smaller scale, local buckling of the skin, between stiffeners, rivets or disbonded regions will not lead to immediate catastrophic failure (stable curve in fig. 2.3). The allowance of local buckling to occur in stiffened panel structures may lead to significant mass savings, since the post-buckled structure is still capable of bearing loads without leading to failure [23].

It is shown in numerous studies that the leading cause of failure in stiffened panels subject to quasi-static compression is stiffener-skin separation [24, 25]. In the context of disbond growth analysis it is therefore important to understand the driving force of the crack growth. The question however, is to which extent this can be attributed purely to buckling. Zarouchas and Alderliesten [3], show that crack growth occurs before the buckling load is achieved, which indicates that buckling is not solely responsible for crack growth.

In metal structures, where the post-buckling behaviour is well understood, a design may allow for local buckling to occur thereby significantly increasing the structure's certified load bearing capacity. This weight saving opportunity is currently not fully utilized in composite structures, leading to over-designed and thus heavier structures. Thus, the appealing weight specific properties of composite materials are profitless due to conservative structural designs.

This section investigates the buckling behaviour of stiffened composite panels in the presence of delaminations and disbonds. The phenomenon of local skin buckling is instigated by disbonded stiffening elements and further acts as a mechanism to grow the disbonded area. This is a central topic of investigation related to **research question 2** and is linked to **objective 1b**.

2.2.1. INTRODUCING AN INITIAL DISBOND

Before discussing the impact of disbond size, position and type; it is pertinent to define the disbond. In section 2.1 the concept of adhesive bonding was introduced. Most articles discussed there were based on coupon level experimental regimes, used to determine characteristics specific to the adhesive. In this section we look at a larger scale, the sub-component level.

When talking about initial imperfections or disbonds in the context of stiffened composite panels, we look at damages to the adhesive material and/or its interface with the adherend. In the case of an I-beam bonded to a larger panel, an artificial disbond may be introduced by means of a PTFE film (commonly referred to as: Teflon™). Often a 'full width' disbond is created meaning that the film spans at least the entire width of the beam. PTFE has poor wetting properties and high resistance to Van der Waals forces, meaning that it will prevent the adhesion of the beam to the panel. Such an artificial disbond is a controlled method of replicating

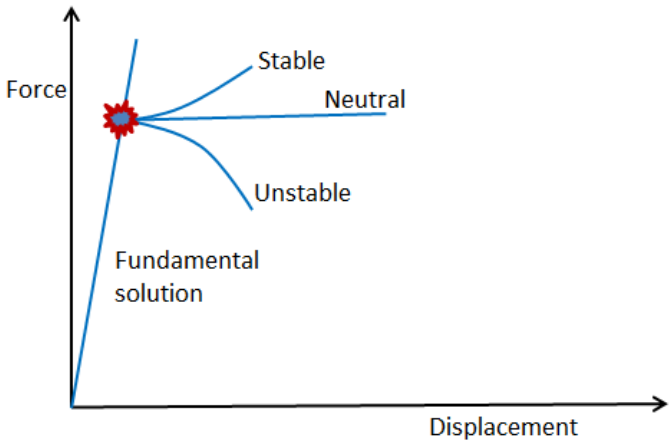

Figure 2.3: The bifurcation point of a structure undergoing buckling, obtained from: comsol.com/blogs/buckling-structures-suddenly-collapse/

disbonds which may occur throughout the service life of an aircraft. Causes for disbonding include impact damage (such as a bird strike) or improper quality control during manufacturing of the joint (leading to so-called kissing bonds).

2.2.2. DISBOND SIZE

Disbond size is generally defined by the distance between the crack fronts as depicted in fig. 1.1 by the teflon foil. In all cases studied here, the disbonds were initially full width, ie. spanning the entire stiffener width. Yap et al. [2] studied buckling and static disbond growth in composite panels reinforced with T-stiffeners. The panel configuration and lay-up are presented in figs. 2.4 and 2.5, respectively. A disbond, located in the third stiffener was monitored as the panel underwent quasi-static loading. It was found that the presence of a bond flaw did not severely reduce the ultimate load of the panel.

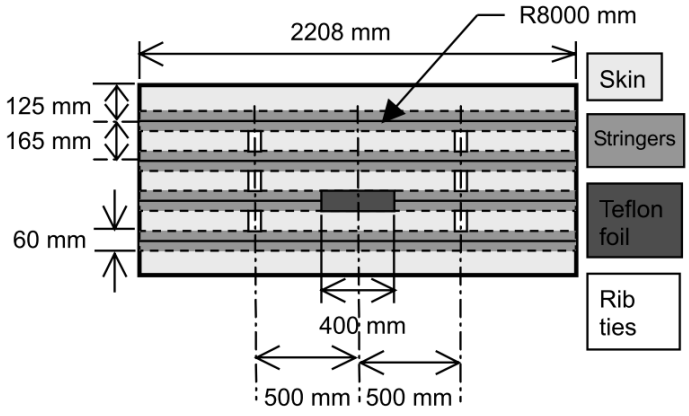

Figure 2.4: The affect of varying disbond sizes on the buckling mode/load of a stiffened CFRP panel, obtained from Yap et al. [2]

Parametric studies were performed by Yap et al. [2] to determine the effect of disbond position and size on the static buckling load of stiffened CFRP panels. It was found that flaws could be categorized into three main groups based on the disbond size, the findings are illustrated in figure 2.6 and summarized below:

- The first category describes a disbond size where no local buckling occurs or where local buckling only

Test panel specifications

Section	Thickness (mm)	Laminate lay-up[a]	Material type
Skin	2.50	[45T, −45T, 0T, 45T, −45T, −45T, 45T, −45T, 45T]	T
Stiffener flange	1.55	[(±45)F, 0T, (±45)F, 0T, (±45)F]	T, F
Stiffener web	4.60	$[(\pm 45)F, 0T, 0T]_{SS}$	T, F
Reinforcement	4.05	[0R, skin lay-up]	T, F

[a] T—tape, F—fabric, R—reinforcement.

Figure 2.5: Stiffener and skin lay-ups used by Yap et al. in [2]

occurs after global buckling. (Disbond size: 0 – 8% of the total panel length)

- The second category (called critical debond size in fig 2.6) is where local buckling at the disbond occurs before global buckling of the panel. This is the category where mode I crack opening occurs near the disbond crack tip. (Disbond size: 10 – 24% of the total panel length)

- The third category includes multiple buckling half-waves in the stiffener flange in the disbond region. Mode II crack growth is dominant in this category, however it requires higher load levels to achieve crack growth initiation. (Disbond size: > 24% of the total panel length)

In terms of fatigue disbond growth the second and third category of disbond size are of interest since that is were local buckling occurs before global buckling. Global buckling of a primary aerospace structure is not acceptable under flight conditions as it will generally lead to catastrophic failure. Under the second and third categories, there will be Mode I and Mode II crack opening, respectively. Subject to cyclic loading typical of two or more aircraft lifetimes this will lead to crack growth. An interesting note is the finding that buckling behaviour of the stiffener flange had a greater effect on the crack growth behaviour than the buckling of the skin. "The wave-like deformation of the stringer flange imposed more localised peeling stress [than the peeling stress resulting from the skin buckling away from the stringer" - Yap et al. [2].

This buckling behaviour is of course highly dependent on the lay-up of the stiffener and skin sections. In order for local buckling of the skin to occur before global buckling, the skin must, in general, have a lower bending stiffness. Furthermore, the lay-up of both the skin and stiffener may be altered to increase buckling resistance in the stiffening element compared to the skin. A semi-analytical approach such as the one proposed by Castro and Donadon [26] may be applied to rapidly iterate towards an initial design (where skin buckling occurs before global buckling) as opposed to a costly FEM based approach. The tool by Castro and Donadon [26] was verified using FEM analyses and further confirms the previous findings that with an increasing disbond length, the buckling load decreases. Their models all consisted of composite plates reinforced with T-stiffeners with various different lay-ups. Further findings included that the aspect ratio of the plate has a significant influence on the buckling load, with longer, slender plates showing lower buckling resistance.

A parametric, numeric model investigating damage tolerance of bonded aluminium skins and stiffeners under compression is proposed by Zarouchas and Alderliesten in [3]. 4 aluminium J-stiffeners were bonded using solid adhesive elements to an aluminium skin, which was subject to compression loading (see upper portion of fig. 2.7). A disbond was modelled between one of the center stiffeners and the skin. This model overlaps the two topics of buckling and disbond growth under compression, however the material used for the skin and stiffeners is isotropic (aluminium). Nevertheless, this study is deemed valuable since it covers disbond influence on stability, investigating both size and position, which will at the very least be comparable for a quasi-isotropic composite design.

Two interesting behaviours were reported [3]: the disbond position critically influenced the buckling load, and a critical flaw size was observed. When this critical flaw size is reached the buckling capacity of the stiffened panel is greatly decreased. Disbond ratio was defined as the total disbonded area divided by the overall bonded area of a stiffener. At a disbond ratio of just under 10% the decrease in buckling load was around 8%. However at a disbond ratio of 16% the buckling load had decreased by 50%. Finally, a plateau was observed for disbond ratios larger than 20%, showing buckling load decrease of around 60%.

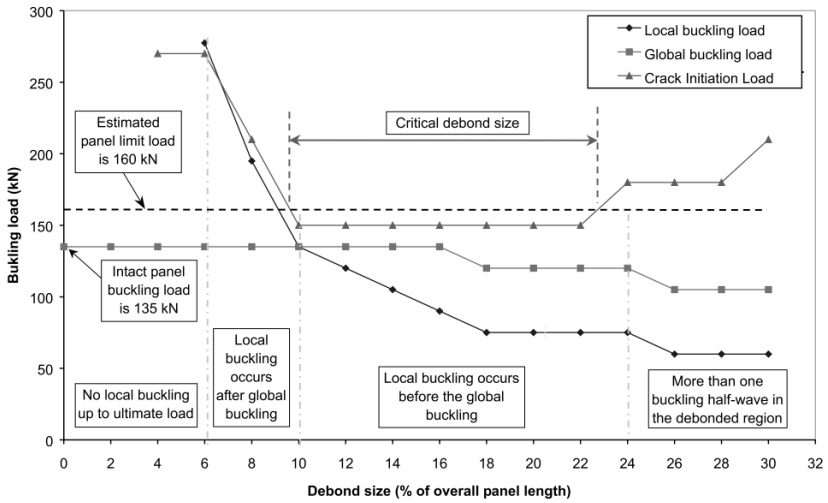

Figure 2.6: The affect of varying disbond sizes on the buckling mode/load of a stiffened CFRP panel, obtained from Yap et al. [2]

2.2.3. DISBOND POSITION

Yap et al. [2] found that the global and local buckling mode shapes were influenced by disbond position only in the case of a medium (category two) disbond (see fig. 2.6). In the case of small disbonds the local buckling mode shape was affected by the global buckling mode shape. The position of the disbond only determined whether crack growth would occur right after buckling or further into the post-buckling regime. This is in contrast with the medium sized disbonds, here the global buckling mode shape was influenced by the position of the local buckle. Furthermore, crack growth initiated regardless of the disbond location.

Zarouchas and Alderliesten also performed parametric numerical studies on how the disbond location in a panel with multiple stiffeners affected the buckling load. They found that for disbonds resulting in a disbond ratio of more than 10% (see section 2.2.2) the buckling load decreased significantly if positioned closer to the clamped edges. For example, in the 1100mm long panel with 4 J stiffeners, a disbond of 170mm in the second stiffener, starting at 100mm from the clamped edge, showed a buckling load of less than 50% of the undamaged panel. Whereas if that same disbond were to be located in the centre (between the two clamped edges), the buckling load reduction would be just 15%.

An illustration is presented in fig. 2.7 showing the variation in buckling load with varying disbond size and position. It must be pointed out though that different buckling modes were encountered for the different positions. When the disbond was located near the clamped edges a mixed mode buckle occurred with the skin displaced away from the stiffener. When the disbond was located near the centre of the panel, a global buckle occurred with the skin between the centre stiffeners displaced towards the stiffeners, resulting in a mode II dominated crack behaviour. This means that the position of the disbond influences the buckling mode, which in turn influences the buckling load.

Furthermore, Zarouchas and Alderliesten [3] used a VCCT based analysis to monitor the onset of disbond growth near the crack tip of the disbond. This analysis is limited to quasi-static loading of the model. Their chosen criterion for crack initiation is shown in eq. (2.3), with the critical SERR (G_C) calculated with the B-K equation (eq. (2.11)). (Further discussion on the analysis methods is presented in section 2.3). An important finding is that crack growth would always occur before the panel buckled. This behaviour, however, is highly dependent on the adhesive material properties such as the threshold and critical fracture toughness, and the B-K coefficient. Panel geometry, loading condition and stiffness ratio between skin and stiffener will play a significant role on crack growth initiation. In other words, this conclusion is case specific.

$$G_I + G_{II} - G_C \geq 0 \tag{2.3}$$

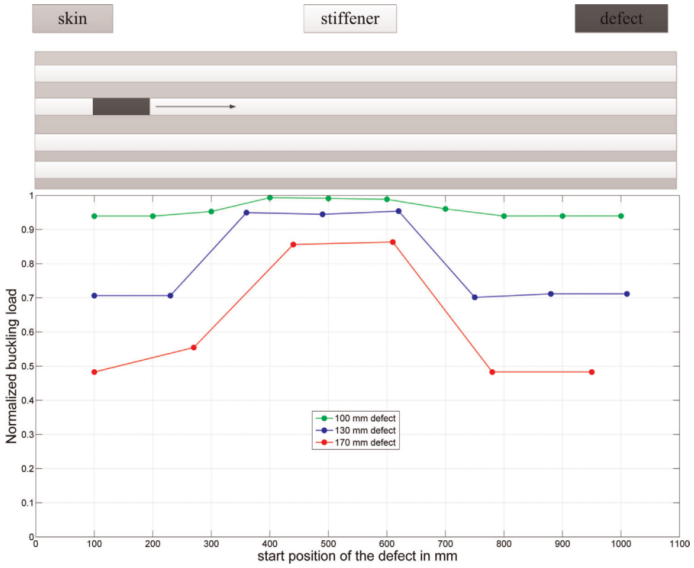

Figure 2.7: Buckling load with varying disbond size and position, obtained from Zarouchas and Alderliesten [3]

Another important observation was that for disbonds near the clamped edges, growth would occur on the crack front facing the center of the panel ie. the bond will grow towards the center. Such a 'self-centering' behaviour is advantageous in the case where an initial disbond is located in the centre. Crack growth will occur on both sides to keep the disbond centred and the skin buckling symmetric. In an experimental context, this means that the test may be run for longer since the crack grows on two fronts, rather than just in a single direction.

A final finding is related to the rate of the disbond growth onset. As the disbond location was moved to the centre of the panel, the disbond growth occurred at a higher load and at a higher rate. The slopes of the G_I and G_{II} values near the tip were steeper and thus the crack growth is more sudden. However, this is in a crack opening dominated by mode II, where static friction may result in this sudden crack growth. In a mode I/mixed mode dominated crack opening, a smoother crack growth is expected, which is indeed observable in the data presented in [3].

2.2.4. RELEVANCE TO PROJECT

In the proposed thesis experiment, a reinforced panel will be subject to cyclic loading. The goal is for the buckling action of the skin to act as a mechanism for the disbond area to grow. Several interesting points have come to light as a result of the investigations in this section which connect directly to **research objective 1b**.

In all the studies investigated in this section a clear relation between disbond size and buckling load is observed. With an increasing disbond length the buckling load decreases. This in itself is not wholly unexpected. However what is interesting is the buckling threshold found for smaller disbonds. Both Zarouchas and Alderliesten [3], and Yap et al. [2] demonstrated that for smaller disbonds (less than 10% of the stiffener length) the buckling load is not significantly altered compared to a pristine panel without a disbond. A sharp decrease in buckling load is observed once this threshold is reached, in the case of Zarouchas and Alderliesten a 50% drop in buckling load was observed when increasing the disbond length from 10% to 16%. On the other hand, a plateau is observed once the disbond has reached a size where local buckling occurs before global buckling. At this point the buckling load is no longer significantly reduced with an increase in disbond size and a change in buckling mode is observed, going from mode I to a mixed mode or mode II crack opening.

Throughout a fatigue disbond growth experiment, in order to have controlled and measurable disbond growth it is desirable to stay between these two limits in disbond size. To avoid significant fatigue damage in

the overall structure the skin needs to buckle away from the stiffener at a lower load than the global buckling load. To maintain a controlled, repeated crack growth the buckling mode should stay constant, preferably in the form of a single half-wave away from the stiffener. As we saw, this mode change is affected by both the disbond length and its position.

Important things to take into consideration are that the aforementioned critical buckling loads and modes are influenced by both geometry and materials which in the case of composite structures is highly dependent on the lay-up. A model such as the one presented by Castro and Donadon [26], may be especially useful when designing a panel (with an initial disbond) which should have such specific buckling properties. These properties should include that local buckling of the skin occurs before global buckling and that the disbond may grow with a measurable amount without changing the buckling mode.

2.3. FATIGUE DELAMINATION AND DISBOND GROWTH

A disbond is similar to a delamination within a composite laminate, where two lamina are separating due to a matrix failure. As explained by Pascoe, Alderliesten and Benedictus [22], the delamination and disbonding mechanisms and prediction methods are very similar, both for fatigue and static propagation. We will therefore look primarily at fatigue models, however since they are often based on static models there will be some overlapping between fatigue models and their static counterparts. A brief discussion on the possible difference in damage mechanisms between fatigue and quasi-static crack growth is given in section 2.3.1.

Four different methods for fatigue delamination modelling are identified: Stress/strain methods, Linear Elastic Fracture Mechanics (LEFM) methods (section 2.3.2, Cohesive Zone Models (CZM) (section 2.3.3 and X-FEM. Stress/strain based models are not common in the context of fatigue crack growth modelling of a 2D crack front, their application is more suited to fatigue life prediction. Therefore stress/strain based methods are not covered in this study. Furthermore, incorporating an X-FEM model for fatigue is outside of the scope of this thesis and is therefore not included in this study. Due to the overlapping nature of CZM and LEFM methods, the reader is advised to read section 2.3.2 before reading section 2.3.3.

The **primary objective** is addressed in this section by means of an analysis of the proposed fatigue model and its origins. Furthermore, **objectives 1c, 1d and 3d** are covered, which in turn aims to answer **research question 1**. The relevance of this section to the thesis is therefore clear, in section 2.3.4 the novelty of the application is discussed.

2.3.1. QUASI-STATIC VS FATIGUE DAMAGE MECHANISMS

Before jumping into the models and methods for predicting delamination and disbond crack growth it is of interest to discuss what differentiates the two processes. Asp et al. [27] performed extensive tests on coupons made of HTA/6376C carbon/epoxy. Fractographic analysis showed that for mode I, mode II and mixed mode testing, the quasi-static samples showed fracture surfaces similar to their fatigue counterparts, the mechanisms were deemed to be identical. They did however note a slight difference in the shear cusps when comparing the pure mode II cases. For the fatigue case, the peaks were rounded and matrix rollers were visible. From analysis of low-cycle fatigue specimens they concluded that the mechanism at the crack tip was identical for quasi-static and fatigue loading.

In his doctoral thesis, Pascoe [28] also compared the fracture surface of aluminium strips bonded with a FM94 adhesive film, subjected to DCB testing. Pascoe notes a gradual change in fracture surface depending on the crack growth rate with the fatigue surface having a flatter appearance. This is said to indicate more plastic deformation for quasi-static crack growth. However, as was claimed by Asp et al. and noted by Pascoe; the smoother surface may be due to increased rubbing of the fracture surfaces at lower crack growth rates.

2.3.2. LINEAR ELASTIC FRACTURE MECHANICS METHODS (LEFM)

Fracture mechanics methods implement similitude parameters such as the stress intensity factor (SIF) or the strain energy release rate (SERR) to determine a certain crack growth length (a) per loading cycle (N). Due to

the complex stress field near a crack tip in composite materials, it is difficult to determine the stress intensity factor. This is why the SERR is most commonly used in fracture mechanic methods. It is shown by Irwin [29] that these similitude parameters (K & G) are equivalent and provide the same information.

The linear elastic fracture mechanics models available for delamination growth in composites are derived from the Paris relation [30, 31] shown in equation 2.1. Since the Paris equation was originally developed for metal materials, the SIF parameter, K, is shown in equation 2.4. Rans et al. show in [32] that the equivalent similitude parameter in terms of the strain energy release rate should be given by equation 2.6, with $\sqrt{\Delta G}$. However in many published papers on fatigue disbond growth [27, 33] equation 2.7 is used, with ΔG as a similitude parameter. Rans et al. demonstrate that the use of ΔG as a direct replacement of K in the Paris equation violates the principles of superposition used in LEFM.

$$\frac{da}{dN} = C \cdot \Delta K^m \tag{2.4}$$

$$\frac{da}{dN} = C \cdot \Delta G^m \tag{2.5}$$

$$\sqrt{\Delta G} = (\sqrt{Gmax} - \sqrt{G_{min}})^2 \tag{2.6}$$

$$\Delta G = G_{max} - G_{min} \tag{2.7}$$

There are many variations of the Paris equation in open literature, when used in the context of fatigue crack growth. Commonly, the similitude parameter, G_{max} or ΔG, is normalised with the critical strain energy release rate, G_c. However, since G_c is a constant obtained from quasi-static experiments it is only influencing the constant C in equation 2.5 and might as well be included there.

MODE MIX

In aerospace structures it is rare to encounter solely mode I or mode II crack propagation. It is therefore pertinent to establish a relation between these modes and how they affect the variables used in equation 2.5. Both the Paris equation variables, C and m, are subject to change. Furthermore, depending on how equation 2.5 is modified (ie. which similitude parameter is used) there may be other variables which need to be corrected for a mixed mode behaviour. We introduce the mode-mix ratio as defined by equation 2.8. Where the subscripts of G refer to the crack opening mode. Mode three crack growth is possible, as demonstrated by Donaldson and Mall [34] for graphite/epoxy composites and by Miura et al. [35] for glass fibre/epoxy systems at varying temperatures. However, mode III loading is rare and often negligible in magnitude when compared to mode I and mode II occurrence.

$$\phi = \frac{G_{II}}{G_I + G_{II}} \tag{2.8}$$

Benzeggagh and Kenane [36] proposed to correct for the mode mix ratio by altering the C and m terms in the Paris equation (2.5) using equations 2.9 and 2.10. They used equation 2.7 as the similitude parameter, divided by the critical fracture toughness, G_c. Although this is proven wrong by Rans et al. [32], the B-K interpolation method is independent of the similitude parameter used. The terms b and d are defined by Benzeggagh and Kenane as material specific properties. To correct the fracture toughness for mode mix, Benzeggagh and Kenane [37] proposed equation 2.11, again the parameter η is considered a material specific property. The values for b, d and η are all found by curve fitting experimental data.

$$logC = logC_{II} + (logC_I - logC_{II}) \cdot (1 - \phi)^b \tag{2.9}$$

$$m = m_I + (m_{II} - m_I) \cdot \phi^d \tag{2.10}$$

$$G_c = G_{Ic} + (G_{IIc} - G_{Ic}) \cdot \phi^{\eta} \tag{2.11}$$

Blanco et al. [38] studied various existing methods to correct for mode-mix in the Paris relation. Using data sets from various sources they showed that the mode-mix dependency is non-monotonic. To correct for mode mix, Blanco et al. [38] proposed the following mix-mode model (equations 2.12 and 2.13) to correct the C and m parameters in Paris' equation (eq. (2.5)). The subscript 'f' in equation 2.12 refers to curve fitted parameters for C and m. Note: the original notation has been changed in order to maintain consistency in this text. Blanco et al. found a good agreement between their proposed model and the fatigue crack growth behaviour samples of HTA/6376C carbon epoxy. The test data was obtained from Asp et al. [27]. The use of this mixed-mode correction introduces another 2 fitting parameters in addition to the existing 4 Paris coefficients (C_I, C_{II}, m_I, m_{II}) required for pure mode I and mode II fatigue crack growth prediction. These Paris coefficients are also curve fitted parameters describing a macroscopic behaviour rather than an inherent material property.

$$logC = logC_I + logC_f \cdot \phi + log\frac{C_{II}}{C_I \cdot C_f}\phi^2 \tag{2.12}$$

$$m = m_I + m_f \cdot \phi + (m_{II} - m_I - m_f) \cdot \phi^2 \tag{2.13}$$

Benzeggagh and Kenane, and Blanco et al. offer different methods for interpolating the Paris coefficients, C and m at different mode mixities. Furthermore, Benzeggagh and Kenane also proposed a model for interpolating the fracture energy, G, for different mode mixities. In the models described in section 2.3.3 it is common to use the B-K method for interpolating the G values, whilst the Blanco method is often used to interpolate the Paris coefficients.

VCCT METHODS

Commonly, when using FE methods, the virtual crack closure technique (VCCT) is applied to calculate the SERR values which are then used in conjunction with LEFM fatigue crack growth models. The principle of VCCT, is that the energy required to open a crack by a finite amount is equal to the work required to close that same crack. Furthermore, it is assumed that the state of the crack front does not change significantly as the crack propagates. Using the same notation as in fig. 2.8, the forces at node i can be used to calculate the work done at node l. The total energy thus to close the crack is given by eq. (2.14). When divided by the change in crack area (assuming an out-of-plane width of unity), the SERR for mode I and II are obtained using eqs. (2.15) and (2.16), respectively. The SERR In fig. 2.8 a 2D case is illustrated using 4-node elements, formulations for 3D applications exist but are not detailed here, for brevity.

$$E = \frac{1}{2} \cdot [X_i \Delta u_l + Z_i \Delta w_l] \tag{2.14}$$

$$E = \frac{-1}{2\Delta a} \cdot Z_i \Delta w_l \tag{2.15}$$

$$E = \frac{-1}{2\Delta a} \cdot X_i \Delta u_l \tag{2.16}$$

The largest drawback when using a VCCT method is that the model must be re-meshed as the crack propagates. Furthermore, an initial crack or notch must be present from which the crack front can propagate. These two drawbacks are eliminated when using a cohesive zone model, which is discussed in section 2.3.3.

2.3.3. COHESIVE ZONE MODELS (CZM)

Initial development of cohesive zone models can be traced back to the 1960s, where Dugdale [39] first formulated cohesive zones around the tip of slitted steel sheets. Barenblatt[40] is often cited along with Dugdale as one of the pioneers of cohesive zone models. In 1959 Barenblatt published two papers [41, 42] on equilibrium cracks formed under brittle fracture in metals. The second hypothesis presented in [42], based on

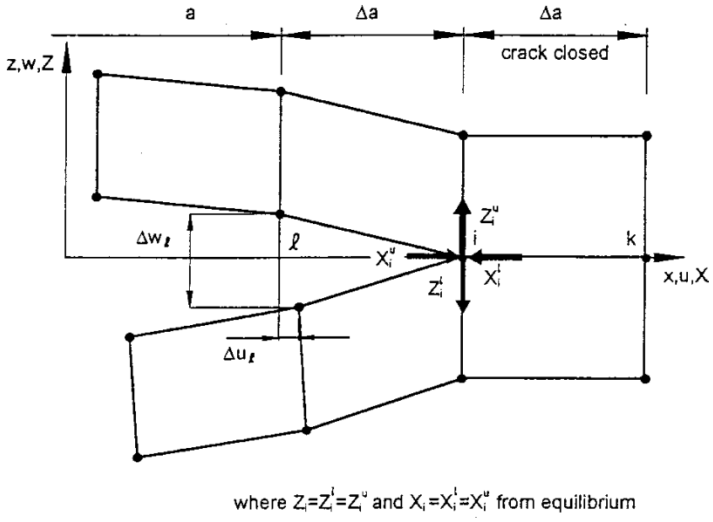

Figure 2.8: VCCT method for 4 node elements, obtained from [4]

the work in [41], forms the basis for the cohesive zone theory: "*The distribution of the displacements of the surface points of the end region of the crack does not depend on the acting loads and is always the same for the given material under given conditions. The cohesive forces, which attract the opposite edges of the crack toward each other, depend only on the distribution of the displacements in the end region; therefore, the hypothesis just stated, involves independence of these forces from the loads*". This hypothesis, along with the introduction of a 'cohesive modulus' in [41] forms the basis for the traction-separation laws used for cohesive zone models today.

The idea of cohesive zone models is to model solid 'cohesive' elements through which a (static/fatigue) crack propagates. When used in a typical composite lay-up the cohesive elements are placed between each ply. In the case of a bonded joint analysis, with either metal or composite adherends, the cohesive elements are used only on the bond interface area. The crack growth path must therefore be known and modelled as a series of cohesive elements as demonstrated in figure 2.9.

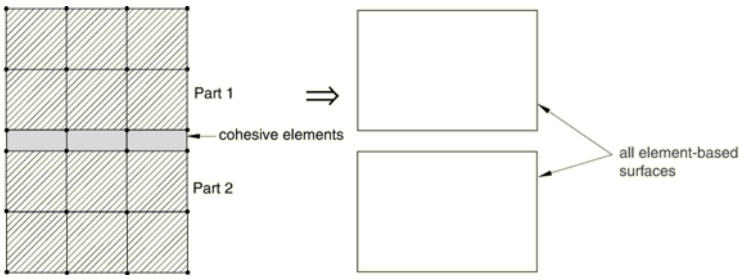

Figure 2.9: Cohesive elements, tied between two solid bodies, obtained from Abaqus 6.14 user manual [5]

The constitutive law used to degrade the cohesive elements can generally be defined by equation 2.17. Where the traction, T_i, is linear elastic up until δ_i^0 is reached. When this displacement (κ_i) is reached and surpassed, damage is introduced into the element by means of a damage parameter, D_i. If we look back at the quote from Barenblatt we see the link to a damage parameter driven solely by the displacement of the element nodes. This damage parameter softens the element stiffness and reduces the strength. An example bi-linear softening law is shown in fig. 2.11, albeit with different notation. Further description of the various damage laws is given in the following subsections for specific cohesive zone models.

$$\begin{aligned} T_i &= K_i \delta_i \quad \text{for} \quad 0 \leq \kappa_i < \delta_i^0 \\ T_i &= (1 - D_i) \cdot K_i \delta_i \quad \text{for} \quad \delta_i^0 \leq \kappa_i < \delta_i^f \\ T_i &= 0 \quad \text{for} \quad \delta_i^f < \kappa_i \end{aligned} \tag{2.17}$$

The elements are assigned the cohesive material properties in addition to a fatigue damage law (described in sections 2.3.3 to 2.3.3. With each fatigue load cycle the cohesive elements are degraded with a penalty factor defined by the damage law. Various damage parameters exist, in this paper the focus lies on the so-called split damage parameter, where the static and fatigue damage are determined separately before being combined to form the final damage value.

Another characteristic modelling technique common for these models is the use of the cycle-jump approach/load envelope approach, proposed by Peerlings et al. [43] and used by Robinson et al. [44] in a CZM formulation, whereby the entire loading/unloading cycle is not analysed explicitly. Rather, as is demonstrated in figure 2.10, the model is subject to a static load L_{max} which is held throughout the fatigue analysis. After the load has been applied (by means of a smooth ramp or polynomial), the fatigue law is activated and the fatigue damage is calculated for each 'virtual' fatigue cycle in an explicit time integration scheme. Computationally this is much cheaper than to simulate each loading/unloading cycle.

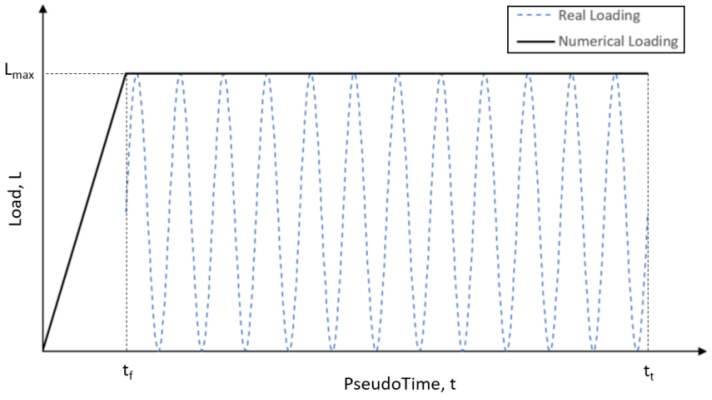

Figure 2.10: Numerical fatigue load cycles, obtained from Oliveira [6]

TURON MODEL

A major breakthrough in the field of CZM was made by Turon et al. [7] by combining LEFM with the FE principles of CZM and using the Paris law to equate crack growth. Turon et al. equate the damage parameter D_i (as described in equation 2.17) to microcrack density in the adhesive/interface material. This in turn means that the damage variable D may be interpreted as the ratio of damaged area A^D to pristine area A^0, when discretized in a FE model this is represented by equation 2.18. Next, in conjunction with a linear softening law as described in figure 2.11, the damage ratio in equation 2.18 is expressed in terms of dissipated damage energy (ξ) and the critical energy release rate, G_c.

$$\bar{D} = \frac{A^D}{A^0} = \frac{\xi}{G_c} \tag{2.18}$$

In order to implement this numerically, the constitutive law is changed to a bi-linear softening law, which includes an initial linear elastic behaviour. This is defined using a penalty stiffness K, resulting in an onset displacement jump, Δ^0. A comparison between the numerical and analytical constitutive laws is presented in figure 2.11, with the ideal analytical model on the left hand side. We can see that the numerical model on the right has the steep initial stiffness, this is necessary to avoid the numerical singularity seen in the analytical model at a zero displacement.

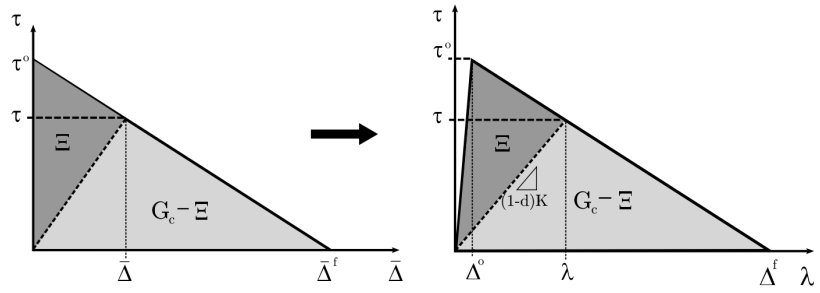

Figure 2.11: Linear and Bi-Linear softening law, obtained from Turon et al. [7]

$$\frac{A^D}{A^0} = \frac{D\Delta^0}{\Delta^f(1-d)+D\Delta^0} \tag{2.19}$$

The novelty of their research lies in the formulation of the fatigue damage parameter. By utilizing the crack growth per cycle ($\frac{\partial A}{\partial N}$), as is defined by the Paris equation, and using the damaged area ratio found in equation 2.19, the damage per cycle can be obtained. Equation 2.20 summarizes the damage, d, per fatigue cycle, N, with the cohesive zone, A_{CZ}, defined by Rice's equation 2.21, where b is the delamination front width, τ^0 is the interfacial strength, E_3 is the Young's modulus in the perpendicular direction and G^{max} is the maximum energy release rate per cycle.

$$\frac{\partial D}{\partial N} = \frac{1}{A_{CZ}} \frac{(\Delta^f(1-d)+D\Delta^0)^2}{\Delta^f\Delta^0} \frac{\partial A}{\partial N} \tag{2.20}$$

$$A_{CZ} = b\frac{9\pi}{32}\frac{E_3 G^{max}}{(\tau^0)^2} \tag{2.21}$$

Turon et al. make use of the Blanco interpolation to determine the mix-mode Paris coefficients and a B-K relation for the fracture toughness, these are described in further detail in section 2.3.2.

A limitation with the Turon model is the computation of the cohesive zone ahead of the crack tip. For 1D cases such as a DCB or 4ENF experiment, the width (b, in equation 2.21) is known and remains constant, a sigle element may be used across the width of the model. However in a 2D case (for example a stiffener panel), where the crack front may propagate asymmetrically, this value for the delamination front width, b, may be more difficult to establish. This problem of predicting crack propagation in situations other than simple 1D models (4ENF, DCB and MMB), is a recurring problem in CZM, one which is addressed in section 2.3.3 by a non-local crack tracking scheme proposed by Kawashita et al. [45].

HARPER-HALLETT MODEL

Harper and Hallet [46] continued with the idea of linking fracture mechanics with a Paris law fatigue damage description, introduced by Turon [7]. Their damage parameter is defined by equation 2.22, where the total damage is split into a static and a fatigue portion.

$$D_{tot} = d_s + d_f \tag{2.22}$$

The static damage is controlled by a mixed-mode bi-linear traction separation law, as seen in figure 2.11 and given by equation 2.23. The fatigue damage portion is linked to the cyclic variation in fracture energy, which is used in combination with a Paris equation to obtain a crack growth rate, $\frac{\delta a}{\delta N}$ (see equation 2.24).

$$d_s = \frac{\delta - \delta_0}{\delta_f - \delta_0} \tag{2.23}$$

$$\frac{da}{dN} = C\cdot\left(\frac{\Delta G}{G_c}\right)^m \tag{2.24}$$

where Δ_G is obtained by eq. (2.25):

$$\Delta G = (1 - R^2) \cdot G_{max} \tag{2.25}$$

$$\frac{\delta d_f}{\delta N} = f(L_{CZ}, \frac{da}{dN}) \tag{2.26}$$

In order to obtain the fatigue damage per cycle (eq. (2.26)), $\frac{\delta d_f}{\delta N}$, two inputs are required: the crack growth per cycle $\frac{da}{dN}$ and the cohesive zone length L_{CZ}. The cohesive zone length is obtained from a quasi-static analysis of a model with elastic cohesive properties (equation 2.26). It is then argued in [46] that half of this cohesive zone experiences fatigue damage, whilst the other half experiences pure static damage. The validity of this statement for conditions with complex crack fronts is questionable, as the mode mix and cohesive zone length will vary along the crack front as it grows. Harper and Hallett themselves admit that this distribution of fatigue vs static zone length requires further investigation.

KAWASHITA/HARPER-HALLETT MODEL

Hallett and Kawashita [45], re-formulate the fatigue damage per cycle (equation 2.26) to include the element length rather than the cohesive zone as an input. This drastically reduces the effort on the user, since no initial static model is required to determine the cohesive zone length. Nixon-Pearson et al. [33] used the same model but with variable size cohesive elements, and assuming squareness, took the square root of the element area to estimate the element length.

Kawashita and Hallet [45] further improved the Harper-Hallett model by implementing a non-local scheme for determining the crack growth direction. By identifying cohesive elements close to crack fronts the propagation direction and effective cohesive length may be computed. As demonstrated by Harper and Hallet [47] the cohesive zone is geometry and load dependent, for complex models the crack front will not be 1 dimensional like in a DCB or 4ENF model. Both the Turon model and the Harper-Hallet model require user input regarding the cohesive zone. By removing this dependency from the user inputs the analysis may be simplified. The term L_{CZ} in equation 2.26 is calculated automatically, regardless of the crack growth direction.

An overview is made of all the fitting parameters required for the Kawashita/Harper-Hallett model (ie. not including the material stiffness, yield strength and the critical strain energy release rates). This includes the static and fatigue portion of the damage formulation. The energy release rates are considered material properties whilst the Paris coefficients are considered fitting parameters. Therefore the total number of fitting parameters is 7.

- B-K coefficient for critical energy release rate interpolation (1 parameter)
- Paris coefficients: C and m (mode I and II = 4 parameters)
- Blanco coefficients for interpolating Paris coefficients (2 parameters)

SUMMARY OF COHESIVE ZONE MODELS

These four Cohesive Zone Models implementing fatigue damage in composite delamination growth are but a selection of the numerous models published over the previous years. Common to all CZMs described previously is the incorporation of fitting parameters, used to describe macroscopic behaviour, rather than an intrinsic material characteristic. If we look back at section 2.1.4, where the influence of fibre bridging on the fatigue crack growth rate was shown, we see that even the Paris coefficients are not purely describing the matrix or cohesive behaviour, but also the influence of the adherends on the crack propagation. This essentially adds the Paris coefficients to the list of fitting parameters.

The early models by Turon and Harper/Hallett incorporate additional estimation to determine the cohesive zone ahead of the crack tip. These estimations are limited to 1D crack propagation and thus unsuitable for more complex crack fronts. The approach suggested by Kawashita et al. (with or without the crack tracking algorithm) is the most suitable for 2D crack fronts and is therefore the primary candidate for this thesis

work. This is further confirmed by Oliveira et al. [6], who performed an investigation into the various fatigue cohesive zone models and applied them on coupon level models such as DCB, MMB and 4ENF. Comparing the Turon, Robinson and Hallett/Kawashita model he noted that the overal robustness and accuracy of the Hallett/Kawashita model made it a better candidate for fatigue crack growth prediction.

2.3.4. A NOTE ON MODELLING SCALE AND VALIDATION

Common to most of the fatigue crack growth modelling discussed above, is the limited scale for which the models have been validated. As mentioned, most researchers have limited the scope to single mode specimens at the coupon level. The DCB, 4ENF and mixed mode bending are some of the standard tests to which the models have been applied (the bottom level in fig. 2.12). Very few have taken the step to sub-component level with, for example, stiffened panels. Even then, research is mostly focused on static crack growth rather than fatigue crack growth. In order to use cohesive zone models on a larger scale, ie. moving from research application to industry application, it is imperative to increase the scale of validation and to include fatigue damage on the (sub-)component level, which is a driving design criterion in the aerospace industry.

The aim of this thesis, as stated in section 1.1, is to apply this class of fatigue models to a larger scale structure. By modelling at the sub-component level, the model's robustness and ability to predict the advancement of a 2D crack front is tested. In fig. 2.12 this is illustrated as the second layer from the bottom, the base layer being coupon level. It is an affordable scale of testing, when compared to the component and full aircraft scale, whilst allowing for more complex geometry and loading conditions to be simulated. So far, the author is not aware of any cohesive zone models with static and fatigue damage formulation being applied to stiffened reinforced panels.

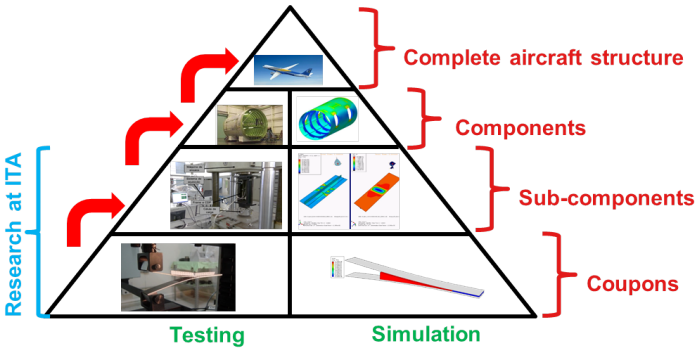

Figure 2.12: Numerical and experimental modelling scale: from coupon level to full structure. Image by: Mauricio V. Donadon

3

APPROACH/METHOD

This chapter serves to give a chronological overview of the research project, including the revisions and lessons learnt throughout the project. Three main phases of the project are identified: static testing/modelling, fatigue testing/modelling and finally residual strength testing/modelling. As mentioned in the introduction, this thesis is the first of a large series of fatigue tests and models. In total, six series of tests are planned (three bonding technologies at two different environmental conditions). Following the method below will ensure a coherent final data set, allowing comparison and analysis between the various series. By no means is it a complete or foolproof set of instructions, however it serves as a foundation for the future test series to build upon and improve.

3.1. PHASE I - STATIC MODELS AND TESTS

The initial phase consists of familiarization with the problem at hand and preparing the initial Abaqus models. A total of three different models are made: 1) linear buckling analysis, 2) general static (without damage), 3) dynamic/explicit with damage formulation in the composite and cohesive elements. The linear buckling analysis serves as input for both the static/general and the dynamic/explicit models. A convergence study is performed on the models to determine the required level of mesh refinement. Finally, an element level verification is performed on the utilized element types. These models are described in full in chapter 4.

The phase I models are validated by means of quasi static testing of a stiffened panel. Under load control, a compressive test is performed on a panel, instrumented with strain gauges on the skin and stiffener. The buckling load is calculated by locating the strain reversal point. Using the buckling load, the linear buckling model is validated, in addition to the buckling loads of the static/general and dynamic/explicit models. Load shortening data is obtained from a load-cell and an LVDT sensor, which is also used to validate the general/static and dynamic/explicit models. In chapter 5, full overview of the test set-up, results and model validation are presented.

3.2. PHASE II - FATIGUE MODEL AND EXPERIMENT

Following the phase I model validation, a fatigue sub-routine is implemented in the Abaqus explicit model, replacing the Abaqus cohesive elements (COH3D8) with solid elements controlled with a VUMAT user subroutine. An adapted version of the cohesive zone model proposed by Kawashita et al. [45] is implemented in the sub-routine. Various adaptations must be made to the Abaqus model initially presented in 4 to run it in a time-effective manner. The model changes, results and recommendations are discussed in chapter 7.

A series of fatigue tests are performed to provide validation data for the fatigue model proposed in chapter 7. Due to this being the first test series in the global INOVA project, an estimation is made of the fatigue loading parameters using a low fidelity VCCT technique. Next, a sacrificial panel is tested and the fatigue loads calibrated. The basis of the experimental data are numerous c-scan images, made throughout the fatigue life of the panel. This is to capture the advancement of the crack front. Furthermore, intra-laminar

fatigue damage is monitored by performing quasi-static tests throughout the fatigue life. The variation of the load-shortening curve will give indication of fatigue damage in the panel skin or stiffener. Finally, some adjustments were made to the test rig as a result of the initial testing performed on the sacrificial panel. The test set-up, results and fatigue model validation are discussed in chapter 8.

3.3. PHASE III - RESIDUAL STRENGTH

Once the fatigue models are complete, the remaining strength of the panels must be determined. By importing the damage in the cohesive layer into a new model, the ultimate load of the fatigued panels may be estimated. Some assumptions and limitations are present, which are described, along with the model, in chapter 9. Ultimate load testing is performed in a similar manner to the tests performed in chapter 5. From which, the data is used to validate the residual strength model. The test results and model validation are also presented in chapter 9.

3.4. FLOWCHART

An overview of the various phases is presented in the flowchart below (image 3.1). This includes all the modelling, testing and validation work performed.

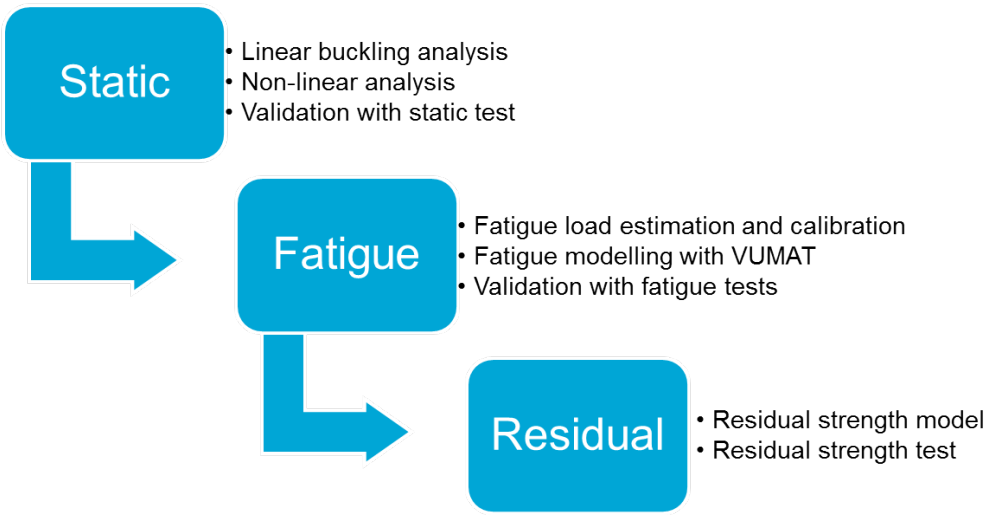

Figure 3.1: Flowchart of the project work: modelling, testing and validation

An overview of the various panels and their identification number are given below:

Table 3.1: Overview of panels used

Panel ID	Phase
401_01	Initial static
401_02	Fatigue calibration
401_03	Fatigue and Residual
401_04	Fatigue and Residual
401_05	Fatigue and Residual
401_06	Fatigue and Residual

PHASE I - STATIC

4

QUASI-STATIC MODELLING

A total of three different types of models are created in the commercial FE software, Abaqus. The first model, a linear buckling (eigenvalue) analysis, serves as input for the two subsequent types of models. The buckling mode and nodal displacement of the eigenvalue analysis is input in a static general and a dynamic/explicit analysis. These shall be referred to from now on as the eigenvalue, static general and explicit models, respectively. The static general analysis serves both as an intermediate step towards the explicit model, additionally it is used to estimate the fatigue test load parameters. Both the eigenvalue analysis and the static general analysis, serve as bases for mesh convergence studies. In all three models it is essential to utilize an identical mesh, to ensure that the input from the eigenvalue analysis works properly in the static and dynamic models.

In section 4.1 the Abaqus model geometry and modelling strategy is shown and compared to the physical panel. Here the material properties are also presented. The convergence studies and analysis results of the eigenvalue and static general analyses are presented in sections 4.2 and 4.3, respectively. Material damage parameters are introduced in the dynamic model, warranting an element level verification. The details of the dynamic model and the results are discussed in section 4.4. Validation of the models is based on experimental testing, both of which are presented in chapter 5.

4.1. MODEL OVERVIEW

In fig. 1.2, the physical cross-section and lay-up is shown. It consists of a T-stiffener bonded to a flat skin panel. A 3-dimensional view of the panel is presented in fig. 4.1, along with the proposed boundary conditions to be applied during experimental testing. An initial defect is introduced in the physical panel by means of a Teflon film, inserted midway between the two load application ends. This film has the same width as the stiffener base and a length of 100mm. The disbonded area is shown in fig. 4.2 as the area between the two highlighted red lines. These red lines are the initial crack fronts in the model.

4.1.1. BOUNDARY CONDITIONS

Note that the panel ends are to be clamped, whilst the edges of the skin are to be constrained in out-of-plane displacement by so-called buckling constraints. These are designed to limit the mode I opening of the skin from the stiffener, which would be significantly more pronounced in the absence of the buckling constraints. In reality, there is rarely a single stiffener on a skin panel (eg. in a wing box), therefore, the skin in-between two stiffeners will not be entirely free to move in the out-of-plane direction. On the other hand, a simply supported boundary condition, as is proposed in fig. 4.1, may slightly over constrain the skin compared to a real life situation. This boundary condition was chosen by the INOVA project managers and as such the decision falls outside of the scope of this thesis. As demonstrated in fig. 4.1, an axial load is applied to the panel. In the model one side is kept fixed, whilst a compressive load is applied on the other face of the panel.

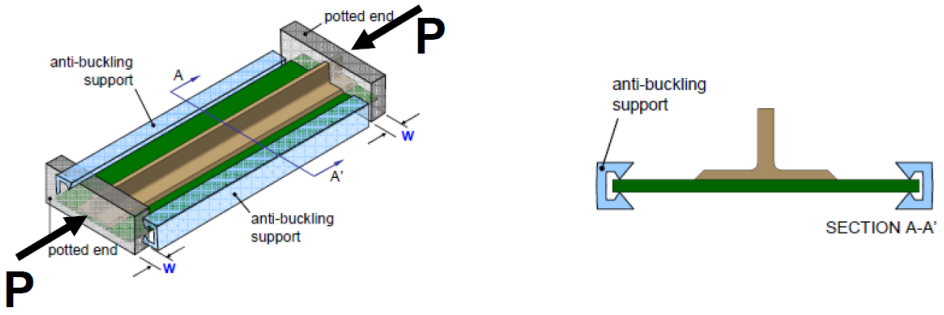

Figure 4.1: 3D view of the simulated panel with boundary conditions

A NOTE ON THE PANEL DESIGN

This stiffener reinforced panel is typical for a stiffened skin section from either an aircraft wing or fuselage. Automotive or maritime industries, may utilize similar constructions at the same or different scale. It must be noted however, that the composite lay-up is quasi-isotropic, using an equal number of plies in just 4 directions $(0, 90, \pm 45)$. Such a 'black aluminium' lay-up is an inefficient design, in terms of weight, and is not common in well engineered design solutions for specific structural problems, such as a fuselage section. The lay-up design was determined by engineering professionals at Embraer (a Brazilian aerospace OEM) and thus lies outside of the scope of this thesis project. Furthermore, since the focus of the INOVA research project is on the durability of bonded joints the composite lay-up is of secondary concern.

4.1.2. MODELLING APPROACH

In order to maintain an efficient simulation time, some approximations must be introduced in the numerical model, compared to the real-life physical stiffened panel. The composite skin and stiffener sections are modelled as shells, whereas the cohesive layer, bonding the stiffener to the skin, is modelled as two slabs. The disbond is simply modelled by the absence of a cohesive solid, in the centre of the panel length. This is illustrated in fig. 4.2, where an exploded view of the panel model is presented. The gap between the two sections of cohesive material is where the Teflon film is located in the physical panels. Finally, the skin and stiffener are tied to the cohesive elements by means of a tie constraint.

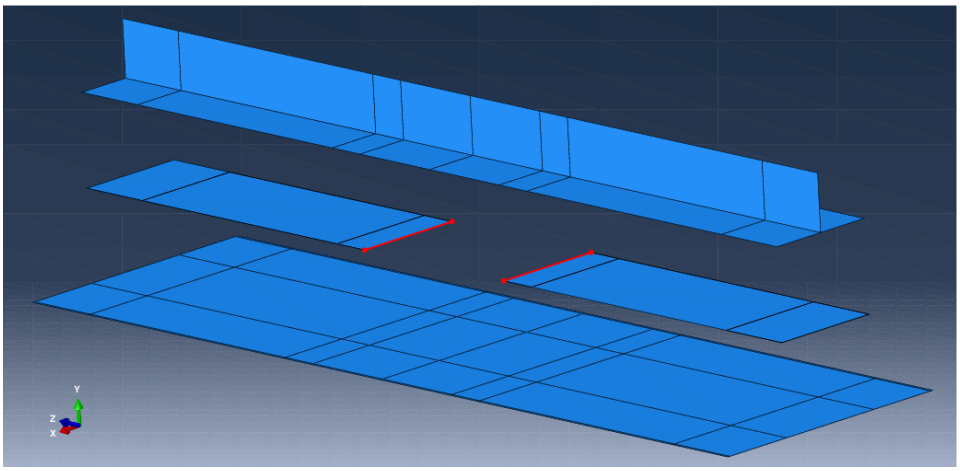

Figure 4.2: Abaqus model - exploded in y-direction. The stiffener and skin (top and bottom parts, respectively, are joined by two cohesive sections. The initial crack fronts on the cohesive sections are highlighted in red.

4.1.3. MATERIAL PROPERTIES

A T800-3900 pre-preg tape is used to manufacture the skin and stiffener. The material data sheet is presented in table 4.1. All panels were cured according to the supplier recommended temperature and pressure cycle

in an autoclave. Once cured, the panels were stored in a temperature controlled clean room. Both the eigenvalue analysis and the static analysis use these values as input. For the linear elastic cohesive elements, the transverse tape properties from table 4.1 are used. Material damage parameters introduced in the dynamic analysis are detailed in section 4.4.

Table 4.1: Material data sheet - T800-3900-2B pre-preg tape

Description	Magnitude	Unit
Strength		
Tensile S_{1t}	2793	MPa
Compression S_{1c}	1432	MPa
Tensile S_{2t}	36	MPa
Compression S_{2c}	226.8	MPa
Interlaminar Shear S_{12}	88.1	MPa
In-plane Shear at 5% $\pm 45^o$ S_{12}	63.8	MPa
Modulus		
Tensile E_{1t}	142-173	GPa
Compression E_{1c}	125-153	GPa
Tensile E_{2t}	7.8-9.6	GPa
Compression E_{2c}	9.9-12.1	GPa
In-plane Shear at 5% $\pm 45^o$ G_{12}	3.5-4.3	GPa
Poisson		
Tensile ν_{1T}	0.343	-
Tensile ν_{2T}	0.024	-
Compression ν_{1C}	0.339	-
Compression ν_{2C}	0.015	-

4.1.4. MESHING STRATEGY

The region of interest in the Abaqus shown in fig. 4.2 is near the edges of the cohesive elements, in the centre of the panel where the disbond is located. As such, a seed bias is introduced in order to accurately capture the model behaviour in this region. Figure 4.3 depicts an example of how the model is meshed. Note that care is taken to ensure an identical mesh on the skin-cohesive and stiffener-cohesive interfaces. A critical meshing criterion is that only a single element must exist in the thickness direction of the cohesive section (section 32.5.3 of the Abaqus user guide [5]).

A mesh refinement study is performed for the eigenvalue and the static model. In both cases the seed bias ratio is kept constant. In the two models, two different convergence criteria are used. It is assumed that the mesh found to be sufficiently refined for both of the models is also adequate for the subsequent dynamic model.

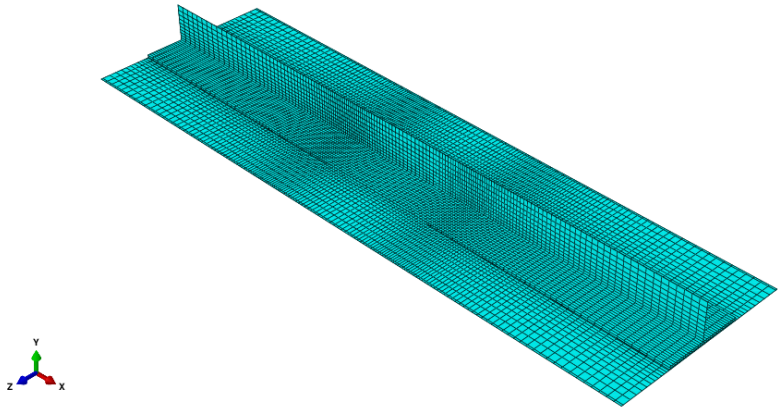

Figure 4.3: View of meshed Abaqus model with seed bias towards crack fronts

4.2. LINEAR BUCKLING/EIGENVALUE ANALYSIS

A linear buckling analysis serves as an input for the subsequent non-linear analyses such as the static general and dynamic/explicit simulations in this report. The node output file of the first buckling mode is used as an input in the non-linear analyses using the *IMPERFECTION command. Furthermore it serves as a first order buckling load and mode determination, which have high value at a relatively low effort on the user. When using unity as the input load, the eigenvalue output is the buckling load in newtons. An example result output is shown in fig. 4.4, note that the deformation scale is exaggerated by a factor 50. As is evident, the skin buckles in the disbonded region, detailed results are presented in section 4.2.2.

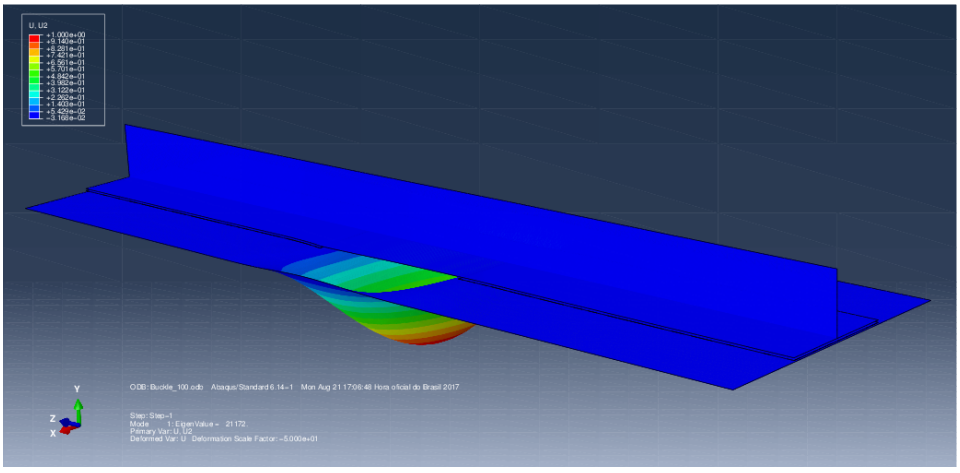

Figure 4.4: Example buckling result of an eigenvalue analysis. Deformation, scale factor = 50x.
Displayed variable = out-of-plane displacement (model y-axis)

4.2.1. MESH CONVERGENCE

A convergence is study is performed to determine the required level of mesh refinement. Throughout the convergence study, the same seed bias ratio is maintained. 5 different mesh refinements were tested, the coarsest having 5x5mm elements near the crack front and the finest having 1x1mm elements near the crack front. The obtained eigenvalues are used as a convergence parameter. A mesh is considered 'converged', if its first eigenvalue is within 1% of the eigenvalue of the previous model. The convergence results for the first eigenmodes are plotted in in fig. 4.5. In total, 5 eigenvalues were requested as output from the Abaqus linear buckling analysis. All 5 showed the same convergence behaviour as the first eigenvalue. The mesh with 2x2mm elements was selected based on the aforementioned criteria.

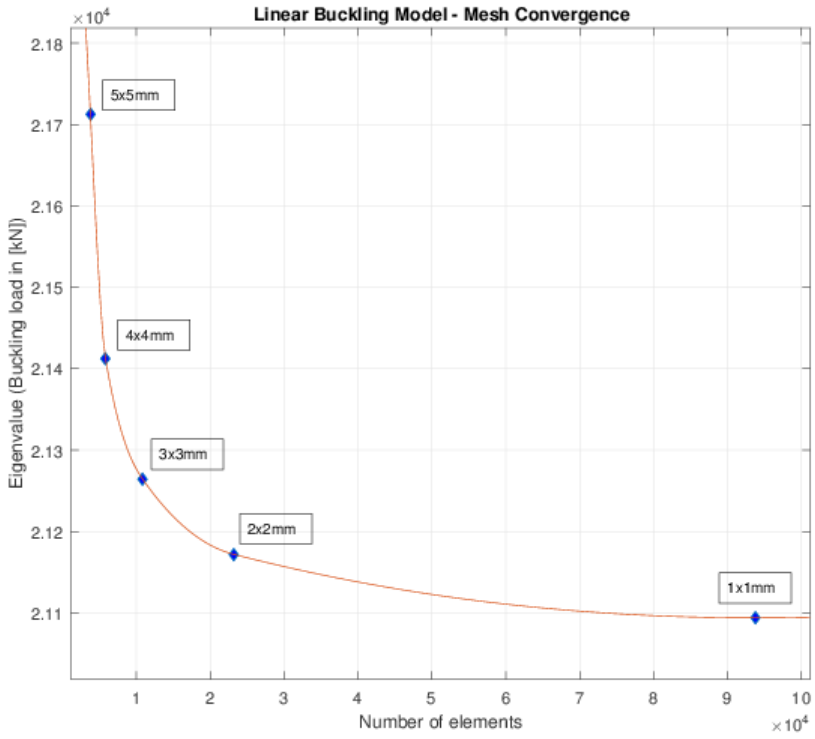

Figure 4.5: Convergence of eigenvalue analysis - Buckling load vs no. of elements

4.2.2. RESULTS

The eigenvalue analysis was performed for models with varying disbond size, ranging from the initial 100mm (the length of the teflon tape insert), up to 140mm. An exponentially decreasing trend can be observed; as the disbond size increases, the buckling load decreases. This is as expected, because as the disbond grows, the length to width ratio of the skin section increases, leading to a lower buckling load. This behaviour is also reported in chapter 2.

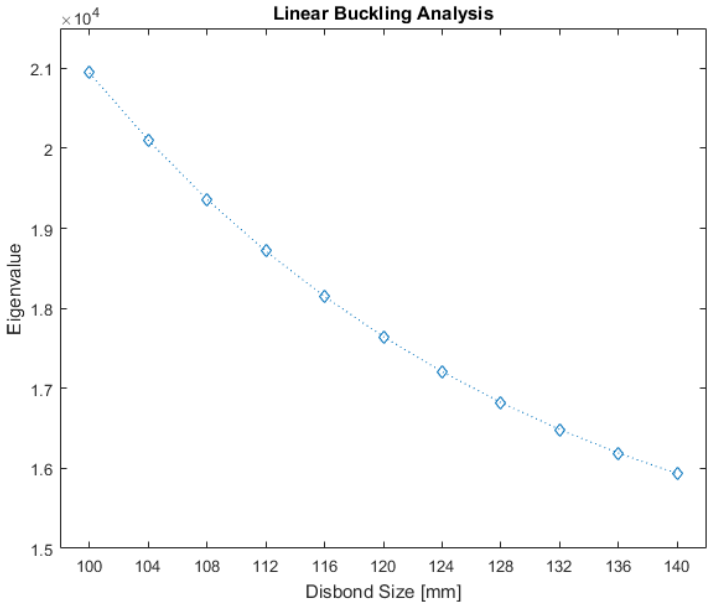

Figure 4.6: Buckling load vs disbond length, (first buckling mode only). The eigenvalue on the y-axis is equal to the buckling load.

4.3. ABAQUS: STATIC GENERAL

Several purposes are served by the static general model. Firstly, it is a computationally cheap method of debugging and verifying the global model behaviour compared to running a dynamic/explicit model. In this way boundary conditions and constraints (such as ties) are checked. Secondly, the load shortening curve may be validated using experimental data (shown in section 5.3), this validates the material input. This can in turn be used to verify the explicit model behaviour in section 4.4. Thirdly, a second mesh convergence study is performed to confirm the mesh choice in section 4.2.1. Fourthly, it is used in section 6.1 to estimate the fatigue load amplitude required for slow, measurable growth.

The Abaqus static general model uses the linear elastic material properties as presented in table 4.1.

In fig. 4.7 preliminary result is shown of the deformation of the skin when the model is subject to a compressive load. A clear diagonal buckling pattern is visible on the skin, which is attributed to the +45 plies on the outside of the lay-up (see fig. 1.2). In fig. 5.5 the load shortening response of the non-linear static general model is presented, along with experimental data. Furthermore, the buckling loads of the model will be validated using experimental data.

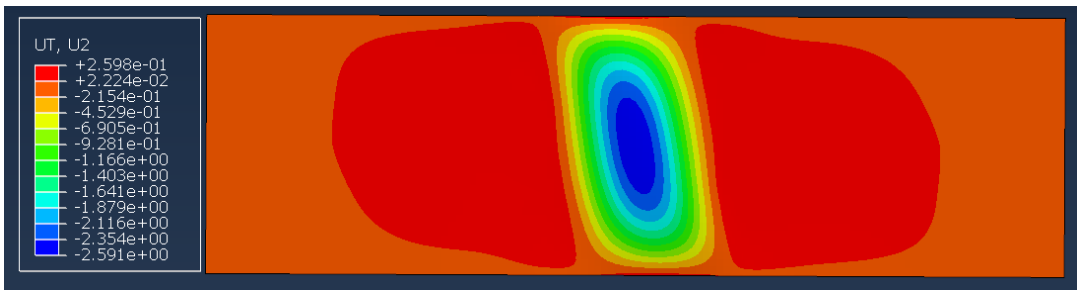

Figure 4.7: Skin buckling pattern at -50kN compressive load, displayed variable is displacement in out-of-plane direction.

4.3.1. MESH CONVERGENCE

The same meshes as described in section 4.2.1 are used in a load controlled static general analysis. To determine convergence, the total strain energy at a load of -50kN is used because this variable will be used in section 6.1 to estimate the fatigue load parameters.

A mesh is deemed to be converged when its total strain energy is within 1% of the energy obtained with the previous (coarser) mesh. In fig. 4.8 the results of the mesh convergence study are presented. The 2x2mm mesh, which was selected after the convergence study in section 4.2.1, is well within the convergence criteria. Compared with the previous mesh it has a difference in internal energy of less than 0.05%. The results of the convergence study are plotted in fig. 4.8.

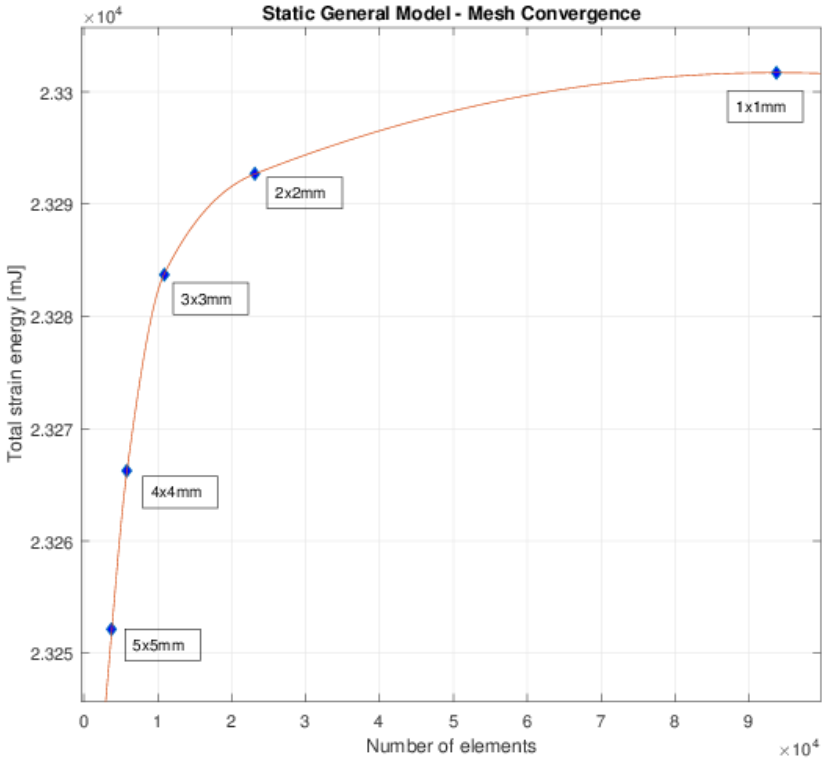

Figure 4.8: Convergence results of static general analysis

4.4. ABAQUS EXPLICIT

Material damage parameters are introduced in the dynamic model, both in the composite elements and the cohesive elements. The dynamic explicit model is created because it will be the basis for the fatigue model. It is introduced here in the quasi-static analysis as a stepping stone to the fatigue model presented in chapter 7 and the residual strength model presented in chapter 9.

Mesh convergence is assumed to follow from the two convergence studies performed in sections 4.2.1 and 4.3.1. This is based on the assumption that mesh dependency is alleviated through the inclusion of a characteristic element length formulation in damage law described in section 4.4.2. See section 23.3.3 of the Abaqus user guide [5] for further details on the characteristic length formulation.

The explicit model is subject to a displacement controlled compression, until failure. By including damage formulations for both the composite and the cohesive section connecting the stiffener and skin, the failure mechanism and load should be captured. This will be validated in chapter 5.

Table 4.2: Material properties for composite section

Property	Value	Unit
Modulus		
E1	1250000	MPa
E2	9900	MPa
μ_{12}	0.339	-
G_{12}	3500	MPa
G_{13}	3500	MPa
G_{23}	3500	MPa
Strength (S)		
Longitudinal tension	2793	MPa
Longitudinal compression	1432	MPa
Longitudinal shear	63.8	MPa
Transverse tension	36	MPa
Transverse compression	226.8	MPa
Transverse shear	88.1	MPa
Fracture toughness (G)		
Longitudinal tension	165	kJ/m^2
Longitudinal compression	25	kJ/m^2
Transverse tension	10	kJ/m^2
Transverse compression	2	kJ/m^2

Table 4.3: Material properties for adhesive section (using Abaqus notation; n=normal, 1=first shear, 2=second shear)

Property	Value	Unit
Modulus		
E/E_{nn}	2970	MPa
G_1/G_{ss}	1080	MPa
G_2/G_{tt}	1080	MPa
Strength		
S_n	50	MPa
S_1	180	MPa
S_2	180	MPa
Fracture toughness		
G_n	0.1825	kJ/m^2
G_1	1.16	kJ/m^2
G_2	1.16	kJ/m^2
B-K criterion	6.72	-

4.4.1. MATERIAL PROPERTIES

In tables 4.2 and 4.3, the material properties are presented. In addition to the strength and stiffness (as was used in the eigenvalue and static general model), fracture toughness properties are included. Furthermore, the B-K constant for the cohesive is included in table 4.3. This value was found by Brito [48] as part of a previous investigation at coupon level on the same composite material. Finally, the cohesive material properties, given in table 4.3 are obtained from experimental studies (at coupon level) reported by Arbelo [49] as part of the INOVA project by FAPESP.

4.4.2. HASHIN DAMAGE INITIATION AND EVOLUTION

Two different damage models are used in the dynamic model. For the composite stiffener and skin, a Hashin initiation criterion is used with an energy damage propagation law. Cohesive elements with a bi-linear softening law are used to model the solid interface section between the stiffener and skin (see fig. 4.2 for the model overview).

The Hashin failure criterion for damage initiation is used as it is available in Abaqus (section 24.3.2 of the

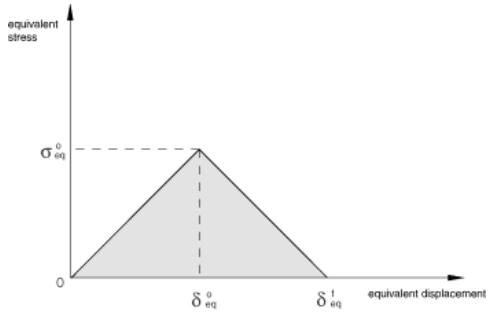

Figure 4.9: Bi-linear softening law for stress-displacement relation

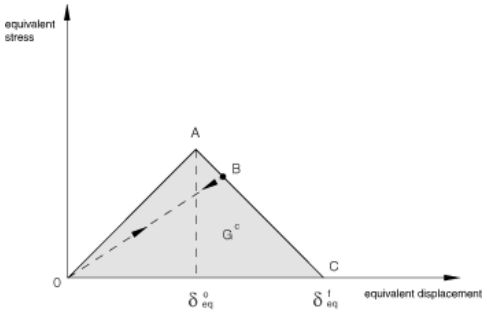

Figure 4.10: Damage variable vs equivalent displacement

Abaqus Analysis User's Guide [5]). It is based on Hashin's theory [50], taking into account fibre and matrix failure in both compression and tension. The equations governing the damage initiation are presented in eqs. (4.1) to (4.4).

$$F_f^t = \left(\frac{\hat{\sigma_{11}}}{X^T}\right)^2 \tag{4.1}$$

$$F_f^c = \left(\frac{\hat{\sigma_{11}}}{X^C}\right)^2 \tag{4.2}$$

$$F_m^t = \left(\frac{\hat{\sigma_{22}}}{Y^T}\right)^2 + \left(\frac{\hat{\tau_{12}}}{S^T}\right)^2 \tag{4.3}$$

$$F_m^c = \left(\frac{\hat{\sigma_{11}}}{2S^T}\right)^2 + \left[\left(\frac{Y^C}{2S^T}\right)^2 - 1\right] \cdot \frac{\hat{\sigma_{22}}}{Y^C} + \left(\frac{\hat{\tau_{12}}}{S^L}\right)^2 \tag{4.4}$$

Where:

- X^T = longitudinal tensile strength
- X^C = longitudinal compressive strength
- Y^T = transverse tensile strength
- Y^C = transverse compressive strength
- S^L = longitudinal shear strength
- S^T = transverse shear strength
- $\hat{\sigma_{11}}, \hat{\sigma_{22}}, \hat{\tau_{12}}$ = components of the effective stress tensor $\hat{\sigma}$ in eq. (4.5).

$$\hat{\sigma} = \mathbf{M}\sigma \tag{4.5}$$

Where σ is the true stress and $\mathbf{M}$ is the damage operator:

$$M = \begin{bmatrix} \frac{1}{(1-d_f)} & 0 & 0 \\ 0 & \frac{1}{(1-d_m)} & 0 \\ 0 & 0 & \frac{1}{(1-d_s)} \end{bmatrix} \tag{4.6}$$

Following the Hashin damage initiation a progressive, energy based, damage evolution law is implemented for the composite sections. The linear damage evolution is illustrated in fig. 4.9. Where the integral of the stress-displacement curve for an element must be equal to the fracture energy to satisfy the failure condition. The damage operator presented in eq. (4.6) is a result of this damage evolution. With the damage variables d_f, d_m and d_s given by eqs. (4.7) to (4.9).

$$d_f = \begin{cases} d_f^t \ \ if \ \ \hat{\sigma_{11}} \geq 0 \\ d_f^c \ \ if \ \ \hat{\sigma_{11}} < 0 \end{cases} \tag{4.7}$$

$$d_m = \begin{cases} d_m^t \ \ if \ \ \hat{\sigma_{22}} \geq 0 \\ d_m^c \ \ if \ \ \hat{\sigma_{22}} < 0 \end{cases} \tag{4.8}$$

$$d_s = 1 - (1 - d_f^t)(1 - d_f^c)(1 - d_m^t)(1 - d_m^c) \tag{4.9}$$

Where the term d is given by eq. (4.10), presented here for a generic case. Equation (4.10) follows the behaviour presented in figs. 4.9 and 4.10. The superscript 0 indicates displacement where damage initiates, whilst the superscript f indicates failure displacement.

$$d = \frac{\delta_{eq}^f(\delta_{eq} - \delta_{eq}^0)}{\delta_{eq}(\delta_{eq}^f - \delta_{eq}^0)} \tag{4.10}$$

Where the equivalent displacements, δ_{eq}, are given by eqs. (4.11) to (4.14), with the superscript denoting the damage mode (ft = fiber tension). The Macaulay bracket $\langle\cdot\rangle$ is the operation given in equation 4.15.

$$\delta_{eq}^{ft} = L_c \cdot \langle \epsilon_{11} \rangle \tag{4.11}$$

$$\delta_{eq}^{fc} = L_c \cdot \langle -\epsilon_{11} \rangle \tag{4.12}$$

$$\delta_{eq}^{mt} = L_c \cdot \sqrt{\langle \epsilon_{11} \rangle + \epsilon_{12}^2} \tag{4.13}$$

$$\delta_{eq}^{mc} = L_c \cdot \sqrt{\langle \epsilon_{11} \rangle + \epsilon_{12}^2} \tag{4.14}$$

$$\langle \alpha \rangle = (\alpha + |\alpha|)/2 \tag{4.15}$$

4.4.3. COHESIVE ZONE MODEL FOR COH3D8 ELEMENTS

A traction-separation constitutive response is used to model the cohesive zone between the skin and stiffener. It assumes an initial linear-elastic response, followed by linear softening once damage onset is reached. In fig. 4.11 an example eight node three dimensional cohesive brick element is shown in both original and deformed state.

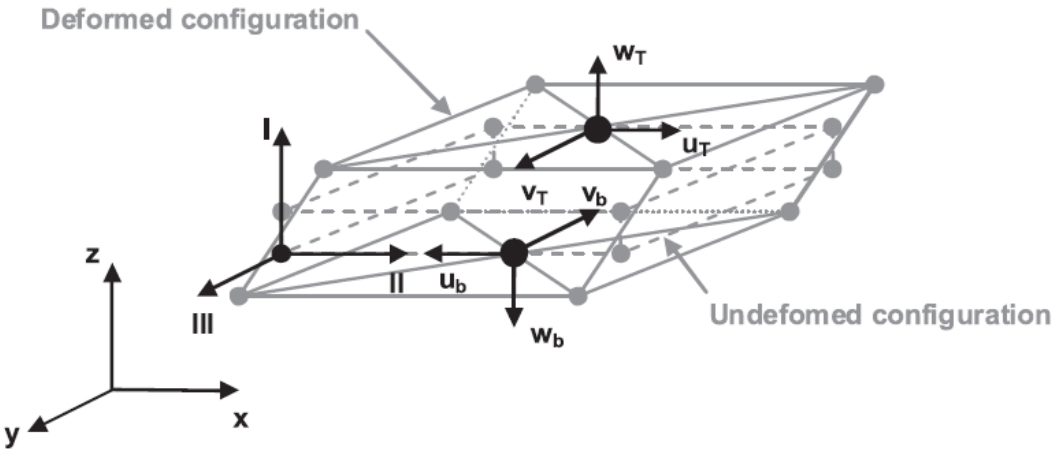

Figure 4.11: Three-dimensional eight node cohesive element. Source: [8]

Damage initiation is determine through a quadratic nominal stress initiation criterion as defined by eq. (4.16). Where the Macaulay bracket (see eq. (4.15) is used for the mode 1 damage initiation. The subscripts refer to

the element directions as shown in fig. 4.11.

$$(\frac{\langle t_1 \rangle}{t_1^0})^2 + (\frac{t_2}{t_2^0})^2 + (\frac{t_3}{t_3^0})^2 = 1 \tag{4.16}$$

Damage evolution is represented by a single scalar damage variable, which represents all damage mechanisms. The result of damage evolution in material stress, per damage mode, is presented in eqs. (4.17) and (4.18). Compressive stress in the 1 (normal) direction will not result in additional damage. Note that shear damage in the 3 direction is given by an equation equivalent to eq. (4.18).

$$t_1 = \begin{cases} (1-D)\bar{t}_1 & if \quad \bar{t}_1 \geq 0 \\ \bar{t}_1 & if \quad \bar{t}_1 < 0 \end{cases} \tag{4.17}$$

$$t_2 = (1-D)\bar{t}_2 \tag{4.18}$$

The B-K criterion is used as an energy-based mixed mode damage evolution criterion. Fracture energies in the three principal directions are input. Abaqus computes the required linear softening behaviour such that the area under the traction-separation curve is equal to the input fracture energy. In fig. 4.12, the damage initiation and evolution response is illustrated for mixed mode behaviour. Where the quadratic stress criterion dictates damage initiation and the B-K criterion dictates the damage evolution.

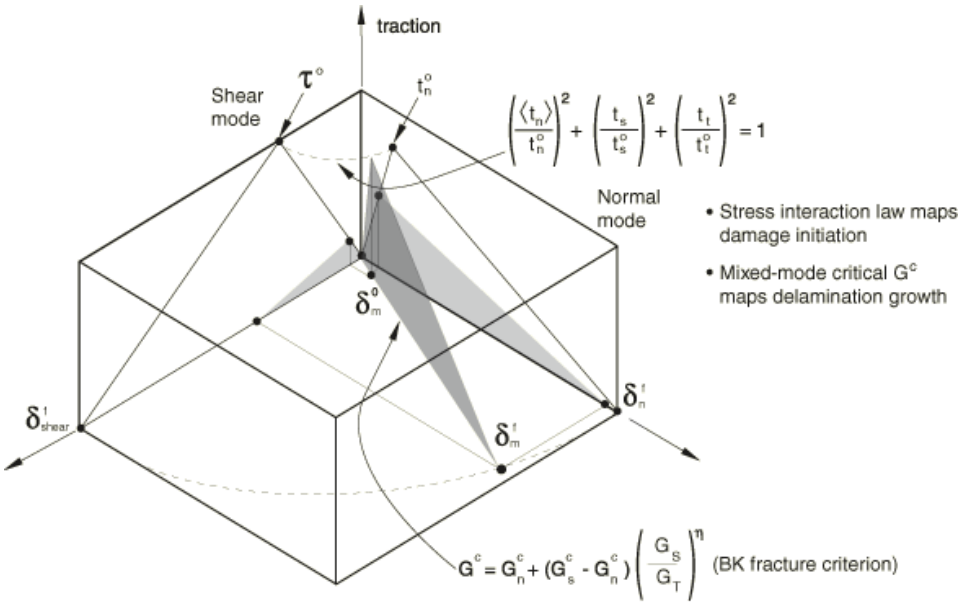

Figure 4.12: Mixed-mode response of Abaqus cohesive elements. Source: [5]

4.4.4. ELEMENT VERIFICATION

Element verification is performed on the Abaqus 'COH3D8' cohesive and 'S4R' shell elements to control the strength and damage material inputs. A 1x1x1mm control volume is used for the cohesive elements and a 1x1mm shell is used for the composite elements. The cohesive unit element is loaded under three separate load cases: normal tensile and mode 13 and mode 23 shear, where the 3 direction is in the element normal direction. The shell element is loaded in separate cases in: tension and compression in the two in-plane directions and finally in in-plane shear.

Verification of strength is performed by determining the maximum stress before damage onset. By integrating the stress-displacement curve, the fracture energy is obtained. For a fully damaged element this should be equal to the input fracture energy. In all tested cases the elements performed according to their

respective inputs.

4.4.5. RESULTS

The Abaqus model with damage definitions for initiation and evolution in both the cohesive and composite sections is subjected to a ramped displacement (up to 3mm). The same boundary conditions as in section 4.1.1 are applied. The model shows an overall linear response on the load displacement curve (as illustrated in fig. 5.5) until final failure occurs in the stiffener. This is discussed further in section 5.4.

5

QUASI-STATIC COMPRESSION TEST AND STATIC MODEL VALIDATION

An initial quasi-static test was performed on a single panel to validate the global stiffness of the models described in chapter 4, in addition to validating the buckling loads estimated by the eigenvalue analysis and non-linear analyses. Prior to testing, the panels were pre-cracked in a 7-point bending rig (as presented in [51]) to ensure that the skin was free from the stiffener in the disbonded region and to initiate the crack fronts next to the Teflon tape inserts. After pre-cracking, the panels are subject to an ultrasonic scan to monitor the crack front and delamination size.

In this chapter the experimental test set-up is introduced (section 5.1), which is identical to the set-up used for residual strength testing in chapter 9. In section 5.2 the static test results are presented, which are then used to validate the models in sections 5.3 and 5.4.

5.1. TEST SET-UP

All quasi-static compression tests are performed in a 1000kN Baldwin load frame shown in fig. 5.2. A custom rig is used to ensure the boundary conditions proposed in section 4.1.1 are also applied to the physical panels during testing. The panel ends are not potted, instead the clamped boundary conditions are ensured by means of steel frames which surround the two ends of the panel (shown in fig. 5.1. In the case of gaps between the fixed steel frame and the panel, shims are introduced to mitigate motion of the panel within the frame. The sides of the panel are constrained by two steel plates (skin buckling support in fig. 5.1), to hinder out-of-plane displacement of the skin (see fig. 4.1).

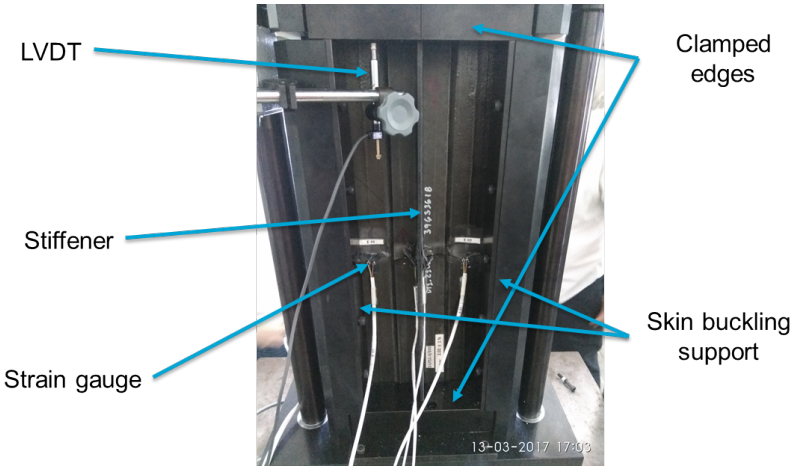

Figure 5.1: Test rig

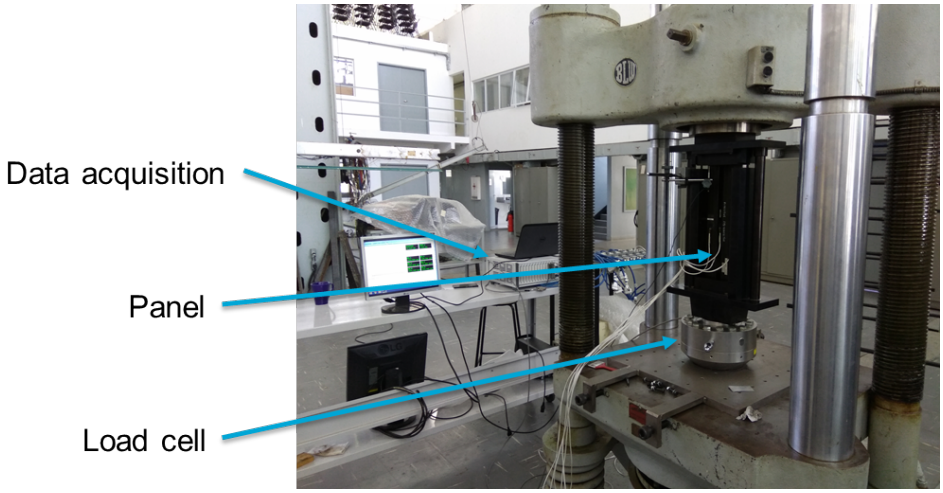

Figure 5.2: Baldwin servo-hydraulic load frame

Three pairs of quarter bridge strain gauges are placed back-to-back on the panel. Two pairs are placed on the skin, either side of the stiffener (see fig. 5.3). These pairs are meant to capture the buckling of the skin. One pair is placed on the stiffener web to monitor the stiffener load shortening. The global load-shortening is monitored by means of a load cell and a LVDT placed on the rig frame (see fig. 5.1). All the test data is collected by an HBM data acquisition system, which is stored and visualized on a desktop computer (see fig. 5.2).

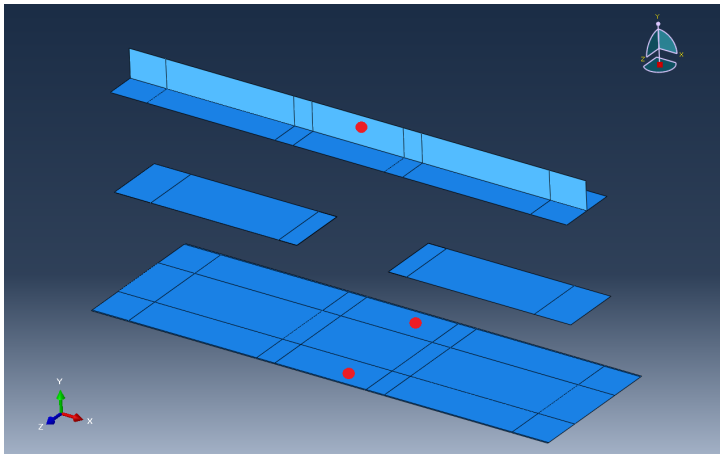

Figure 5.3: Placement of back-to-back strain gauges marked in red

5.2. QUASI-STATIC TEST DATA

The panel was subjected to a displacement controlled compression in the Baldwin load frame. At a load of -20kN the skin showed a clear buckle, away from the stiffener. A diagonal buckling half-wave was observed, which is further confirmed by the DIC image analysis presented in fig. 5.4. Some short, sharp cracking sounds were observed throughout the test, as the panel was subjected to a higher compression load. At approximately -115kN, a significantly louder crack was heard, followed by a small jump in displacement and a small drop in load on the global load-shortening curve (fig. 5.5). Shortly after, at a load of -120kN the panel suffered catastrophic failure.

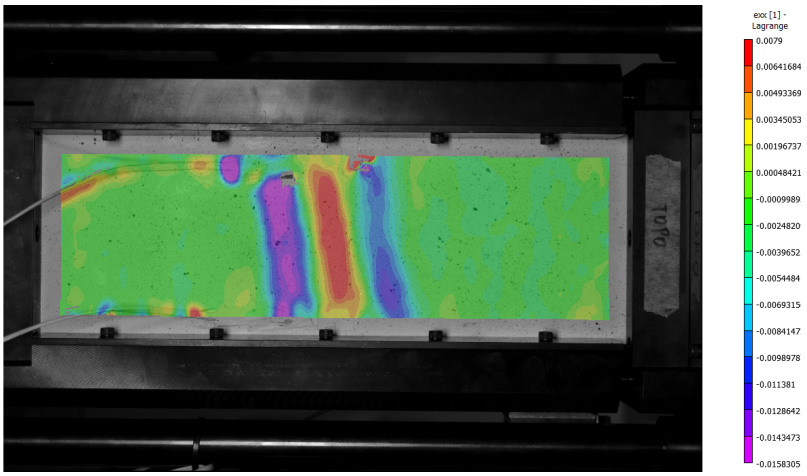

Figure 5.4: DIC analysis of panel skin 401_01, load=80kN

The stiffener did not show any buckling or crippling failure. Using the strain reversal method, the buckling load was determined for the two pairs of strain gauges on the skin. Other methods were investigated, such as the top-of-the-knee and using the load shortening curve, however the strain reversal technique was deemed most robust. The strain reversal method uses the point at which the strain changes direction, ie. the stationary points highlighted in figs. 5.6 and 5.7 by circles. It is reported in literature though that this method often under-predicts the buckling load [52]. Since the buckling pattern on the skin is diagonal, different buckling loads were found for the two different sets of strain gauges. Strain gauge 2 showed a buckling load of -14.69kN, whilst strain gauge 4 showed a buckling load of -17.20kN (see fig. 5.3 for strain gauge locations.

5.3. VALIDATION OF EIGENVALUE AND STATIC GENERAL MODELS

The linear buckling analysis performed in section 4.2.2, estimated a buckling load of -19kN for a panel with a 110mm initial disbond. This disbond was measured before the experiment using a c-scan device. The two experimental buckling loads from the skin are: -14.69kN and -17.20kN for strain gauges 2 and 4, respectively. These two experimental buckling loads are 22.7% and 9.5% from the linear buckling load, respectively. This shows good agreement between the linear buckling model and the experimental data. Sources of error include the estimation of the initial disbond size and the shape of the initial disbond front, which is not necessarily straight. As shown, the location of the strain gauge influences the measured buckling load which, combined with the strain-reversal technique, may account for the discrepancy.

The non-linear analysis performed with the Abaqus standard solver offers more insight into the behaviour of the panel when compared to the linear buckling analysis (eigenvalue analysis). We can accurately extract the data from the Abaqus/static general model at the exact position of the strain gauges in the experimental panel. Using the same method of strain-reversal, buckling loads of -13.02kN and -17.23kN are obtained for strain gauges 2 and 4, respectively. Which in turn gives an error with respect to the experimental data of 12.8% and 0.2% for strain gauges 2 and 4, respectively. This shows a very good correlation between the test data and the non-linear Abaqus/static general model.

5.4. VALIDATION OF ABAQUS/EXPLICIT MODEL

First, we look at the global response of the experimental test compared to the numerical models. The load-shortening of both the static general and the explicit model is compared to the experimentally obtained data in fig. 5.5. A very good agreement is found in the global stiffness response of both models up until approx. 50kN. Thereafter, the test data shows a more relaxed stiffness compared to the numerical models. The clear difference between the Abaqus static general and the Abaqus Explicit model is the ultimate failure, which is only captured by the Explicit model. The Explicit model shows an ultimate strength of -131.6kN, this is 7.8% higher than the ultimate load found experimentally (-122.1kN). The displacement at failure is 7.6% lower in the numerical model, compared to the test data. In summary, a good agreement is found, considering the global response and ultimate load of the panel. A kink is evident in the test data, occurring at around 2.5mm displacement, a sharp cracking noise was observed at this point in the test. This could be caused by a jump in delamination growth, which could explain the larger displacement in the test data, compared to the model data.

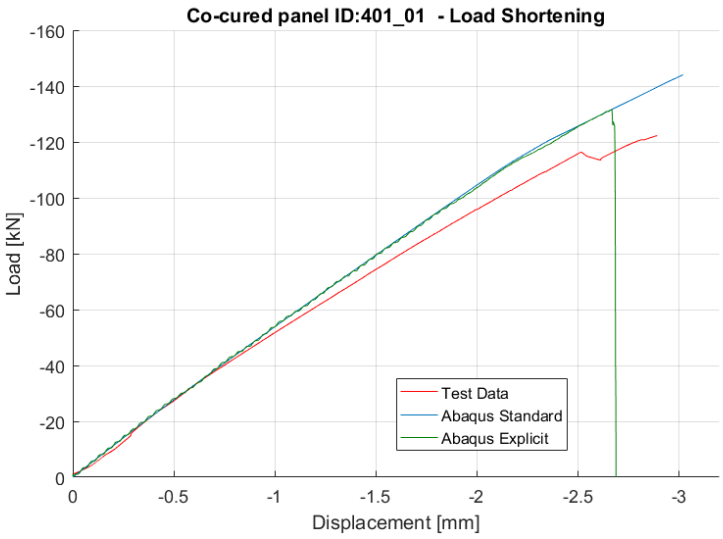

Figure 5.5: Load shortening of panel 401_01 - comparison with Abaqus static general and explicit models

Next, we consider the buckling of the skin. Strain gauge data from the test is compared to strain output

from the explicit model. As mentioned previously the strain gauges on the skin are numbered 2 and 4, as shown in fig. 5.3. The strain output from the Explicit model is taken from the same position as the strain gauges in the test. In fig. 5.6 the strain comparison is shown. The results for strain gauge 2 match well, with the numerical model showing a 13.3% lower buckling load. Strain gauge 4 however shows a 143.6% higher buckling load in the numerical model, compared to the test data. A study has been performed into the elements surrounding the one from which the strain was obtained. In fig. 5.7, the strain from a neighbouring element is shown (in green), showing a much better agreement with the experimentally obtained buckling load. This new data is thus not obtained from the exact same location as the strain gauge on the physical panel, it is obtained from an element 8mm further away from the edge of the panel.

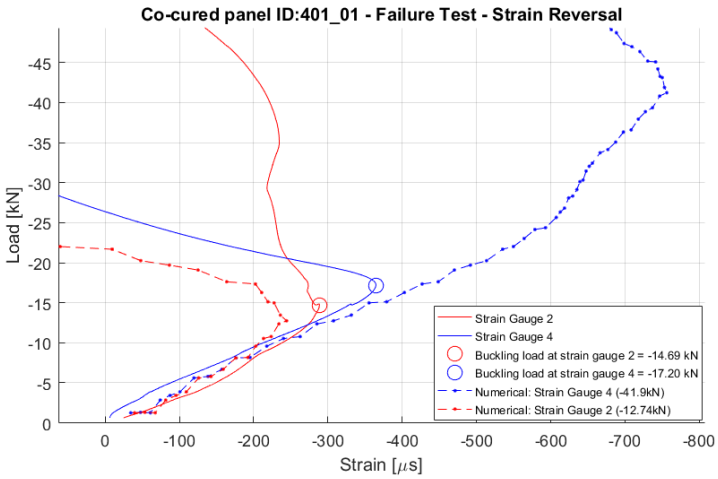

Figure 5.6: Validation of buckling load in numerical model

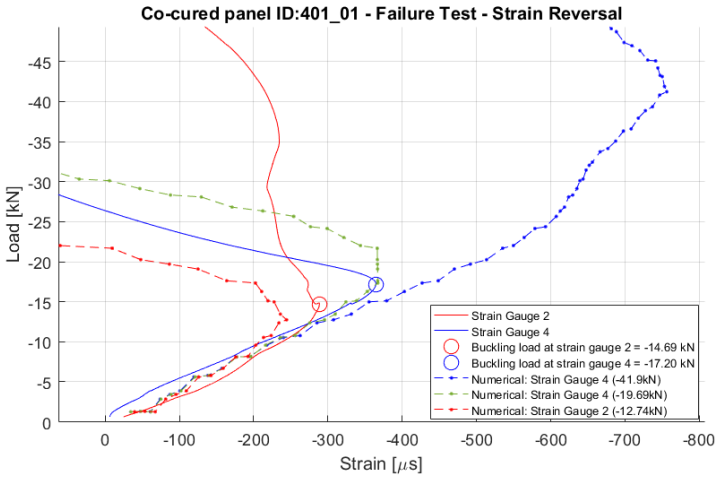

Figure 5.7: Corrected strain output from numerical model

PHASE II - FATIGUE

6

FATIGUE LOAD ESTIMATION AND CALIBRATION

Before the fatigue testing of the co-cured panels, one sacrificial panel was used to test and calibrate the experimental setup. This involved determining the testing load, testing the in-situ NDT method and checking the instrumentation and control of the load frame. In section 6.2 the experimental setup and NDT method is presented. The fatigue load is analytically estimated in section 6.1 based on high level requirements.

6.1. DETERMINING FATIGUE LOAD

This section serves as a preparation for the experimental tests in chapter 8 and serve as input for the model described in chapter 7. The fatigue loading parameters are estimated to fulfill the requirements and limitations listed below. Requirements 1-3 are high level requirements, whilst requirement 4 is dictated by the load frame used for fatigue testing. Requirement 3 is two times the number of load cycles a typical commercial aircraft endures throughout its life. All loads described are compressive, unless stated otherwise.

- **Req 1:** R-ratio = 10 [†]
- **Req 2:** Final disbond length = 140mm (initial disbond length =100mm)
- **Req 3:** Target number of cycles, N = 120'000 cycles
- **Req 4:** Maximum cyclic load, P_{max} = -50kN

Since the R-ratio is fixed, only the maximum load, P_{max}, is required to fully describe the fatigue load cycle. The loading frequency is discussed later in section 6.3. To determine the maximum load a LEFM based method is employed.

The dimensional notation is introduced in fig. 6.1. Where the initial disbond length, a_0, grows in steps of Δa to the target disbond size, a_f. Since the disbond grows at two crack fronts, the crack growth per increment per side is: $\frac{\Delta a}{2}$. Equation (6.1) shows the incremental growth of the disbond. The disbond width, w, is constant (defined by the area of the stiffener flanges).

$$a_{n+1} = a_n + 2 \cdot \frac{\Delta a}{2} \tag{6.1}$$

A rudimentary LEFM method is combined with a Paris relation to determine the amount of cycles, N, required to grow the crack in discrete steps of 5mm (Δa) from an initial disbond length (a_0) of 100mm to a final disbond length (a_f) of 140mm. The purely linear elastic model (with varying disbond length) introduced

[†]Since a compression-compression fatigue load cycle is applied we define the R-ratio as 10, most sources however use in this case the notation for tension-tension loading ie. giving a R-ratio of 0.1

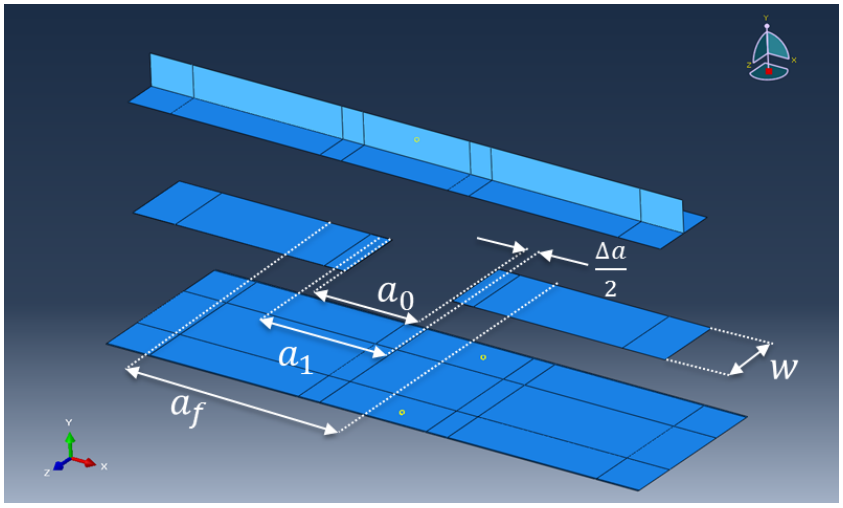

Figure 6.1: Notation used for fatigue crack growth estimation

in section 4.3 is used to output the total strain energy, U, over a load ranging from 0kN to -50kN. The strain energy release rate may be computed using eq. (6.2) using eq. (6.3) as the change in area.

$$G = -\frac{\delta U}{\delta A} \tag{6.2}$$

$$\Delta A = \Delta a \cdot w = (5 \cdot 64 = 320 mm^2) \tag{6.3}$$

It was found that the G values at P_{min} loads, were 4 orders of magnitude smaller than the obtained G value at the corresponding P_{max}). A Paris equation eq. (6.4) is used to determine the crack growth rate over a range of loads [0,-50kN] with a R-ratio of 10. Since G_{min} is negligible compared to G_{max}, it is assumed that $\Delta G = G_{max}$.

$$\frac{dA}{dN} = c(\frac{\Delta G}{G_c})^m \tag{6.4}$$

with

$$\Delta G = G_{max} - G_{min} \approx G_{max} \tag{6.5}$$

The Paris coefficients are corrected for mode-mixity using the Blanco equations presented in section 2.3.2. Furthermore, the critical strain energy release rate value, G_c is corrected for mode-mixity using the B-K equation, also presented in section 2.3.2.

Equation (6.4) can then be integrated to give the number of cycles required to grow the crack by the predetermined length increment. The inherent assumptions are that the crack front will grow straight towards the loaded edges and that there are no other energy losses in the system. Furthermore, mode-mixity is taken into account, however it is assumed to be constant along the crack front. This is therefore a coarse, low fidelity method for determining the number of fatigue cycles required to grow the disbond given a certain maximum load level, P_{max}. By using **req 1** and **req 3**, a P_{max} is obtained.

Since the mode-mixity (ϕ) was not known, a large range of mode mixities was analyzed. The results are shown in fig. 6.2. Based on the analyses and testing performed in chapters 4 and 5, the mixed mode ratio was expected to be in the low range, close to pure mode I. This is because the skin buckles away from the stiffener leading to an expected mode I opening along the crack front. A load of $P_{max} = -32kN$ was selected, which gives a $P_{min} = -3.2kN$.

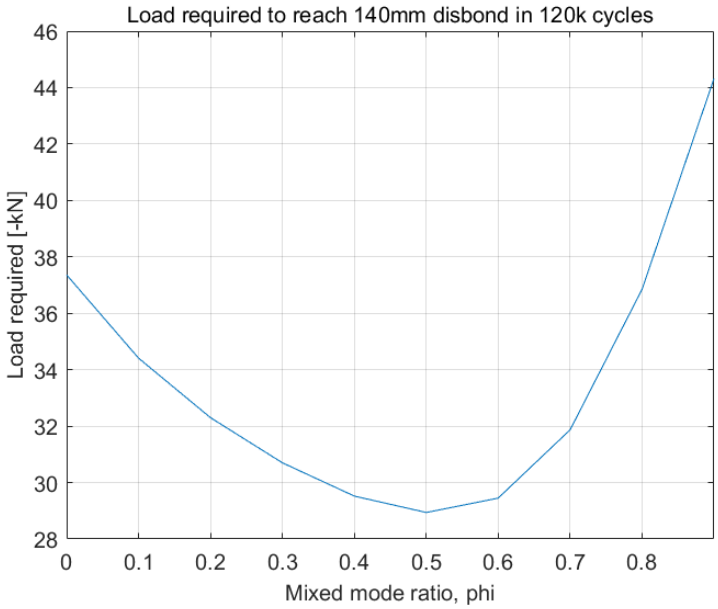

Figure 6.2: Predicted maximum fatigue load P_{max} required to grow disbond from 100mm to 140mm

6.2. TEST SET-UP AND NDT METHOD

A 50kN servo-hydraulic load frame (Spectra model AH-310-50-150) was used for high cycle fatigue testing. The test was load controlled, with a -50kN load cell providing feedback to the computer control system. The same panel rig that was used for the static test in chapter 5, was used for fatigue testing. An overview of the fatigue test set-up is shown in fig. 6.3. Shims were applied between the panel and the test rig clamps to avoid motion of the rig within the clamped section. As described earlier, potting and machining each panel was not feasible, thus shims were used to ensure proper contact between the test rig and the panels.

An ISONIC 2006 c-scan system [53] with a handheld transducer was used to scan the panels throughout the fatigue testing. The same system was used prior to fatigue testing to determine the initial disbond area. The c-scan system uses a sonic triangulation method to determine the position of the handheld ultrasonic transducer. The antennas used for triangulation were calibrated prior to use. A jig was prototyped for the antennas to ensure constant width between them (see fig. 6.4). In order to reduce repeatability errors, all c-scans were performed by the author.

Initially, the panels were scanned without being removed from the test rig. This was made possible through the application of a blister filled with ultrasonic gel couplant, attached to the skin side as shown in fig. 6.4. However, inconsistent results were obtained using this set-up, partly due to the unergonomic grip on the transducer and cramped working space within the rig. It was decided to remove the panel from the test rig for each inspection. This required the removal of 18 bolts, increasing slightly the inspection time, however the c-scan results improved noticeably. The removal and re-installation of the panel at each inspection interval does introduce a source of variability in the test setup, however it was deemed to be the most reasonable method of inspection available.

According to the manufacturer manual [53] of the ultrasonic scanning equipment a resolution of less than 1mm is achievable. While that claim may be true for the transducer by itself, when combined with the positioning method of sonic triangulation, a error of $\approx \pm 1.5mm$ was observed for single point measurement ie. if a delamination is detected its position accuracy is $\pm 1.5mm$. When measuring the distance between two crack fronts this error is present on both crack fronts, therefore the error in measuring disbond length is $\pm 3mm$. The machine was properly calibrated and cleaned, according to manufacturer guidelines prior to use.

The rig for the c-scan antennas was still used to maintain spacing between the antennas. Additionally, the gel bag on the skin was kept in place, reducing the usage of ultrasonic couplant. The gel bag had a secondary

Figure 6.3: Fatigue test setup. Left to right: Load frame with test rig, portable c-scan device, hydraulic control computer.

effect of cooling the panel in the buckling area, mitigating possible hysteresis heating. This was confirmed using an IR-camera; no significant heating was observed on the panel during fatigue testing.

6.3. TEST CALIBRATION

A sacrificial panel (ID: 401_02) was used to test the experimental setup for fatigue testing in addition to validating the load level determined in section 6.1. The control system for the servo hydraulic actuator was tuned to apply a cyclic load with a sinusoidal wave form. The maximum and minimum compressive loads were -32kN and -3.2kN, respectively. On the hydraulic control computer the load readout had a maximum variation of $\pm 0.2kN$ at P_{max} which equates to ±0.6%. A 5Hz loading frequency was selected based on hydraulic pump limitations and oscillation of the load frame. At this frequency no heating was detected by IR inspection of the panel.

After approximately 100'000 cycles, with intermittent inspections, a disbond growth of $\approx 7mm$ was recorded, far less than the 40mm target in section 6.1. The disbond grew from approx. 102mm to 109mm. The test was interrupted frequently and abruptly due to jamming of the test rig. The two guiding rods on either side of the panel clamps showed signs of fretting (see fig. 6.5). Given that the bearing surfaces were both steel (with poor surface finish) the machine would often seize with the rig in an asymmetric position. Furthermore, large oscillations were observed in the load frame. When a shutdown occurred the hydraulic cylinder slowly lost pressure causing the guiding rods of the rig to slip out of their bushings in the top clamp. This would lead to time consuming re-positioning of the rig.

Two design changes were made to the test rig: firstly the steel bushings in the top of the rig were replaced with linear bearings. This improved the sliding motion of the guiding rods and prevented the rig from seizing during fatigue loading. Secondly, two steel rods were turned which could be threaded into the top of the guiding rods. This prevented the rig from going out of alignment in the case of hydraulic pressure loss. The design changes are illustrated by before and after photos of the test rig in fig. 6.5. Both design changes significantly improved the functionality, reliability and safety of the test setup.

Following the rig modifications it was decided to increase the maximum load from -32kN to -40kN in order to observe a larger disbond growth. This cyclic load, with the same R-ratio of 10, was applied for a total of 272'000 cycles on the same sacrificial panel (ID 401_02). Growth was observed during the first 5000 cycles,

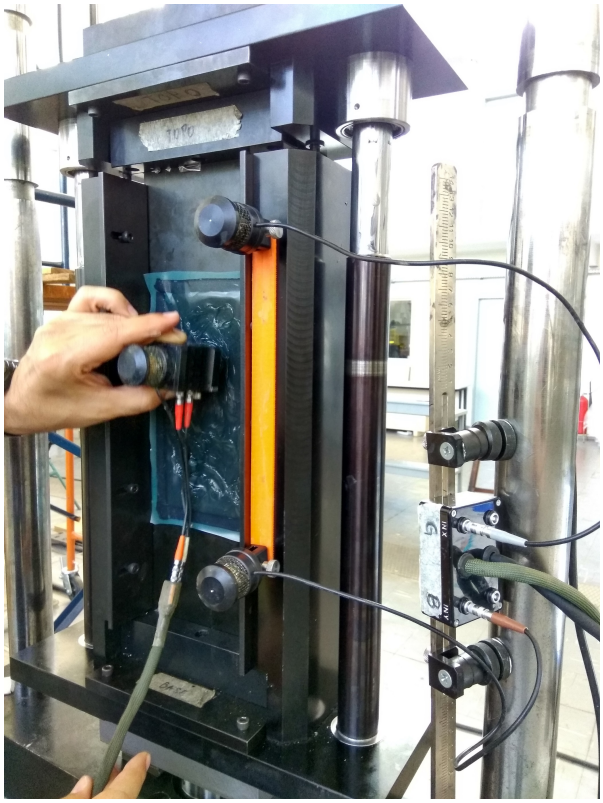

Figure 6.4: Initial in-situ c-scan setup with gel bag attached to skin. Antenna mounting prototype in orange.

thereafter it stagnated for the remaining 267'000 cycles. This is shown graphically in fig. 6.6, a jump in disbond length is seen when the maximum cyclic load was increased to -40kN. Error bars of $\pm 3mm$ are included to account for measurement error of $\pm 1.5mm$ on both the crack fronts. Since the disbond showed no sign of further growth after a cumulative 370'000 cycles it was decided to increase the P_{max} to -47kN. After 80'000 cycles at -47kN no further growth was observed, giving a final disbond length of approximately 115mm after close to 450'000 cycles at the previously mentioned loads. A P_{max} of -47kN and P_{min} of -4.7kN pushed the fatigue load frame close to its theoretical limit of -50kN. In order not to trip the machine, a -47kN was set as the maximum feasible fatigue testing load.

At the load of -47kN with a R-ratio of 10, measurable but limited disbond growth was observed. Since this was the maximum load for the Spectra load frame, it was decided to perform all future fatigue tests under these conditions to maximize the possible measurable disbond growth. The observations made and their contrast to the predicted growth may be due to the following reasons:

- A straight crack front was assumed, the c-scans and later fatigue models showed that this was not the case. The corners of the crack front grow rapidly initially, rounding the crack front, followed by slow, stable growth of the entire crack front. A side-by-side comparison of the crack front progression is given in fig. 6.7. Note: this image demonstrates the general crack propagation behaviour observed in all panels subject to fatigue, the image is not of the sacrificial panel (ID: 401_02) due to inconsistent c-scan images obtained during test setup and calibration.

- Material data: the Paris data is from external sources, obtained for another material (discussed at length in section 7.4)
- Results from an early Abaqus model indicated that the mode mixity was much higher than anticipated, closer to mode II than to mode I. This will be discussed in (chapters 7 and 8).

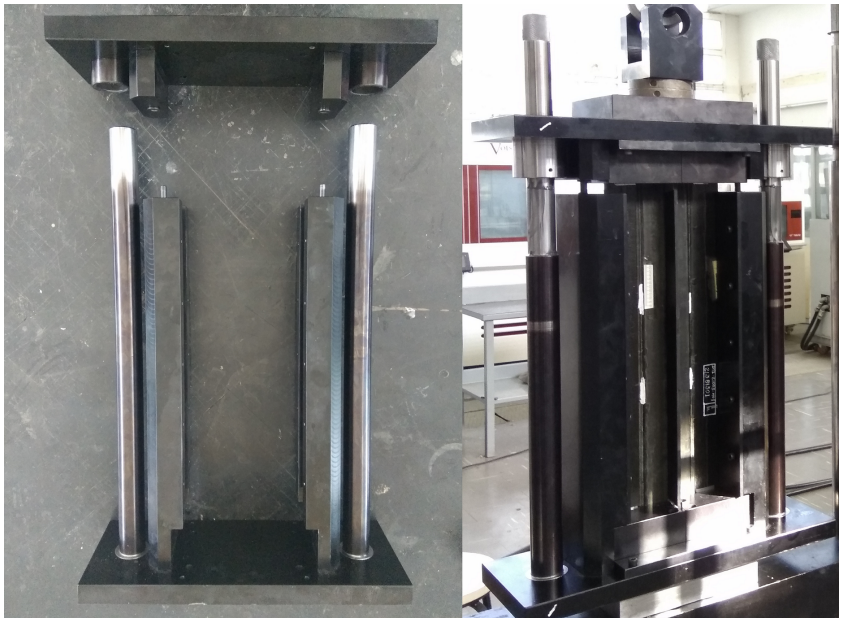

Figure 6.5: Left: initial test rig with signs of wear on the guiding rods. Right: modified test rig with knurled guide rod extensions and linear bearings installed.

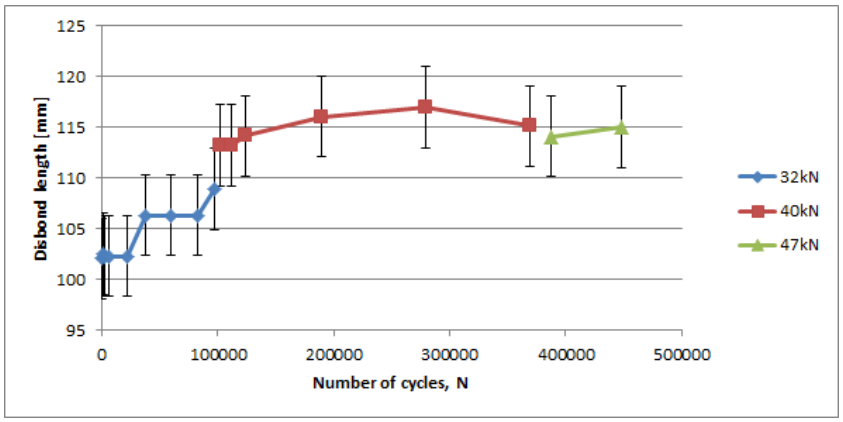

Figure 6.6: Disbond growth on panel 401_02 during fatigue calibration tests. 3 different maximum load levels were tested increasing from -32kN to -47kN.

6.4. SUMMARY OF FATIGUE TEST CALIBRATION

Initial fatigue testing of a sacrificial panel was performed to verify the test setup, loading conditions and NDT method.

- **Test rig:** Based on initial fatigue tests two design changes were made to the test rig to improve functionality, reliability and safety.
- **NDT:** A fixture was prototyped to improve the repeatability of the non-destructive inspections. A portable c-scan machine is used for NDT, which after calibration showed a $\pm 1.5mm$ error for a single point measurement.
- **Fatigue loading:** A maximum fatigue load of -47kN is selected to achieve the largest possible disbond growth, given the load frame operating limits. At an R-ratio of 10, this equates to a minimum compressive load of -4.7kN. A 5Hz testing frequency is selected. The number of cycles are limited by the available time for testing, leading to limit of 350'000 cycles per panel (an additional 4 panels are to be tested under fatigue loading).

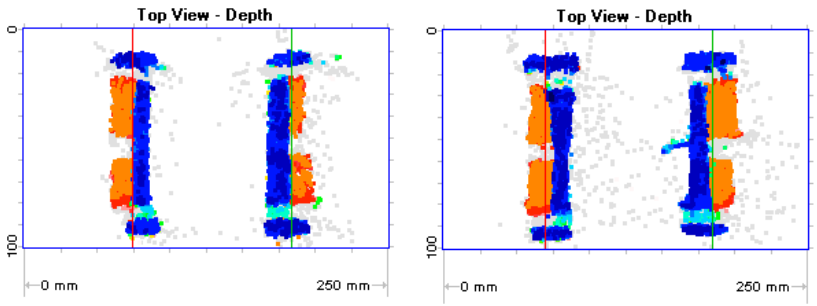

Figure 6.7: Crack growth in panel 401_05 measured by ultrasonic scanning. Left at N=1, right at N=205'000. Orange/red colour indicates bonded region, blue/light blue indicates disbonded region. White indicates un-scanned region.

7

ABAQUS FATIGUE MODEL

A cohesive zone model based on the work by Kawashita, Harper and Hallett [45, 46] is implemented in Abaqus as a user defined material (VUMAT). The VUMAT sub-routine was originally coded by Lucas Oliveira (phd candidate at ITA) and implemented in coupon level models (DCB, 4ENF and MMB). This code was adapted to work with the stiffened panel model presented in chapter 4 with a time explicit integration scheme. The fundamentals of this class of models are presented in section 2.3.3. The static model previously implemented in Abaqus/Explicit (see section 4.4) is modified to use the VUMAT sub-routine, these changes are discussed in section 7.1. In section 7.2 some additional details regarding the VUMAT sub-routine are presented. Finally, the results of the fatigue analysis are presented in section 7.4. These will then be validated using experimental data in chapter 8.

7.1. MODEL REVISION

The greatest challenge was to run the fatigue model in a time effective manner with the allocated computational resources. For reference, initial tests when implementing the VUMAT sub-routine showed that to run around 100'000 fatigue cycles would take in the order of weeks. This is clearly not an acceptable time window for a component of this size and complexity. A goal of 24 hours was set (using 16 cores on the TU Delft hpc12 cluster), to run the entire fatigue model up to 350'000 fatigue cycles.

To achieve this goal, a number of things were changed in the model. Firstly, the number of elements was reduced by introducing transition regions, allowing a fine mesh near the crack front an a coarse mesh further away from the interest region. Secondly, the VUMAT was only applied in a small region of cohesive elements where the fatigue crack was expected to grow. A section of linear elastic cohesive elements was used to transition between the VUMAT elements and a tie-constraint between the stiffener and skin. In fig. 7.1 an updated exploded view of the model is presented.

The current mesh has ≈55000 elements and is able to run in under 2 hours on the TU Delft cluster using 16 cores. With further changes to the load ramping method in the cycle jump formulation described in section 2.3.3 further gains in computation time may be achieved. A comparison was made with the quasi static explicit model presented in chapter 4, which was deemed to have converged. The global load-shortening curve showed less than 1% difference in failure load and stiffness between the revised model and the initial model. Furthermore, no significant stress concentrations were observed in the transition regions between the VUMAT elements and the linear elastic elements.

7.1.1. INITIAL DELAMINATION SIZE

Two models are proposed, one with an initial delamination length of 105mm and one with an initial delamination length of 110mm, corresponding to initial disbond areas of 6300mm^2 and 6600mm^2, respectively. This is based on c-scans of the panels, after pre-cracking of the interface in front of the Teflon tape insert. Prior to precracking, the panels had delamination sizes determined by the Teflon insert (100mm long). Pre-cracking

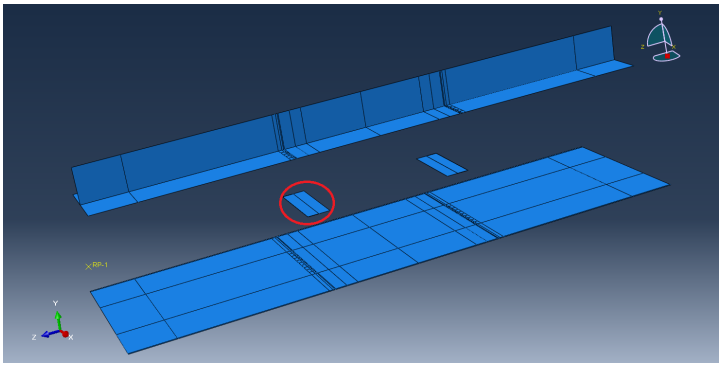

Figure 7.1: Updated Abaqus model used for high cycle fatigue analysis of the co-cured interface, one of the cohesive sections is circled

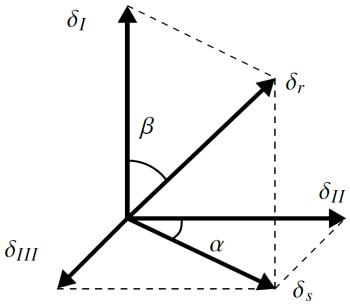

Figure 7.2: Resultant displacement vector. Source: [6]

the panels increased the initial disbond length with 5-10mm. Modelling a straight delamination front, as is done in the current Abaqus model, is an approximation of the actual delamination front in the test panels. The c-scans did show a reasonably straight crack front after the pre-cracking procedure.

7.2. VUMAT DESCRIPTION

The VUMAT used in this thesis was developed by L. Oliveira (PhD candidate at ITA) as part of his doctoral research. It is based on the work by Kawashita, Harper, Hallett, May and Nixon-Pearson of the University of Bristol [33, 45–47, 54], which is discussed in section 2.3.3. The basis for the subroutine formulation is the work by Harper and Hallett [46, 47]. It does not use the global crack front tracking algorithm proposed by Kawashita et al. [45], however it does incorporate changes to the element local formulation proposed by May et al. [54] and Kawashita et al. [45]. An outline of the fatigue damage formulation in the VUMAT subroutine is presented below. The static portion of the sub-routine is not included in detail here as it has been covered extensively by Jiang et al. [55].

Static Damage Formulation The resultant displacements, in mode I, II and III are combined to form a single displacement vector and shear vector as given by eqs. (7.1) and (7.2), shown visually in fig. 7.2. A quadratic damage initiation criterion is used (eq. (7.3) for static damage initiation.

$$\delta_r = \sqrt{\delta_I^2 + \delta_{II}^2 + \delta_{III}^2} \tag{7.1}$$

$$\delta_s = \sqrt{\delta_{II}^2 + \delta_{III}^2} \tag{7.2}$$

$$DI := \frac{\langle \sigma_I \rangle^2}{S33} + \frac{\sigma_{II}^2}{S13} + \frac{\sigma_{III}^2}{S23} \geq 1 \tag{7.3}$$

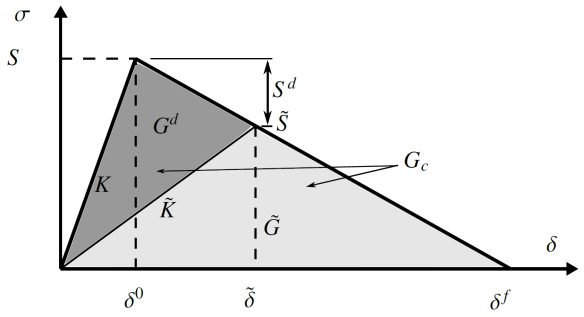

Figure 7.3: Generic bi-linear softening relation

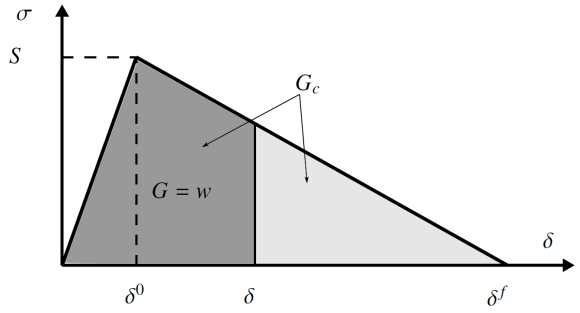

Figure 7.4: Calculation of strain energy release rate using traction separation curve

For a given mode-mix ratio, ϕ, an equivalent bi-linear traction separation law is determined (shown in fig. 7.3 for a general case). This is done whilst ensuring that the total area under the traction separation curve is equal to the critical fracture toughness for that given mode-mix. A B-K relation (eq. (2.11)) is used for the mode-mix interpolation of the critical fracture toughness.

The static damage in terms of strength, D_S, is given by eq. (7.4). Where the tilde indicates the current state and the superscript d is the damaged strength (see fig. 7.3). In [6] it is shown that this damage parameter, D_S, is equivalent to the area damage, D_A, and fracture toughness damage, D_G.

$$D_S := 1 - \frac{\tilde{S}}{S} = \frac{S^d}{S} = \frac{\delta_f - \delta_0}{\delta_f - \tilde{\delta}} \tag{7.4}$$

Fatigue Damage Formulation As described in section 2.3.3, a cycle jump method is used for analysing high-cycle fatigue damage. Once the maximum load has been reached and the system is in steady state, the fatigue damage law is activated.

The strain energy release rates for the three different modes are super-positioned to give an equivalent strain energy release rate. The individual strain energy release rates are calculated by integrating the area under the traction separation curve, as shown in fig. 7.4. Since this is done at the load of P_{max}, we get the maximum strain energy release rate for a fatigue cycle.

A threshold criterion is used to determine when fatigue damage starts to degrade an element. Threshold values for the strain energy release rate are experimentally obtained for mode I, II and mixed mode conditions. These are interpolated for the mixed mode ratio, ϕ, using a B-K relation as shown in eq. (7.5). Note, this B-K constant, η_{th} is not the same as the B-K constant used for the interpolation for the critical strain energy release rate. The mixed-mode dependency of the threshold fracture toughness is contested by O'Brien et al. [56] who determined for different reinforced thermoset and thermoplastics that no such relation existed. However, since the $G_{threshold}$ values obtained experimentally by Asp et al. are for the same material as the Paris relation data, its use is deemed appropriate.

$$G_{th} = G_{I,th} + (G_{II,th} - G_{I,th}) \cdot \phi^{\eta_{th}} \tag{7.5}$$

Using eq. (7.6), the ΔG is obtained for one fatigue cycle, which is used as an input for the determination of the crack growth rate for a single cycle. In cases where significant geometric non-linearities occur one must use the element local R-ratio, rather than the globally applied R-ratio. This introduces a whole new set of problems, which will be discussed at a later stage.

$$\Delta G = G_{max,eq} \cdot (1 - R^2) \tag{7.6}$$

The crack growth rate per cycle is determined using a Paris relation, described by eq. (7.7). A Blanco type interpolation is used to account for mode-mix in the Paris coefficients, C and m (see 2.3.2). Note, that eq. (7.7) describes a 1D crack growth rate, obtained experimentally by observing a 2D crack front propagating through a coupon. This is then translated back into a 2D crack growth rate (ie. area) by using a constant width element. For elements without a constant width, it is recommended to reformulate the Paris relation to area growth rather than crack length growth.

$$\frac{da}{dN} = C \cdot (\frac{\Delta G}{G_c})^m \tag{7.7}$$

The fatigue damage increment is then calculated using eq. (7.8), where ΔN is the number of fatigue cycles jumped during an increment in the explicit solver and l_e is the element length. Since the Paris equation accounts for all damage throughout a fatigue cycle, the static damage, D_S, calculated in the **static** VUMAT description is removed.

$$\Delta D_f = \Delta N \cdot \frac{da}{dN} \cdot \frac{1 - D_S}{l_e} \tag{7.8}$$

The sub-routine was verified at the element and coupon level. Comparison with coupon level experimental data (DCB, 4ENF and MMB) showed good agreement in disbond growth under fatigue loading as reported in [6] (**submitted**). The author assisted in debugging the code for use in the Abaqus explicit model described in section 7.1.

7.3. FATIGUE MODEL INPUTS

In table 7.1 all the subroutine inputs are described, including their sources. For details on the composite material inputs see table 4.2. The material data from Arbelo [49] is specific for the material used in the INOVA project. The interpolation data by Blanco et al. [38] is based on the data from Asp et al. [27] for a toughened polymer matrix reinforced with carbon fibres (HTA/6376C). It is similar in strength, stiffness and toughness to the T800/3900 material used in the INOVA project. Until coupon level fatigue testing is complete for the T800/3900 material, it is deemed reasonable to use the HTA/6376C data as a starting point.

7.4. FATIGUE MODEL RESULTS AND OBSERVATIONS

In fig. 7.5 the evolution of damage is shown as the model undergoes the linear ramping of the compressive load and subsequent fatigue damage. This image shows only the cohesive elements (marked with a red circle in 7.1). At N=1 (top image), the purely static damage as a result of the load application is shown, a small number of elements have failed from pure static loading in the top right corner. The following images show how the crack front propagates through the cohesive elements whilst fatigue damage is applied. In the top left corner we observe elements being damaged and failing due to pure fatigue damage. At a total of 350'000 cycles a distinct rounding of the initial corners is observed, similar to the damage pattern seen in coupons (DCB) subject to fatigue testing. The top right corner shows more static and fatigue damage due to the asymmetric buckling pattern observed in the skin (see section 4.3).

Table 7.1: VUMAT subroutine inputs

Property	Value	Unit	Source	Description
h	0.02	mm	User input	element thickness
R	0.1	-	User input	load ratio
l_e	0.4	mm	User input	element length
E33	2970	MPa		mode I modulus
G13	1080	MPa		shear modulus
G23	1080	MPa		shear modulus
S33	50	MPa		mode I strength
S13	180	MPa	Arbelo [49]	shear strength
S23	180	MPa	T800/3900	shear strength
$G_{I,c}$	0.1825	kJ/m^2		mode I critical SERR
$G_{II,c}$	1.16	kJ/m^2		mode II critical SERR
$G_{III,c}$	1.16	kJ/m^2		mode III critical SERR
BK_c	6.72	-		BK constant for G_c mixed mode
$G_{I,th}$	0.06	kJ/m^2		Mode I threshold SERR
$G_{II,th}$	0.1	kJ/m^2	Asp et al. [27]	Mode II threshold SERR
$G_{III,th}$	0.1	kJ/m^2	HTA/6376C	Mode III threshold SERR
BK_{th}	2.737	-		BK constant for G_th mixed mode
C_I	0.00221	-		Mode I Paris constant
m_I	5.09	-		Mode I Paris exponent
C_{II}	0.122	-	Blanco et al. [38]	Mode II Paris constant
m_{II}	4.38	-	HTA/6376C	Mode II Paris exponent
C_m	609000	-		Mixed mode Paris constant interpolation coeff
m_m	5.48	-		Mixed mode Paris exponent interpolation coeff

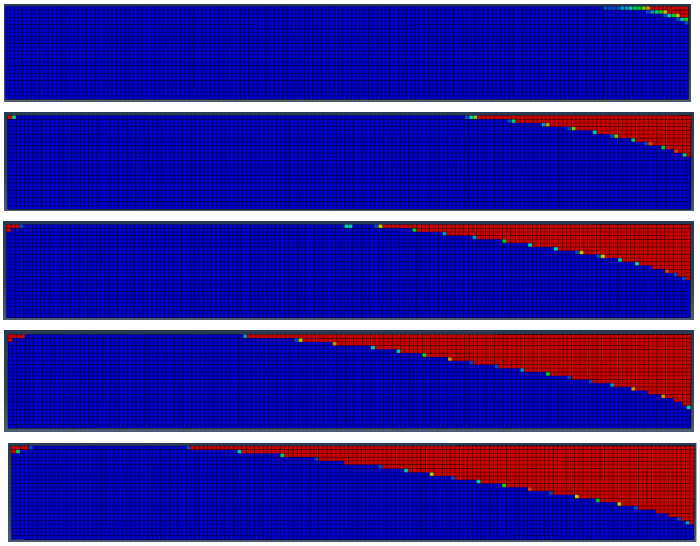

Figure 7.5: Damage evolution of cohesive elements under fatigue. Number of fatigue cycles from top to bottom: N=1, N=10'000, N=50'000, N=200'000, N=350'000

To determine the driving mechanism behind the disbond growth, the energy release rates for mode I, II and III are shown in fig. 7.6 for the entire cohesive section as a function of the analysis pseudo time. Furthermore, the increase in disbond area is plotted, also as a function of the pseudo time. The fatigue damage law is activated at t=0.21s (marked by a vertical line), after this time the model undergoes 50'000 fatigue cycles per pseudo-second. In other words, at t=7.21 the model has undergone 350'000 fatigue cycles. A very clear correlation is shown between the mode II energy release rate and the disbond area growth. In the initial ramping of the load (between t=0s and t=0.2s) there is an increase of mode I and III energy release rate, however when the loading ramp has stabilized and the fatigue law is activated only the mode II energy shows a significant

increase in magnitude.

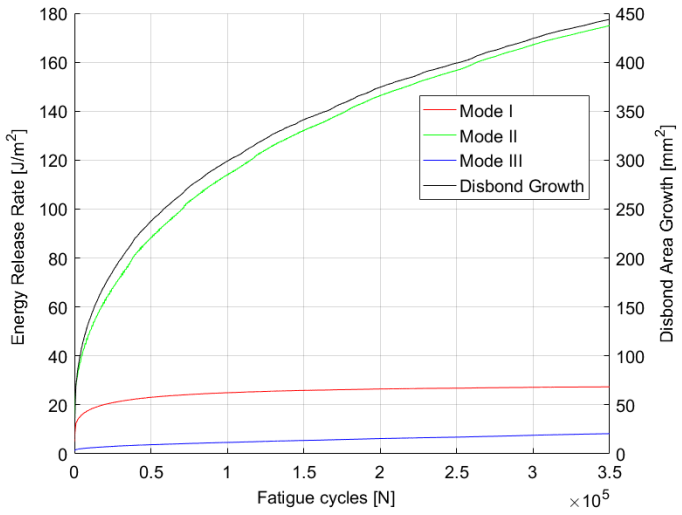

Figure 7.6: Total strain energy release rate and disbond area growth

Further checks include the monitoring of the artificial strain energy accumulated throughout the model run due to the use of reduced integration elements. The total artificial strain energy was always observed to be less than 1% of the total energy in the model. Preliminary sensitivity analyses were performed to determine the influence of several VUMAT inputs. It was found that for a lower BK coefficient for the critical fracture toughness a lower growth rate occurred. Furthermore, it was observed that the crack growth rate, da/dN, was significantly more sensitive to the local mixed mode coefficient, ϕ, than the critical strain energy release rate.

7.5. ERROR SOURCES AND RECOMMENDATIONS

Finally, we summarize some of the limitations of the model, which narrow the scope of validity and serve as topics for further investigation. These error sources are also to be taken into consideration in chapter 8, where the proposed fatigue model is validated using experimental data.

Fibre bridging: As discussed in section 2.1.4, fibre bridging behind the disbond front works as an energy dissipation mechanism. It slows down the crack growth rate, influencing primarily the constant in the Paris relation as shown by Yao et al. [20]. The proposed VUMAT model does not incorporate a correction for the influence of fibre bridging in the fatigue crack growth rate. Furthermore, the Paris data used in the model is derived from a test series on the HTA/6376C performed by Asp et al. [27], they noted no significant fibre bridging in their samples. Following the quasi-static test in chapter 5 and the fatigue calibration test in chapter 6, significant fibre bridging was observed in the delaminated areas. The model is therefore likely to be conservative, demonstrating a larger disbond growth than in the physical panels.

Local R-ratio: In the current fatigue damage formulation, the global R-ratio is used to calculate the element local ΔG (eq. (7.6)). This follows from the earlier fatigue models only being validated with coupon level test data. At the coupon level (eg. DCB, MMB) the applied R-ratio is equal to the local R-ratio, however when geometric non-linearities occur in a more complex structure it will no longer be correct to apply the global ΔG because locally the ratio between G_{max} and G_{min} will no longer be quadratically proportional to the global R-ratio. A sanity check has been performed on various elements throughout the cohesive zone in the current fatigue model. It has been verified that the global R-ratio is applicable to calculate the local ΔG. This is due to the fact that the crack is predominantly subject to a mode II loading, as demonstrated in fig. 7.6.

Enhanced shear fracture toughness during compression: In the current model, the element does not experience damage due to compression in the mode I direction. However it does not model the influence of compression on the shear behavior of the material. A proposed model by Li et al. [57] includes the increased shear fracture toughness when an element is subject to mode I closure based on a friction coefficient. Not including this in the Abaqus model results in a conservative result ie. larger disbond growth than experienced in experimental tests.

Fatigue data source: As is shown in table 7.1 a large degree of material input data is sourced from work by other authors investigating different material. As mentioned previously the HTA/6376C material is comparible to the T800/3900 as both are toughened carbon epoxies showing similar strength, stiffness and fracture toughness. Where possible of course, data for T800 is used, such as the critical SERR and the material strength and stiffness. The use of data not specific to the used material introduces a considerable source of error, however it is not possible to determine if it that error is conservative or not.

8

FATIGUE TESTING

Fatigue testing of 4 panels was performed to serve as a validation basis for the model described in chapter 7. The panel identification numbers are described in table 3.1. All 4 panels were tested following the same set-up as described in chapter 6. In section 8.1 the data analysis and validation procedure is described. The results and model validation are presented in section 8.2, including a discussion on error sources. One panel, ID:401_06, was also tested quasi-statically at every inspection interval to monitor the global stiffness degradation, this is discussed in section 8.3.

8.1. DATA ANALYSIS METHOD

All 4 panels are c-scanned at increasing cycle intervals. More crack growth is expected in the initial cycles, therefore more frequent c-scans are performed during the first 50'000 cycles to capture this behaviour.

The c-scans made throughout the fatigue tests were not full scans of the entire disbond region. This would be prohibitively time consuming, thus only the crack fronts were scanned, the region in between these two crack fronts is assumed to be completely disbonded, as is evident by the complete separation of the skin from the stiffener when the panels buckled.

An analysis of a large set of c-scan images (5 scans per panel, for 4 panels), revealed that the chamfered region of the stiffener, where the flange edges taper towards the skin (see fig. 1.1), were poorly captured by the c-scan device. On average, a width of 59.7mm was found to be properly captured by the c-scan, this corresponds with the point where the taper starts in the flange. In order to perform a proper validation of the Abaqus model it is decided to use a constant disbond width of 60mm for both the model and the c-scan images. In the original Abaqus model, a disbond width of 64mm was modeled, meaning that in the results file, 2mm is trimmed from each side of the cohesive areas.

A tool is created in Matlab to use the raw images from the c-scan device. The images are first filtered to remove colours depicted un-damaged material. This filtered image serves as the input for the Matlab image analysis tool. The tool crops the c-scan image and converts it to a binary matrix. Unwanted regions around the disbond area are removed. Next, two horizontal lines are drawn to connect the two disbond interface regions. These lines are always spaced 60mm apart to ensure compatibility and comparability with the Abaqus model. Next, the disbond area is filled allowing the total disbond area to be counted. The tool also measures the extreme disbond length (ie. measuring the distance between the two extreme points in the disbond growth direction. This process is illustrated in fig. 8.1.

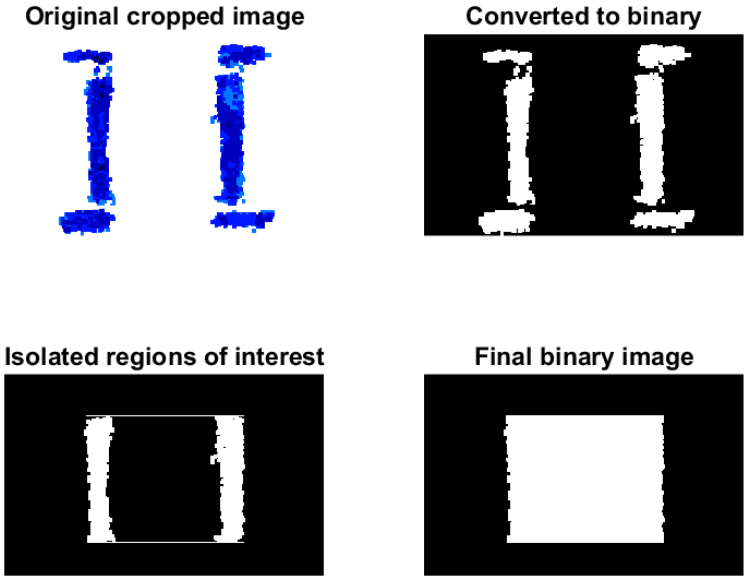

Figure 8.1: Image analysis tool: overview of processing steps

Error in data measurement: an error of $\pm 1.5mm$ was observed in the c-scan data for a single point measurement in section 6.2. Considering that the position of two crack fronts (each $\approx 60mm$ in length) must be determined an error in area measurement of at least $\pm 180mm^2$ exists. This is roughly equal to the 90th percentile confidence bounds shown in figs. 8.2, 8.4 and 8.5.

8.2. FATIGUE TEST RESULTS AND MODEL VALIDATION

In figs. 8.2 and 8.3 the processed data from the c-scan image analysis is presented, for disbond area and disbond length respectively. The data points are interpolated with a power2 curve ($f(x) = ax^b + c$) using Matlab's cftool, with varying degrees of goodness of fit. This is likely due to the low amount of growth, combined with the poor positioning system in the c-scan device, as discussed in section 6.2. For example, panel 401_06 shows a total growth of $219mm^2$, the error in area measurement as previously determined was $\pm 180mm^2$, which brings into question the significance of the measured data.

In the case of panel 401_04 the interpolated curve shows a negative trend, indicating a negative disbond growth in terms of area. The wide confidence bounds indicate that this fit is poor, either due to inconsistency in the image analysis tool or improper images from the c-scan device. Panels 401_03 and 401_06 show reasonable fits, with R values of 0.866 and 0.625, respectively. Panel 401_05 does show a positive area growth, however due to the three outliers in the lower left corner of the graph the fitted curve shows a linear trend rather than a power relation. Figure 8.3 shows positive disbond length growth for all 4 panels, although the confidence bounds for panel 401_04 are rather poor. Panel 401_03 shows a good fit, with an R=0.96.

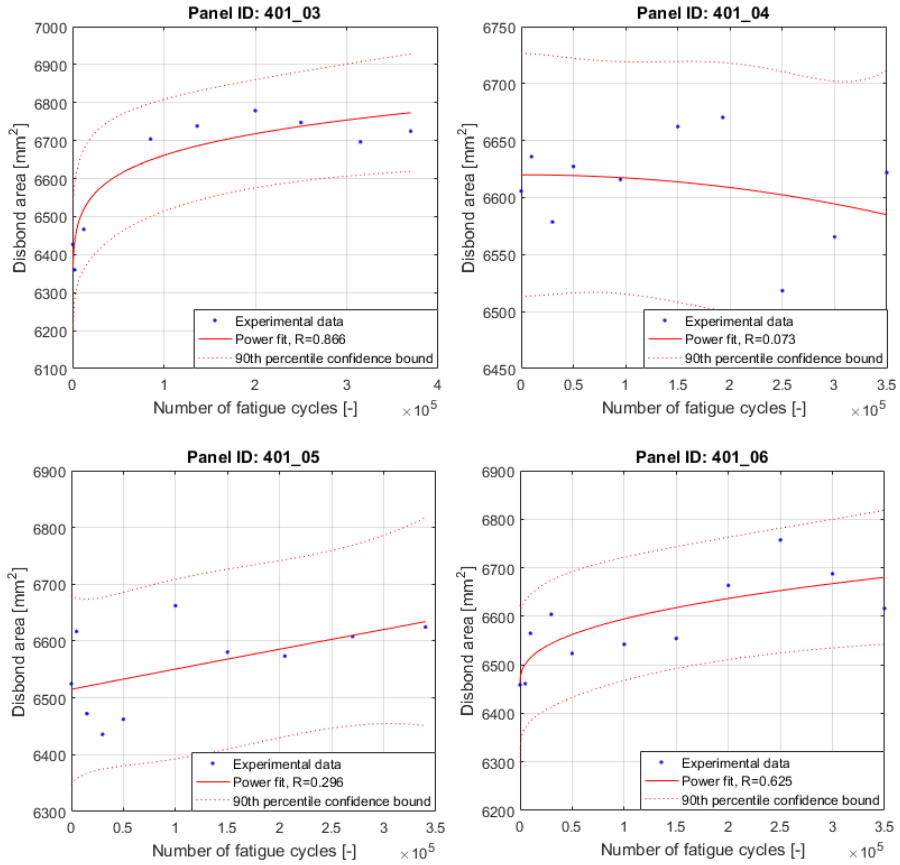

Figure 8.2: Disbond area growth under fatigue loading. (Fitted with a power equation - 90th percentile confidence bounds shown)

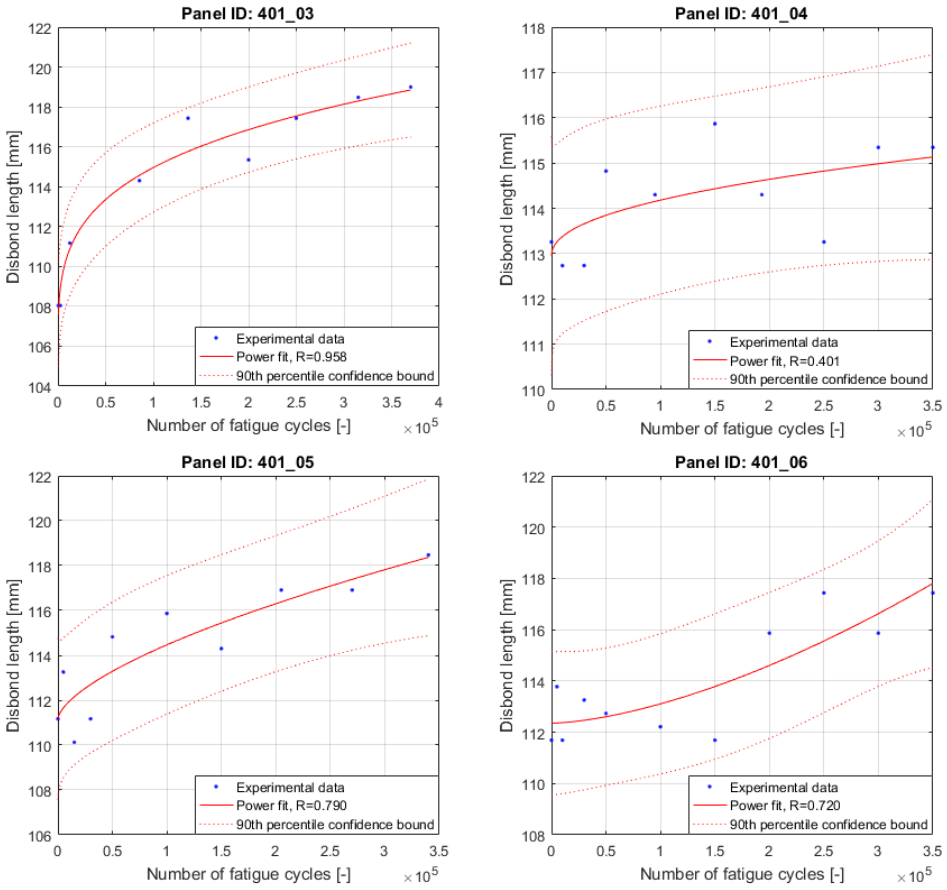

Figure 8.3: Disbond length growth under fatigue loading. (Fitted with a power equation - 90th percentile confidence bounds shown)

The problem with comparing the experimental data with the Abaqus model lies in the initial state of the delamination front. Firstly, after pre-cracking of the panel the delamination front is not perfectly straight, as it is in the Abaqus model. Secondly, the delamination area or length can vary between each panel. As discussed in section 7.1 two models were tested in fatigue, one with initial disbond length of 105mm and initial disbond area of 6300mm^2, the other model had a initial disbond length of 110mm and initial disbond area of 6600mm^2. This is the range of initial disbonds observed in the panels after pre-cracking.

In figs. 8.4 and 8.5, the disbond area growth obtained from the two Abaqus models is compared to the disbond area growth measured in panels 401_03 and 401_06. Panel 401_03 has an initial disbond of 6427mm^2 which is in the range of the two Abaqus models discussed earlier. The curves of both Abaqus models fall within the 90th percentile confidence bounds of the fitted curve. A reasonable agreement is observed between the Abaqus model with initial disbond of 6300mm^2 and the data fit. Similarly, in fig. 8.5 the Abaqus model falls between the 90th percentile confidence bounds of the experimental data, although the agreement in initial disbond rate is somewhat poor.

The Abaqus model does show, in both cases, a larger magnitude of growth, indicating a conservative aspect to the model. Sources for this conservative outcome are discussed in section 7.5. Panels 401_04 and 401_05 were not compared to the Abaqus models due to the poor quality of the test data. Clearly, a poor fit correspondence to the Abaqus data would result for these two panels.

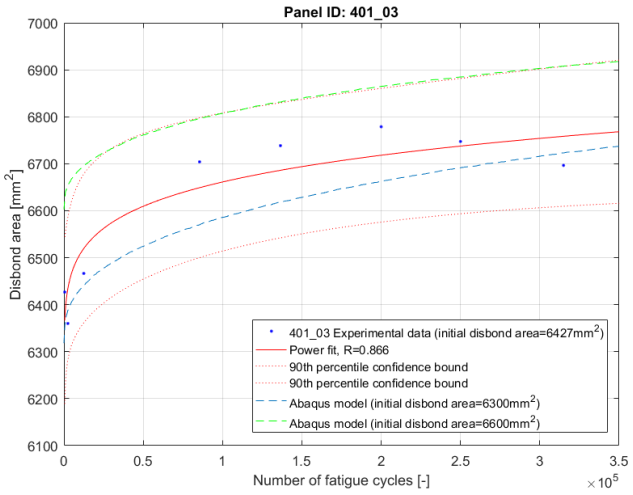

Figure 8.4: Validation of Abaqus fatigue models: disbond area growth panel 401_03

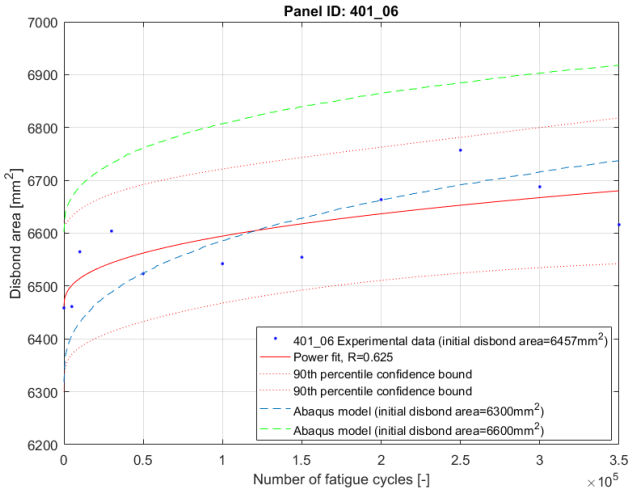

Figure 8.5: Validation of Abaqus fatigue models: disbond area growth panel 401_06

A final numerical validation method is the comparison of the disbond growth rate as a function of the disbond area. In fig. 8.6 the disbond growth rate data from all 4 panels and both Abaqus models is presented. As is clear from both the Abaqus models and panels 401_03 and 401_06, there is a large initial disbond growth rate, which approaches an asymptote close to zero. If we look back at fig. 7.5, we see that initially the corners of the cohesive region quickly are damaged due to both static and early fatigue damage. The difference in damage is far less pronounced going from N=10'000 to N=50'000 than going from N=200'000 to N=350'000. This corner coincides with the diagonal buckling pattern observed in the skin in fig. 4.7.

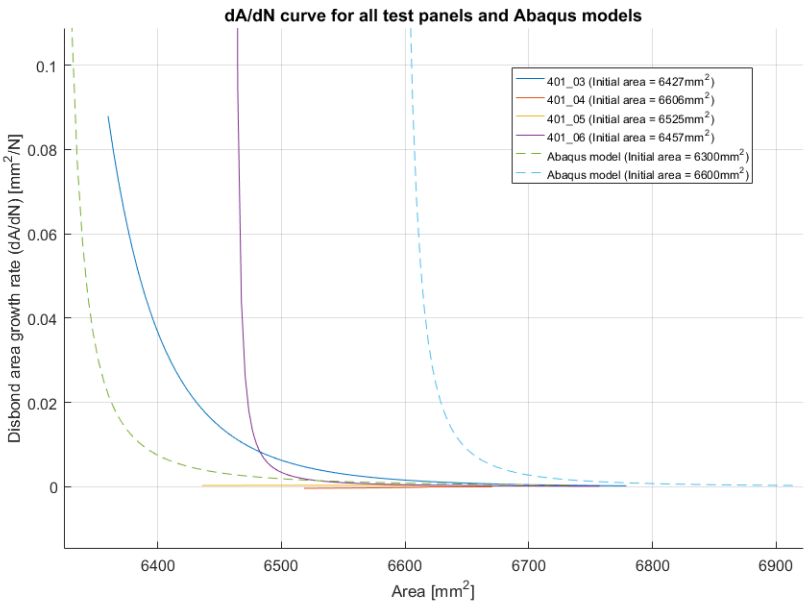

Figure 8.6: Disbond area growth rate

Finally, a visual validation is presented. One of the claimed advantages of cohesive zone models is the ability to capture the growth shape of complex delamination fronts. In fig. 8.7, the right hand corner is clearly showing greater delamination damage than the left hand corner. When comparing to the Abaqus result shown in fig. 7.5, shapes clearly match, indicating that the Abaqus model is able to capture the behaviour of the 2D delamination front.

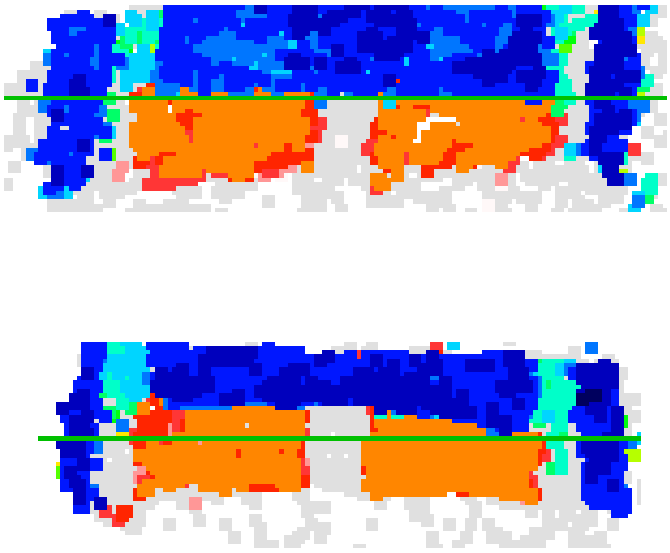

Figure 8.7: Disbond shape evolution of panel 401_03. Top: N=1, Bottom: N=315'000. Blue indicates delamination, orange/red indicates intact stiffener/skin interface. For spatial reference see figs. 7.1 and 7.5, where the equivalent section is shown in the numerical model.

8.3. GLOBAL STIFFNESS MONITORING

It is assumed that due to large difference between the ultimate load ($\approx -120kN$) and the maximum applied fatigue load (-47kN), the impact of intra-laminar damage will be minimal to the stiffener web and flanges. It is virtually impossible though to accurately monitor the intra-laminar behaviour of the stiffening element. Firstly, the ultra-sonic transducer is not able to scan near the corners where the flanges meet the stiffener. Secondly, performing c-scans for the entire stiffener in addition to the disbond region would be a prohibitively time consuming task. To gain some understanding of the intra-laminar behaviour, quasi-static tests are performed on one panel (ID:401_06) each time the fatigue test is stopped for c-scan inspection. Before the panel is removed for inspection it was instrumented with an LVDT and loaded to -50kN, similar to the test setup for the static test in section 5.1. The load shortening curves are presented in fig. 8.8, no evident global stiffness reduction of the panel. The stiffness reduction (measured by comparing the slope of the linear data in fig. 8.8) shows a 2.0% reduction in stiffness after 300'000 cycles and a 2.7% reduction in stiffness after 350'000 cycles. This indicates that there was no significant intra-laminar fatigue damage in the global structure.

Inspection of a panel after 350'000 fatigue cycles was performed using a CNC Mitutoyo Coordinate System Measuring Machine. This revealed a permanent deformation (shortening) of the stiffener (ie. plastic compression) of 0.55mm when compared to a pristine panel. This shows that, some plastic deformation occurs of the stiffener during fatigue loading, however this does not affect the overall stiffness significantly.

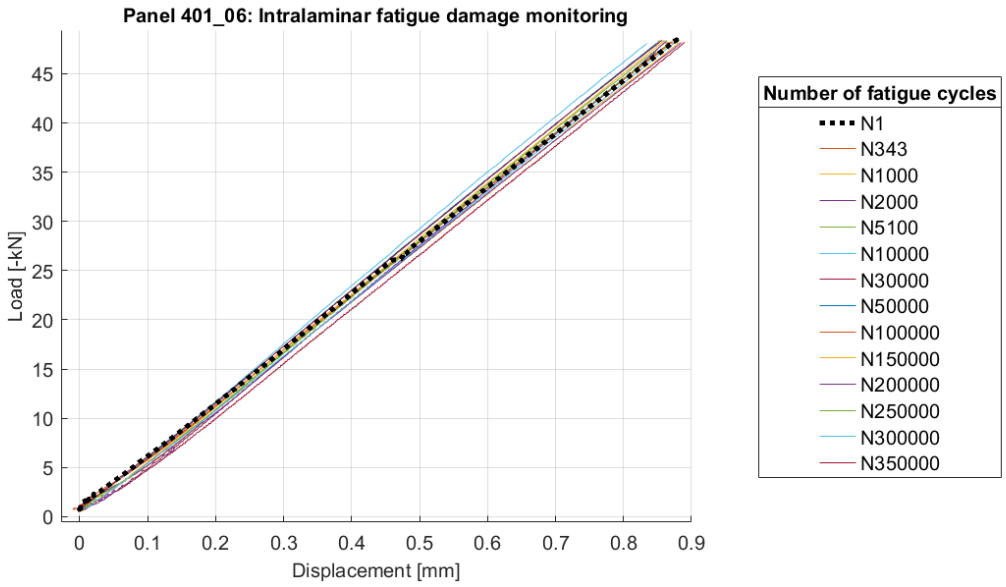

Figure 8.8: Load shortening response of panel 401_06 during fatigue testing regime

PHASE III - RESIDUAL STRENGTH

9

RESIDUAL STRENGTH: MODEL, TESTS AND VALIDATION

The final stage of this thesis consists rather fittingly of the destructive testing of all the panels tested in fatigue. Presented in section 9.1 is the revised quasi-static model first introduced in section 4.4. This is followed by the testing of the four fatigue panels in section 9.2 and the failure mode analysis in section 9.2.1.

9.1. RESIDUAL STRENGTH MODEL

A residual strength model is implemented in Abaqus explicit using COH3D8 elements for the cohesive sections. The model basis is identical to the quasi-static model described in section 4.4. A Hashin initiation criterion is used in combination with a bi-linear softening law for quasi-static damage (in the composite sections). To recreate the damaged state of the panel after fatigue damage (350k cycles), the state of the cohesive section in the fatigue model is imported into the new residual strength model. Cohesive elements which are fully damaged in the fatigue model are deleted from the residual strength model. Partially damaged elements are not considered, therefore they are included as pristine elements in the residual strength model.

In fig. 9.1 the load displacement curve for the damaged and pristine model (from section 4.4) are shown. It is evident that the deletion of several cohesive elements near the crack tip has an insignificant influence on the behaviour of the model. Both models fail at an ultimate load of -131kN and show the same failure mode (compression in the stiffener web). When observing the failure mode it is evident that the stiffener is the primary load carrying member, controlling the ultimate load.

A model of only the stiffener is tested to verify the hypothesis that the bonded skin has a marginal influence on the ultimate load of the panel. If the stiffener is allowed to buckle (with the inclusion of an imperfection in the model) it fails at a load of -107kN. When no imperfection is included, a failure load of -117kN is achieved. Compared to an ultimate load of -131kN of the entire panel, ie. including the skin; it is evident that the stiffener is the primary load carrying element.

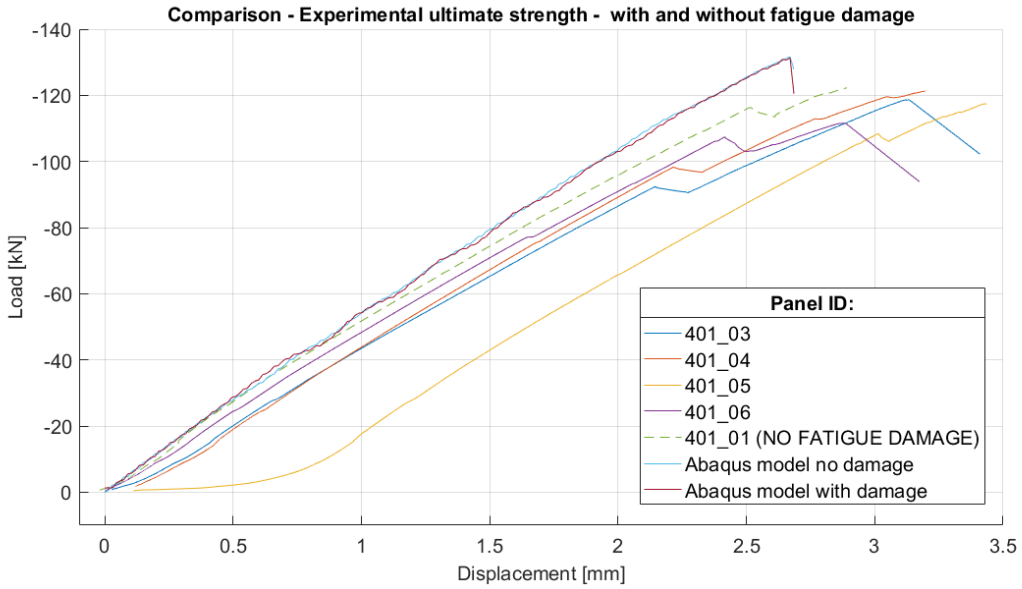

Figure 9.1: Comparison of residual strength model with the pristine strength model presented in section 4.4 and experimental data from residual strength tests

This is compatible with the findings by Yap et al. [2], where the ultimate load of a panel with multiple stiffeners was insignificantly reduced by the presence of an artificial disbond in one of the stiffeners.

Comparison with the test data in fig. 9.1 shows that the Abaqus model has a marginally higher stiffness than the tested panels. The same results were found in chapter 5 where a pristine model was validated with test data from a pristine panel. Again, a noticable kink is missing from the Abaqus models compared to the test data. In chapter 5 it was observed that this kink is due to a jump in delamination growth, this was not captured in the Abaqus models.

9.2. RESIDUAL STRENGTH TEST OF FATIGUE PANELS

The residual strength tests were performed in an identical manner to the initial static test described in chapter 5. All four panels tested in fatigue were subject to quasi-static testing in compression until failure. In fig. 9.1 the load shortening curves are presented, together with the load shortening of the Abaqus models and the pristine panel (401_01) tested in chapter 5. A summary of the buckling loads and failure loads of all panels and static model is presented in table 9.1.

Firstly the outliers: panel 401_05 is noticeably offset to the right in fig. 9.1. This is attributed to improper clamping before starting the experiment; the panel likely was not contacting the load application surface. As the rig was loaded, the panel seated and followed a load-displacement curve of comparable stiffness to the other panels/models. The buckling load of SG2 on panel 401_05 is more than twice that of the other panels, which may be due to instrumentation error or again due to the poor set-up in the rig. Finally, the buckling load of panel 401_06 is not shown in table 9.1 because the panel was not fitted with strain gauges.

The buckling loads of strain gauge 4 is lower for all panels tested in fatigue, compared to the pristine panel (401_01). However we have only 1 data point for the pristine panel and therefore no significant conclusion can be drawn. For strain gauge it is even more difficult to draw a meaningful conclusion because the buckling loads for both panel 401_04 and 401_05 are higher than for the pristine panel, admittedly the buckling load for panel 401_05 is likely an outlier.

A decrease in ultimate load is observed in all of the fatigue tested panel, varying between 1.1kN lower for panel 401_04 to 10.8kN lower for panel 401_06. All panels also showed the same or an increase in displacement at failure, which is visible in fig. 9.1 where a slight relaxation in stiffness is observed.

Table 9.1: Summary of all quasi-static test results. All loads are compressive.

Panel ID	Buckling Load SG2 [kN]	Buckling Load SG4 [kN]	Ult. Load [kN]	Disp. at failure [mm]
401_01	14.69	17.2	122.3	2.87
401_03	12.49	12.25	118.5	3.13
401_04	16.68	16.68	121.2	3.19
401_05	38.5	10.85	117.5	3.43
401_06	n/a	n/a	111.5	2.87
Abaqus w/o damage	13.02	17.23	131.7	2.67

9.2.1. FAILURE MODE ANALYSIS

Following the quasi-static residual strength tests the panels were inspected visually to determine the mode of failure, which upon initial inspection appeared to differ between the panels. Common failure modes include ply failure in the skin, crushing of the stiffener and skin-stiffener delamination. Below, the failure modes per panel are described and analysed.

401_03 & 401_05:
Both panels showed very similar failure modes. Large delamination growth was observed, growing in both directions from the initial delamination towards the clamped ends of the panel. This resulted in the skin buckling with a larger half-wave compared to the panels with just a 100mm delamination. The delamination stopped growing just short of the clamped ends. Significant crushing was observed on both of the stiffener ends ie. where the load was applied to the stiffener. This is illustrated in fig. 9.2. Significant fibre and matrix failure were observed in the buckling region of the skin, particularly near the sides of the skin constrained by the anti-buckling support. The delamination growth in both directions, along with the skin failure near the anti-buckling supports can be observed in fig. 9.3.

Figure 9.2: Crushing of stiffener clamped end. Panel ID:401_05

Figure 9.3: Delamination growth and skin failure. Panel ID:401_05

401_04:
Compared to panels 401_03 and 401_05, a smaller delamination growth 'jump' was observed. The primary failure mode was the crushing of the stiffener web, approximately halfway between the clamped ends. Furthermore, the stiffener flanges showed crippling failure. The skin slipped out of the anti-buckling supports when the stiffener failed catastrophically, inducing additional damage to the skin. Contrary to the other panels, no crushing of the stiffener ends was observed.

Figure 9.4: Skin failure, crippling of stiffener flange (marked by red arrow) and crushing of stiffener web. Panel ID:401_04

401_06:
Similar to panel 401_04, the skin slipped out of the anti-buckling supports after. However, unlike the other panels it showed delamination growth in just one direction (towards the top of the panel). In this case the delamination grew completely towards the loaded side of the panel. Furthermore, crushing of the edge of the stiffener web (as was seen in panels 401_03 and 401_05) only occurred on the top side, the same side in which the delamination grew. The bottom side showed no sign of crushing or significant delamination growth.

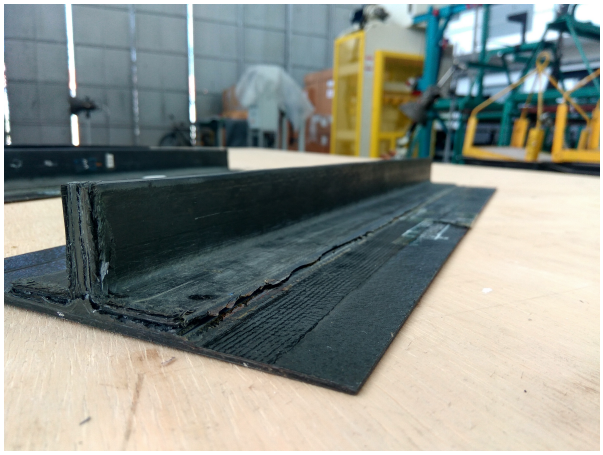

Figure 9.5: Complete delamination and stiffener end crushing. Panel ID:401_06

Summary of failure mode analysis
All the panels showed skin failure in the buckling region, to a certain degree. The panels, whose skins slipped out of the anti-buckling support showed a larger amount of damage. Crushing and brooming of the stiffener ends in the clamped region was observed in panels 401_03, 401_04 and 401_06. Panel 401_05 showed no crushing of the stiffener edges, this was also observed in the failure mode of the pristine panel (ID: 401_01) under quasi-static testing in chapter 5.

A correlation is observed between the direction of delamination growth and the crushing of the ends of the stiffener web. If significant delamination growth occurred, the ends of the stiffener web showed crushing on the same side(s) as the direction of delamination growth. This interesting phenomenon may be due to improper shimming of the panel in the test rig clamps, allowing the stiffener to crush and broom out. It would be interesting to stop a quasi-static test after the first rapid delamination growth occurs to check if the stiffener has crushed, if this is not the case it would mean that the rapid delamination growth is not a direct result of the crushing of the stiffener.

10

CONCLUSION

The global aim of this investigation is reiterated: **to analyse the durability of bonded stiffened composite panels with initial flaws under cyclic compressive loading**. To prepare for this task, an in-depth literature study has been performed on the stability and durability of bonded composite structures, looking at novel modelling techniques. Looking back at the research questions posed in section 1.1, the three supporting questions have been addressed:

1. What is the state-of-the-art knowledge regarding the modelling of bonds in composite structures under static and fatigue loading?
2. How does the disbond size and position influence the stability of a stiffened composite panel?
3. **What is the correlation between disbond growth rate under fatigue loading and the disbond size?**

The first research question is thoroughly discussed in the literature survey, covering basics of bonding techniques and how their material parameters are influenced. This served primarily to investigate the characteristics of bond material, these material properties will eventually be used as input for the damage model. Of particular interest were the studies on fracture toughness and fibre bridging, which have significant influence on the fatigue characteristics of bonded and laminated interfaces.

Research question 2 was covered extensively in the literature survey and partially in the thesis work. Numerous studies have shown that as the disbond grows, the buckling load decreases [2, 3, 8]. Under a load controlled fatigue experiment this means that buckling occurs earlier as the disbond grows, further driving open the crack front.

However, several sources [2, 3], demonstrate so called 'critical' disbond lengths. Yap et al. [2] show that for a disbond size of lower than 6% of the panel length marginal disbond growth occurs. Similarly, Zarouchas and Alderliesten [3] demonstrate a lower threshold for disbond growth. conversely, an upper limit for disbond growth is shown to exist by both sources. Above this threshold the buckling mode changes to include multiple half-waves which has an arresting affect on the disbond.

A linear buckling analysis in section 4.2 showed indeed a decrease in buckling load as the disbond size is increased. Residual strength tests performed in section 9.2 showed a decrease in buckling load for one of the panels subject to fatigue testing, however the same conclusion could not be confidently drawn from the test data from two other panels.

The primary objective, introduced in section 1.1 is: **To experimentally validate a fatigue crack growth model, using a cohesive zone formulation, on the sub-assembly level by analyzing fatigue crack growth in artificially disbonded stiffened panels**.

To achieve this objective, a cohesive zone model with static and fatigue damage formulation is used to simulate delamination growth in a co-cured panel with an initial delamination. The selected model is based on the original work by Harper and Hallett [46, 47], which was further developed by Kawashita et al. [45].

In the final model, the cohesive element damage is controlled by a single damage parameter, split into a static portion and a fatigue portion. Static damage is introduced by means of a bi-linear softening law. The material is linear elastic until a quadratic stress damage criterion is met, thereafter the stiffness and strength (as a function of element nodal displacement) is linearly decreased by means of a single damage parameter. Fatigue damage is initiated once a threshold SERR has been reached, damage propagation is then governed by means of a Paris type relation. Damage introduced is irreversible so when one element is fully damaged it means that the crack front has propagated. This may be by means of pure static or pure fatigue loading, or a combination of both.

Four specimens were subject to extensive fatigue testing in order to validate the fatigue model. Periodic c-scans were performed to track the progression of the delamination fronts. Overall, a reasonable agreement was found in terms of disbond area growth between the model and two of the specimens. However the model was consistently conservative, indicating a larger disbond growth than observed in the experimental tests. Reasons for these conservative results may include the presence of fibre bridging in the T800/3900 material, which was not observed in the HTA/6376C material from which the Paris data was obtained.

Two of the four panels showed an inconclusive growth in terms of area, however all panels showed conclusive growth in disbond length. This result may be attributed to the relatively large systematic measurement error of the c-scan setup compared to the amount of disbond growth. The measurement error for the disbond area was estimated to be $\pm 180 mm^2$, whilst the total measured area for the panels was in the order of $200 mm^2$.

A visual validation of the crack front propagation showed good agreement between the model and the tested panels. In both cases a clear delamination growth was seen in the corners of the crack front. Due to the diagonal buckling pattern of the skin, the delamination front clearly grew faster and larger on one of the crack front corners.

Material input for the model came from open literature and in-house testing. The open literature data was for a CFRP comparable to the material used in this thesis and is therefore considered a good starting point. However,this means that the model can not be considered properly validated. Fatigue delamination growth data (ie. Paris curve data) is required for this specific material before it can be properly validated in terms of area disbond growth. However, given that the delamination shape was reproduced well by the model it shows that the application of CZMs is promising. This is further backed up by a reasonable prediction of the area growth rate, despite using Paris data for a different material.

11

RECOMMENDATIONS

A summary of recommendations is presented in this chapter. It is meant as a guide for future students and researchers continuing the INOVA project. For the sake of clarity a division is made between the experimental and numerical recommendations.

11.1. EXPERIMENTAL

The method of data aqcuisition may be drastically improved by means of an in-situ NDT technique as described in appendix B. Methods such as DIC analysis or a thermographic method may be applied to monitor the crack advancement in real or near real time. Granted, the resolution of such techniques is not as good as an ultrasonic scan. Therefore it is proposed to use the in-situ NDT methods to trigger a c-scan, once it has been established that growth has occurred. This will make sure that c-scans are performed only when required, reducing testing time and repeatability errors associated with the removal of the panel from the rig for c-scan inspection. A final improvement with respect to the inspection method would be to employ a CNC rig for consistent and repeatable c-scanning results using the single point probe available at the ITA lab.

A target crack growth of 40mm was not achieved in the current set-up. Given the scatter of the c-scan results it is advised to have a larger magnitude of crack growth to validate the numerical model. This may be achieved be either increasing the cyclic load, increasing the number of cycles or decreasing the initial delamination size. Other options include removing the anti-buckling supports from the skin, however this change in boundary conditions would entirely change the fracture mode near the crack tip.

A final comment with respect to the manufacturing of the panels: extending the Teflon tape insert beyond the width of the stiffener flanges is advisable. It ensures that the stiffener is not connected in any manner to the skin due to excess resin flowing out during curing. This in turn would eliminate the need to excessively pre-crack the panels using the 7-point bending rig to loosen the stiffener from the skin in the disbond area (a pre-crack is still needed though to initiate the crack fronts).

11.2. NUMERICAL

The current cohesive zone formulation for fatigue damage requires the input of the R-ratio. In this thesis the global R-ratio was used, which by coincidence was equal to the local R-ratio experienced by the cohesive elements. This use of the R-ratio is an artefact from early fatigue CZMs which were focused only on coupon level experiments. In all such cases the global and local R-ratio are equal. However, more complex geometries and load cases may introduce geometric non-linearities such that the local R-ratio is not equal to the global R-ratio. An option would be to model two instances of the same part, one at P_{min} and one at P_{max}. In this way the local R-ratio is always known and damage may be updated simultaneously in both instances of the model at every time-increment. From a computational perspective this will be expensive to run, however it would allow the cycle-jump technique to be employed, which is orders of magnitude faster than modelling every fatigue load cycle.

Since previous work in the field of fatigue delamination growth has often been limited to coupon level experiments, the current Paris parameters are one dimensional. When increasing the test scale to the sub-component level it does not make sense to describe crack growth as a one dimensional parameter (da/dN). Intuitively, area should be used as a basis since it is an area that is ultimately measured. Furthermore, the similitude parameters currently used to calculate the crack growth rate do not fully describe the load cycle. In this thesis only the ΔG was used. To fully describe the fatigue load cycle we also require a reference point such as the G_{mean}, G_{max} or G_{min}.

We must also look at the physical problem that is actually occurring in the damage area. Paris data related a one-dimensional crack to the entire damage state in a coupon. Can this be translated properly to a larger scale? In the case of mode II fracture, the damage zone is not limited to the fracture tip. How do we accurately describe the damage state further ahead of the crack tip, where micro-cracks are forming and coalescing? These issues must be addressed if we are to fully and correctly capture the damage state in a structure.

Finally, as mentioned numerous times, the Paris coefficients used in the current numerical model are taken from a single open literature source. Despite the materials being comparible, both are toughened epoxies reinforced with carbon fibres, it is advised to perform coupon level tests to obtain data specific to the material used. Furthermore, the influence of fibre bridging must be investigated, in addition to the effect of friction (ie. compressive mode I) on the mode II behaviour of the material. Finally, an investigation into the influence of fibre angles of the interface plies on the fatigue crack behaviour is warranted. Needless to say, given the inherent scatter in fatigue testing of composites, the aforementioned investigations would be time consuming and expensive.

BIBLIOGRAPHY

[1] M. G. Song, J. H. Kweon, J. H. Choi, J. H. Byun, M. H. Song, S. J. Shin, and T. J. Lee, *Effect of manufacturing methods on the shear strength of composite single-lap bonded joints,* Composite Structures **92**, 2194 (2010).

[2] J. W. H. Yap, M. L. Scott, R. S. Thomson, and D. Hachenberg, *The analysis of skin-to-stiffener debonding in composite aerospace structures,* Composite Structures **57**, 425 (2002).

[3] D. S. Zarouchas and R. C. Alderliesten, *The effect of disbonds on stability aspects of adhesively bonded aluminum panels during compression loading ,* Thin-Walled Structures **96**, 372 (2015).

[4] R. Krueger, *Virtual crack closure technique: History, approach, and applications,* Applied Mechanics Reviews **57**, 109 (2004).

[5] Dassault Systèmes, *Abaqus 6.14 documentation,* (2014).

[6] L. Amaro de Oliveira, D. S. Alves, and M. V. Donadon, *Fatigue driven delamiation of composites and adhesives: critical review and comparative study,* [submitted] (2018).

[7] A. Turon, J. Costa, P. P. Camanho, and C. G. Davila, *Simulation of delamination in composites under high-cycle fatigue ,* Composites Part A: Applied Science and Manufacturing **38**, 2270 (2007).

[8] M. V. Donadon and D. P. Lauda, *A damage model for the prediction of static and fatigue-driven delamination in composite laminates,* Journal of Composite Materials **49**, 1995 (2015).

[9] J. N. Zalameda, E. R. Burke, F. R. Parker, J. P. Seebo, C. W. Wright, and J. B. Bly, *Thermography inspection for early detection of composite damage in structures during fatigue loading,* , 835403 (2012).

[10] S. Tandon, *M.Sc. Thesis: Fatigue disbond growth in primary aerospace structures,* (2016).

[11] R. C. Alderliesten, *Damage tolerance of bonded aircraft structures ,* International Journal of Fatigue **31**, 1024 (2009).

[12] S. Budhe, M. D. Banea, S. de Barros, and L. F. M. da Silva, *An updated review of adhesively bonded joints in composite materials ,* International Journal of Adhesion and Adhesives **72**, 30 (2017).

[13] Y.-B. Park, M.-G. Song, J.-J. Kim, J.-H. Kweon, and J.-H. Choi, *Strength of carbon/epoxy composite single-lap bonded joints in various environmental conditions,* Composite Structures **92**, 2173 (2010).

[14] FAA, *Advisory Circular: 20-107B - Composite Aircraft Structure,* (2009).

[15] L. F. M. da Silva, R. J. C. Carbas, G. W. Critchlow, M. A. V. Figueiredo, and K. Brown, *Effect of material, geometry, surface treatment and environment on the shear strength of single lap joints ,* International Journal of Adhesion and Adhesives **29**, 621 (2009).

[16] J. Mohan, A. Ivanković, and N. Murphy, *Mode I fracture toughness of co-cured and secondary bonded composite joints,* International Journal of Adhesion and Adhesives **51**, 13 (2014).

[17] J. Mohan, A. Ivanković, and N. Murphy, *Mixed-mode fracture toughness of co-cured and secondary bonded composite joints,* Engineering Fracture Mechanics **134**, 148 (2015).

[18] M. Kanerva, E. Sarlin, M. Hoikkanen, K. Rämö, O. Saarela, and J. Vuorinen, *Interface modification of glass fibre–polyester composite–composite joints using peel plies,* International Journal of Adhesion and Adhesives **59**, 40 (2015).

[19] L. Yao, Y. Sun, M. Zhao, R. Alderliesten, and R. Benedictus, *Stress ratio dependence of fibre bridging significance in mode I fatigue delamination growth of composite laminates,* Composites Part A: Applied Science and Manufacturing **95**, 65 (2017).

[20] L. Yao, R. Alderliesten, and R. Benedictus, *The effect of fibre bridging on the Paris relation for mode I fatigue delamination growth in composites,* Composite Structures **140**, 125 (2016).

[21] L. Yao, R. Alderliesten, M. Zhao, and R. Benedictus, *Bridging effect on mode I fatigue delamination behavior in composite laminates,* Composites Part A: Applied Science and Manufacturing **63**, 103 (2014).

[22] J. A. Pascoe, R. C. Alderliesten, and R. Benedictus, *Methods for the prediction of fatigue delamination growth in composites and adhesive bonds – A critical review ,* Engineering Fracture Mechanics **112–113**, 72 (2013).

[23] A. C. Orifici, I. O. de Zarate Alberdi, R. S. Thomson, and J. Bayandor, *Compression and post-buckling damage growth and collapse analysis of flat composite stiffened panels,* Composites Science and Technology **68**, 3150 (2008).

[24] H. Klein and A. Kling, *Buckling and postbuckling of stringer stiffened fibre composite curved panels – Tests and computations,* Composite Structures **73**, 150 (2006).

[25] C.-W. Kong, I.-C. Lee, C.-G. Kim, and C.-S. Hong, *Postbuckling and failure of stiffened composite panels under axial compression,* Composite Structures **42**, 13 (1998).

[26] S. G. P. Castro and M. V. Donadon, *Assembly of semi-analytical models to address linear buckling and vibration of stiffened composite panels with debonding defect ,* Composite Structures **160**, 232 (2017).

[27] L. E. Asp, A. Sjögren, and E. S. Greenhalgh, *Delamination Growth and Thresholds in a Carbon / Epoxy Composite Under Fatigue Loading,* Journal of Composites Technology & Research **23**, 55 (2001).

[28] J.-A. Pascoe, *Characteristics of fatigue crack growth in adhesive bonds,* Ph.D. thesis, Delft University of Technology (2016).

[29] G. Irwin, *Analysis of Stresses and Strains Near the End of a Crack Traversing a Plate,* Journal of Applied Mechanics **24**, 361 (1957).

[30] P. C. Paris, M. P. Gomez, and W. E. Anderson, *A rational analytic theory of fatigue,* The Trend in Engineering **13**, 9 (1961).

[31] P. Paris and F. Erdogan, *A Critical Analysis of Crack Propagation Laws,* Journal of Basic Engineering **85**, 528 (1963).

[32] C. Rans, R. Alderliesten, and R. Benedictus, *Misinterpreting the results: How similitude can improve our understanding of fatigue delamination growth,* Composites Science and Technology **71**, 230 (2011).

[33] O. J. Nixon-pearson, S. R. Hallett, P. W. Harper, and L. F. Kawashita, *Damage development in open-hole composite specimens in fatigue . Part 2 : Numerical modelling,* Composite Structures **106**, 890 (2013).

[34] S. Donaldson and S. Mall, *Delamination Growth in Graphite/Epoxy Composites Subjected to Cyclic Mode III Loading,* Journal of Reinforced Plastics and Composites **8**, 91 (1989).

[35] M. Miura, Y. Shindo, F. Narita, and S. Watanabe, *Mode III fatigue delamination growth of glass fiber reinforced polymer woven laminates at cryogenic temperatures,* Cryogenics **49**, 407 (2009).

[36] M. Kenane and M. L. Benzeggagh, *Mixed-mode delamination fracture toughness of unidirectional glass/epoxy composites under fatigue loading,* Composites Science and Technology **57**, 597 (1997).

[37] M. Benzeggagh and M. Kenane, *Measurement of mixed-mode delamination fracture toughness of unidirectional glass/epoxy composites with mixed-mode bending apparatus,* Composites Science and Technology **56**, 439 (1996).

[38] N. Blanco, E. K. Gamstedt, L. E. Asp, and J. Costa, *Mixed-mode delamination growth in carbon-fibre composite laminates under cyclic loading,* International Journal of Solids and Structures **41**, 4219 (2004).

[39] D. S. Dugdale, *Yielding of steel sheets containing slits,* Journal of the mechanics and physics of solids **8**, 100 (1960).

[40] G. I. Barenblatt, *The mathematical theory of equilibrium cracks in brittle fracture,* Advances in Applied Mechanics **2**, 55 (1962).

[41] G. I. Barenblatt, *The formation of equilibrium cracks during brittle fracture. General ideas and hypotheses. Axially-symmetric cracks,* Journal of Applied Mathematics and Mechanics **23**, 622 (1959).

[42] G. I. Barenblatt, *Equilibrium cracks formed during brittle fracture rectilinear cracks in plane plates,* Journal of Applied Mathematics and Mechanics **23**, 1009 (1959).

[43] R. H. J. Peerlings, W. A. M. Brekelmans, R. de Borst, and M. G. D. Geers, *Gradient-enhanced damage modelling of high-cycle fatigue,* International Journal for Numerical Methods in Engineering **49**, 1547 (2000).

[44] P. Robinson, U. Galvanetto, D. Tumino, G. Bellucci, and D. Violeau, *Numerical simulation of fatigue-driven delamination using interface elements,* International Journal for Numerical Methods in Engineering **63**, 1824 (2005).

[45] L. F. Kawashita and S. R. Hallett, *A crack tip tracking algorithm for cohesive interface element analysis of fatigue delamination propagation in composite materials,* International Journal of Solids and Structures **49**, 2898 (2012).

[46] P. W. Harper and S. R. Hallett, *A fatigue degradation law for cohesive interface elements - Development and application to composite materials,* International Journal of Fatigue **32**, 1774 (2010).

[47] P. W. Harper and S. R. Hallett, *Cohesive zone length in numerical simulations of composite delamination,* Engineering Fracture Mechanics **75**, 4774 (2008).

[48] C. B. G. Brito, *Hygrothermal Effects on the Interlaminar Fracture Toughness of Composite Joints,* (2017).

[49] M. I. Arbelo, *FAPESP REPORT: Modelagem de Junções Coladas para Aplicações em Estruturas Aeronáuticas de Materiais Compósitos*, Tech. Rep. (FAPESP, 2017).

[50] Z. Hashin and A. Rotem, *A cumulative damage theory of fatigue failure,* Materials Science and Engineering **34**, 147 (1978).

[51] J. van Rijn and J. F. M. Wiggenraad, *A Seven-point Bending Test to Determine the Strength of the Skin-stiffener Interface in Composite Aircraft Panels*, Tech. Rep. (2000).

[52] J. Singer, J. Arbocz, and T. Weller, *Buckling Experiments: Experimental Methods in Buckling of Thin-Walled Structures Basic Concepts, Columns, Beams and Plates Volume 1* (John Wiley & Sons, Inc., 1998).

[53] Sonotron NDT ltd., *ISONIC 2006 Manual,* (2006).

[54] M. May and S. R. Hallett, *Composites : Part A A combined model for initiation and propagation of damage under fatigue loading for cohesive interface elements,* Composites Part A **41**, 1787 (2010).

[55] W.-G. Jiang, S. R. Hallett, B. G. Green, and M. R. Wisnom, *A concise interface constitutive law for analysis of delamination and splitting in composite materials and its application to scaled notched tensile specimens,* Int. J. Numer. Meth. Engng. **69**, 1982 (2007).

[56] T. K. O'Brien, G. B. Murri, and S. A. Salpekar, *Interlaminar shear fracture toughness and fatigue thresholds for composite materials,* (1987).

[57] X. Li, S. R. Hallett, and M. R. Wisnom, *Predicting the effect of through-thickness compressive stress on delamination using interface elements,* Composites Part A: Applied Science and Manufacturing **39**, 218 (2008).

[58] C. G. Dávila and C. Bisagni, *Fatigue life and damage tolerance of postbuckled composite stiffened structures with initial delamination,* Composite Structures **161**, 73 (2017).

[59] R. Yang and Y. He, *Optically and non-optically excited thermography for composites: A review,* Infrared Physics & Technology **75**, 26 (2016).

A

APPENDIX A - GANTT CHART

Level	WBS	Task	Start Start Date	End End Date	Task Duration	feb 1	feb 8	feb 15	feb 22	mrt 1	mrt 8	mrt 15	mrt 22	mrt 29	apr 5	apr 12	apr 19	apr 26	mei 3	mei 10	mei 17	mei 24	mei 31	jun 7	jun 14	jun 21	jun 28	jul 5
P	1	Literature Study	6-2-2017	16-6-2017	95																						
A	1.1	AE4010	6-2-2017	21-4-2017	55																						
B	1.1.1	Literacy Training	6-2-2017	6-3-2017	21																						
B	1.1.2	Gantt chart	6-2-2017	10-2-2017	5																						
A	1.2	Mid term Lit. Study	13-2-2017	21-4-2017	50																						
A	1.3	Final Hand-in	24-4-2017	16-6-2017	40																						
P	2	Phase 1	27-2-2017	30-6-2017	90																						
A	2.1	**Abaqus Modelling**	**24-4-2017**	**30-6-2017**	**50**																						
B	2.1.1	Linear Buckling	24-4-2017	12-5-2017	15																						
B	2.1.2	Non-Linear Buckling	15-5-2017	9-6-2017	20																						
B	2.1.3	Ultimate Load	12-6-2017	30-6-2017	15																						
A	2.2	**Testing**	**27-2-2017**	**9-3-2017**	**9**																						
B	2.2.1	Static Test	27-2-2017	9-3-2017	9																						
B	2.2.2	Static Data Analysis	16-3-2017	24-3-2017	7																						
P	3	Holiday	3-7-2017	23-7-2017	15																						
A	3.1	Ciao	3-7-2017	23-7-2017	15																						
P	4	Phase 2	24-7-2017	22-9-2017	45																						
A	4.1	**Abaqus Modelling**	**24-7-2017**	**15-9-2017**	**40**																						
B	4.1.1	Damage Init.	24-7-2017	11-8-2017	15																						
B	4.1.2	Interface Damage	14-8-2017	1-9-2017	15																						
B	4.1.3	Residual Ult. Load	4-9-2017	15-9-2017	10																						
B	4.1.4	Contingency week	17-9-2017	22-9-2017	5																						
A	4.2	**Testing**	24-7-2017	12-8-2017	15																						
B	4.2.1	Fatigue	24-7-2017	12-8-2017	15																						
B	4.2.2	Fatigue Data Analysis	24-7-2017	12-8-2017	15																						
P	5	Reporting (& Validation)	17-9-2017	8-12-2017	60																						
A	5.1	Phase 1 reporting	25-6-2017	30-6-2017	5																						
A	5.2	Report outline/template	17-9-2017	22-9-2017	5																						
A	5.3	Mid term review	25-9-2017	20-10-2017	20																						
A	5.4	Final Review/Green Light	23-10-2017	17-11-2017	20																						
A	5.5	Hand in	20-11-2017	8-12-2017	15																						

Figure A.1: Gantt chart of the thesis. Period Jan-Jun.

Level	WBS	Task	Start Start Date	End End Date	Task Duration	jul 12	jul 19	jul 26	aug 2	aug 9	aug 16	aug 23	aug 30	sep 6	sep 13	sep 20	sep 27	okt 4	okt 11	okt 18	okt 25	nov 1	nov 8	nov 15	nov 22	nov 29	dec 6	dec 13
P	1	Literature Study	6-2-2017	16-6-2017	95																							
A	1.1	AE4010	6-2-2017	21-4-2017	55																							
B	1.1.1	Literacy Training	6-2-2017	6-3-2017	21																							
B	1.1.2	Gantt chart	6-2-2017	10-2-2017	5																							
A	1.2	Mid term Lit. Study	13-2-2017	21-4-2017	50																							
A	1.3	Final Hand-in	24-4-2017	16-6-2017	40																							
P	2	Phase 1	27-2-2017	30-6-2017	90																							
A	2.1	**Abaqus Modelling**	**24-4-2017**	**30-6-2017**	**50**																							
B	2.1.1	Linear Buckling	24-4-2017	12-5-2017	15																							
B	2.1.2	Non-Linear Buckling	15-5-2017	9-6-2017	20																							
B	2.1.3	Ultimate Load	12-6-2017	30-6-2017	15																							
A	2.2	**Testing**	**27-2-2017**	**9-3-2017**	**9**																							
B	2.2.1	Static Test	27-2-2017	9-3-2017	9																							
B	2.2.2	Static Data Analysis	16-3-2017	24-3-2017	7																							
P	3	Holiday	3-7-2017	23-7-2017	15																							
A	3.1	Ciao	3-7-2017	23-7-2017	15																							
P	4	Phase 2	24-7-2017	22-9-2017	45																							
A	4.1	**Abaqus Modelling**	**24-7-2017**	**15-9-2017**	**40**																							
B	4.1.1	Damage Init.	24-7-2017	11-8-2017	15																							
B	4.1.2	Interface Damage	14-8-2017	1-9-2017	15																							
B	4.1.3	Residual Ult. Load	4-9-2017	15-9-2017	10																							
B	4.1.4	Contingency week	17-9-2017	22-9-2017	5																							
A	4.2	**Testing**	24-7-2017	12-8-2017	15																							
B	4.2.1	Fatigue	24-7-2017	12-8-2017	15																							
B	4.2.2	Fatigue Data Analysis	24-7-2017	12-8-2017	15																							
P	5	Reporting (& Validation)	17-9-2017	8-12-2017	60																							
A	5.1	Phase 1 reporting	25-6-2017	30-6-2017	5																							
A	5.2	Report outline/template	17-9-2017	22-9-2017	5																							
A	5.3	Mid term review	25-9-2017	20-10-2017	20																							
A	5.4	Final Review/Green Light	23-10-2017	17-11-2017	20																							
A	5.5	Hand in	20-11-2017	8-12-2017	15																							

Figure A.2: Gantt chart of the thesis. Period Jul-Dec

B

APPENDIX B - NDT TECHNIQUES

In order to perform a proper experimental validation of the fatigue disbond growth model a series of tests are to be performed. It is imperative that the data acquired from these tests is in fact usable for the proposed validation. Non Destructive Testing (NDT) will be performed throughout the fatigue life of the experiment as it is vital to minimize the impact on the structure and testing conditions when obtaining data for validation. The first question to be posed here is: what phenomenon is being monitored? This leads to the second question: how can this be captured in both an accurate and precise manner? This chapter is a direct answer to research question 4 in chapter 1 and is used to achieve objectives 2 and 4.

The primary measurement of interest is the disbond area. An initial, known, disbond is present in the panel, introduced by a through-width teflon film between the skin and stiffener, as depicted in fig. 2.4. In the panels considered, disbond growth is the phenomenon of the co-cured matrix cracking under compressive cyclic fatigue loading, as the result of the skin buckling away from the stiffener. Two crack fronts are present, one at either end of the Teflon^{TM} tape, and both may propagate towards the clamped ends of the panel. The goal of the NDT regime is to observe the propagation of these two crack fronts. The key issue here is the fact that the crack fronts are located between two solid sections of carbon fibre reinforced epoxy. Furthermore, the crack fronts must be monitored in-situ, meaning that the fronts may be tracked throughout the fatigue tests, preferably without dis-assembly of the test rig during every measurement.

Of secondary interest is the stability behaviour of the panel as it undergoes fatigue loading. What is interesting to monitor is the load at which the skin buckles away from the stiffener and how it changes as the number of cycles increases and as the disbond increases. The buckling behaviour may be used as an indicator of the disbond growth, since an increase in buckling deflection of the skin, and an increase in the half wave length, will indicate that the disbonded area has increased. Finally, monitoring the development of the buckling pattern may also help to understand the shape of the disbond area. For example an asymmetric buckling pattern may be reflected in the shape and position of the crack fronts.

B.1. ULTRASONIC SCANNING

In the wake of the crack fronts, there is no solid, continuous connection between the skin and stiffener. This gap of air changes the acoustic impedance and is used by ultrasonic scanning equipment to determine both the depth and location of an imperfection in a laminated composite. This technique however relies on an intermediate transmission medium, such as gel or water, between the probe and the inspected material. A large advantage is that this equipment is available as a compact and portable device. Furthermore, it is capable of scanning both metal and composite structures and is not limited to flat surfaces. With such portable devices the scans are performed manually meaning that the results may be operator dependent. To mitigate this, a 2-axis cnc frame may be used to reduce test-retest variability. Such a set-up was used successfully by Davila and Bisagni [58] to measure the fatigue disbond growth of an imperfection between a composite omega stiffener and skin. For a typical portable, hand-held c-scan device, a resolution in the order of 1mm is reported [53], meaning a 1mm diameter defect may be observed.

B.2. THERMOGRAPHY

Thermographic inspection captures the surface thermal signature of an object. It is both a non-contact and non-intrusive form of inspection as it relies purely on the infrared radiation emitted from all bodies with a temperature over absolute zero. Structures may be excited, to improve thermographic analysis. In contrast to ultrasonic scanning, it does not require a couplant such as gel or water to perform the inspection. Further advantages include: greater inspection speed, higher resolution and sensitivity, and detectability of imperfections within a structure. These improvements depend highly on the type of thermography used and are mostly reserved for actively excited structures, ie. with an external heat source. The most suitable thermographic method is described below. For future reference: Yang and He [59] performed a comparative study of the various thermographic methods for composite structures.

Optical thermography - Based on observation of thermal evolution in the structure surface. The structure may be excited with a thermal pulse (active), if not it is classified as passive optical thermography. Davila and Bisagni [58] used a passive thermography set-up to measure disbond initiation and progression of an initial imperfection in a bonded composite structure subject to fatigue loading. However, resolution was rather poor comapred to C-scanning and the crack fronts were not accurately observed. Its use in combination with a CNC c-scan device was well thought out. The passive thermography set-up gave continuous in-situ information on the disbond growth and was used to trigger a pause in fatigue testing and subsequent c-scanning. This powerful set-up allows for c-scans to be made at regular intervals of growth, rather than an estimated number of cycles.
Zalameda et al. [9] made a comparative study of passive thermography, flash thermography, x-ray tomography and non-immersion UT scans of a hat stiffened panel with initial disbond under fatigue loading. A fairly good agreement was found between the flash thermography results and both the x-ray tomography and UT scans. However, the UT scans showed a better resolution and better detection of defects at multiple depths. In fig. B.1, a side-by-side comparison of the NDT techniques is shown. The panel disbond was also monitored using passive thermography for a continuous indication of the disbond growth. A correlation was found when comparing UT scans with the passive thermography image, however the thermographic image resolution was poor. A side by side comparison of passive thermographic images vs UT scans is shown in fig. B.2

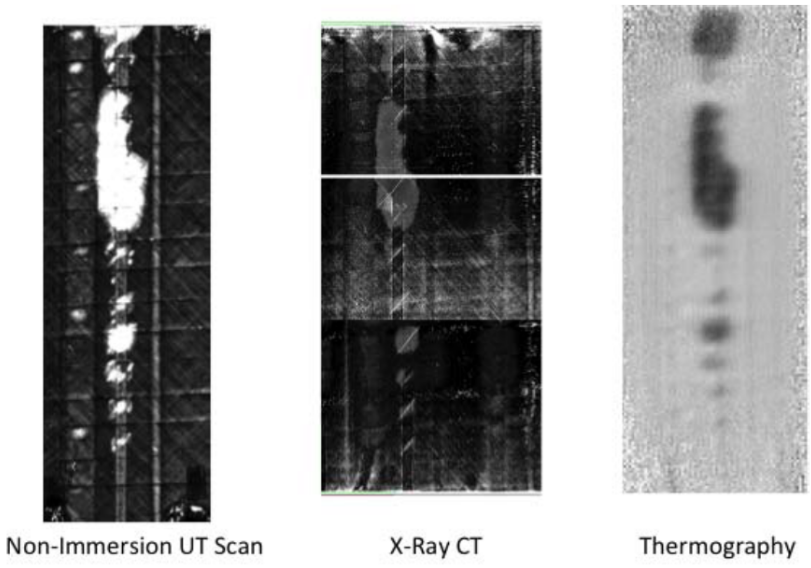

Figure B.1: Left-to-right: Non-immersion UT scan, X-Ray CT, Flash Thermography. Obtained from: [9]

Other thermographic methods such as laser thermography, vibro-thermography, microwave thermogra-

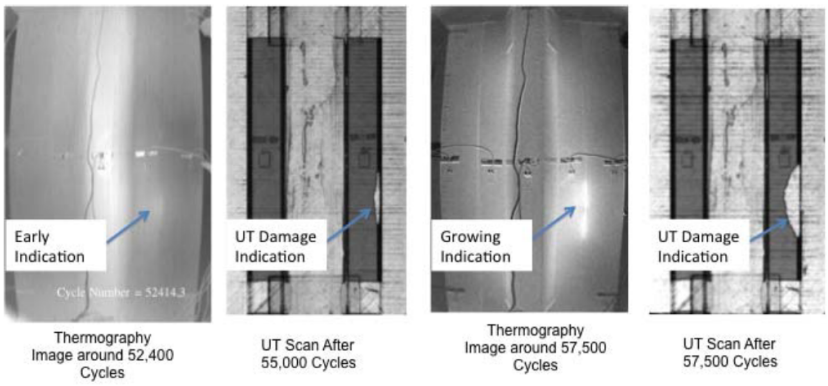

Figure B.2: Comparison of passive thermography with UT-scans, reinforced composite panels with an initial disbond. Obtained from: [9]

phy and eddy current thermography are considered unfeasible due to the expensive and/or complex equipment required for such analyses.

B.3. ACOUSTIC EMISSION

An interesting development in non-destructive monitoring of composite structures lies in acoustic emission. The phenomenon of crack growth releases acoustic waves through the parent structure. If the speed of sound in the material is known, the distance to such an event may be calculated using a sonic transducer. To locate the precise location, multiple transducers may be used to triangulate the event, effectively mapping the crack front as it propagates.

B.4. DIGITAL IMAGE CORRELATION (DIC)

By optically tracking the displacement of a random speckle pattern painted on a surface, the in plane strain of a structure may be captured. With a single camera, only 2D in-plane behaviour is captured, however when using a stereoscopic set-up it is possible to capture out-of-plane behaviour as well. It is a non-intrusive method, requiring only the application of a random, high contrast, speckle pattern to the surface of interest. This relatively low-fidelity inspection technique is able to capture the entire strain field. Relatively fast post-processing is possible, giving near continuous data of the surface strain field. This technique may be used to capture buckling patterns, and thus with increasing buckling length a correlation may be established between buckle length and disbond length in a stiffened panel with initial disbond, as demonstrated by Tandon [10]; an example is shown in fig. B.3. This method however, does not give an accurate depiction of the crack front and may therefore be used as a trigger to perform more accurate c-scans, similar to how passive thermography was used by Davila and Bisagni [58] to pause the fatigue testing and perform a c-scan. An analog to this method would be the use of a Moiré grid on the buckling surface, as demonstrated by Kong et al. [25] and Krueger [4].

B.5. CONCLUSION

Two areas of interest were identified in the introduction of this chapter: the evolution of the two disbond crack fronts and the stability of the skin under compressive fatigue loading. Of the examined NDT methods examined here, ultra-sonic scanning is deemed the most robust inspection technique to accurately and precisely capture the propagation of the crack fronts in-between the laminated composite sections. As noted several times, it is advantageous to utilize a secondary NDT technique such as passive thermography, DIC or a Moiré grid as a 'trigger' for the ultra-sonic scan to be performed. This is due to the fact that the fatigue experiment must be halted in order to perform an ultra-sonic scan. To ensure that scans are performed when disbond growth has occurred, such a global, in-situ technique may be accurate enough the determine that some growth has occurred. This will streamline the fatigue experiments by making sure that time consuming

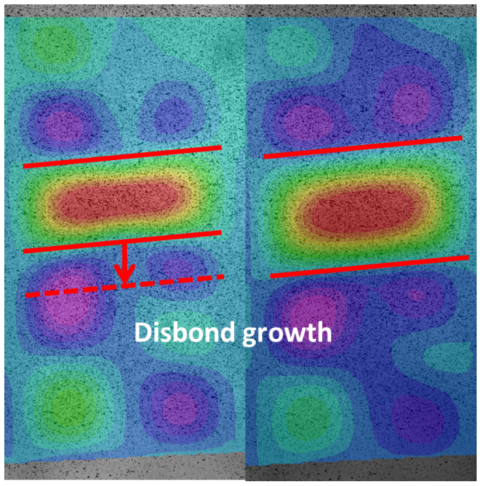

Figure B.3: Disbond growth monitoring in a stiffener reinforced panel with initial disbond. Obtained from: [10]

tests (c-scans) are only performed when needed.